A STUDY OF IRON POWDER COMPACTION FOR AUTOMOBILE COMPONENTS APPLICATION

By

CHENGHAO ZHAO, B.Eng. (Mechanical Engineering)

McMaster University

A Thesis

Submitted to the School of Graduate Studies

In Partial Fulfillment of the Requirements

for the Degree

Master of Applied Science

McMaster University

A STUDY OF IRON POWDER COMPACTION FOR AUTOMOBLIE

COMPONENTS APPLICATION

MASTER OF APPLIED SCIENCE (2009) McMaster University

(Mechanical Engineering) Hamilton, Ontario

TITLE: A Study of Iron Powder Compaction for Automobile Components Application

AUTHOR: Chenghao Zhao, B. Eng. (Mechanical Engineering)

McMaster University

SUPERVISOR: Dr. Mukesh K. Jain

Department of Mechanical Engineering

McMaster University

NUMBER OF PAGES: XIX, 135

Abstract

The major advantage of the Powder Metallurgical (P/M) manufacturing process is its ability to shape powder directly into a final component form with a primary goal of a high quality, homogeneity of density and mechanical properties and productivity. In this research, powder die filling, powder transfer and powder compaction process have been studied in succession using a novel experimental set-up that utilizes a high strength transparent wall section to observe and record the particle movement and powder compaction during the entire sequence leading up to the formation of a green part. The natural powder pattern itself, as observed from the transparent wall section, is utilized for obtaining full-field displacement and strain measurement for the first time. This strain field data is converted into density distribution data and is validated through other commonly used density measurement methods. The test set-up and the strain measurement technique offer a means of quickly obtaining density distribution data in select cases. In addition to the above, several powder flow characteristics during die filling, powder transfer and powder compaction under a range of test conditions have been noted through a series of high-speed photographic recordings. The role of transfer speed and friction in the development of density gradient and crack formation has been experimentally assessed. Another new method of density measurement based on surface roughness of the compact has been investigated. Finally, powder compaction simulations of the lab-based experiments have been carried out using modified Drucker-Prager Cap model within the ABAQUS CAE. The simulation results are in good agreement with experimental data.

Acknowledgements

I would like to first express my sincere appreciation to my supervisor, Dr. Mukesh K. Jain, for offering me a chance to complete this interesting research, and his instructive guidance and support throughout this research.

I would also like to thank Dr. Michael Bruhis for his invaluable assistance in conducting the experiments. His enthusiasm and dedication in perfecting my experiments is much appreciated.

I would also like to thank Dr. Baosheng Zhang for his support and constructive suggestions during the development of the FE simulation model.

I would also like to thank Mr. Doug Culley, Mr. Chris Butcher and Dr. Meneesh Khanna for their help with hardness measurements, image analysis and surface roughness measurement respectively.

I would also like to thank Gates Canada research staff, Mr. Roger Lawcock and Mr. Yannic Praden, for the help of powder mixture preparation and powder compact sintering. I am also grateful to Gates for financially supporting this research.

Finally, I would like to thank my parents for their encouragement, financial support, and patience.

Table of Contents

List of Figures

List of Tables

Nomenclature

c	Cohesion	(Figure 2-13)
$d, \beta, \alpha, P_b, R, P_a$	Material parameters in DPC model	
D	Diameter of cylindrical compact	(Equation 2-1)
E	Young's modulus	
f	Density dependent parameter	(Table 2-1)
G	Bulk modulus	
F_d	Load of diametrical compression test	(Figure 5-5)
F_c	Load of uniaxial compression test	(Figure 5-5)
F_f	Frictional force	(Figure 2-4)
F_n	Normal force	(Figure 2-4)
F_T	Load in transverse direction	(Equation 4-4)
F_z^u	Upper punch load during compaction	(Equation 4-4)
F_z^l	Lower punch load during compaction	(Equation 4-4)
H	Height of compact	(Equation 2-2)
HV	Vickers hardness value	
J_1,	First invariant of stress tensor	(Table 2-1)
J_2'	Second invariant of deviatoric stress tensor	(Table 2-1)
k	Variable represents the material hardening	(Table 2-1)
K	Shear modulus	
L	Length of powder compact	(Table 4-2)
m	Mass	
m_o	Initial mass	
n	Work hardening exponent	
q_A	Mises Equivalent stress at point A	(Equation 5-9)
q_1, q_2, q_3	Material constant in Gurson model	(Table 2-1)
P	Compression pressure	(Equation 2-1)

R	Relative density	(Table 2-1)
R^2	A statistical measurement of fitness	
R_a, R_z	Surface roughness parameters	
t	Thickness of the compact	(Equation 5-5)
V	Volume	
V_o	Initial volume	
x	Distance below top punch	(Equation 2-1)
z	Proportionality constant with density	(Equation 2-1)
ε_V	Volumetric strain	(Equation 3-4)
ε_h, ε_w, ε_b	Strain components	(Equation 3-4)
σ_e	Von Mises effective stress	
σ_T, σ_B	Axial stress applied by top and bottom punches	(Equation 2-2)
σ_1, σ_2, σ_3	Principle stress	(Figure 2-13)
σ_m	Hydrostatics stress	(Figure 2-13)
σ_r	Stress in transverse direction	(Equation 2-2)
σ_z	Axial stress at position z	(Equation 2-2)
ρ	Density	
ρ_o	Initial density	
ρ_t	Density after powder transfer	(Equation 4-2)
δ	Angle of internal friction	
v	Poisson's ratio	
μ	Coefficient of friction	

Chapter 1

Introduction

1.1 Powder Metallurgical (P/M) Parts

Powder metallurgical (P/M) parts through metal powder compaction offer the possibility of near net shape production of complex geometries with substantial reductions in cost at large scale production as compared to traditional manufacturing process such as forging, blanking, machining and metal casting. Some parts requiring porosity such as certain filters and self lubricating bearings can only be produced by P/M process. P/M for manufacturing of small precision components is becoming an increasingly important industrial technique [German, 1994].

The automotive industry is the main user of P/M components, which are commonly used in transmission, engine, suspension, brake and exhaust applications, as shown in Figure 1-1. A modern automobile contains on average 10 kg of P/M components. However, US automobiles tend to have far more P/M components than those produced in Asia. Since Asia is the fastest growth region of automobile production, the future demand for P/M parts in Asia is expected to increase. However, in order to meet the increasing demand in automobile industry, P/M parts have to meet the precision of complex geometry as well as mechanical performance while utilizing its lower cost structure [Berg, 2005].

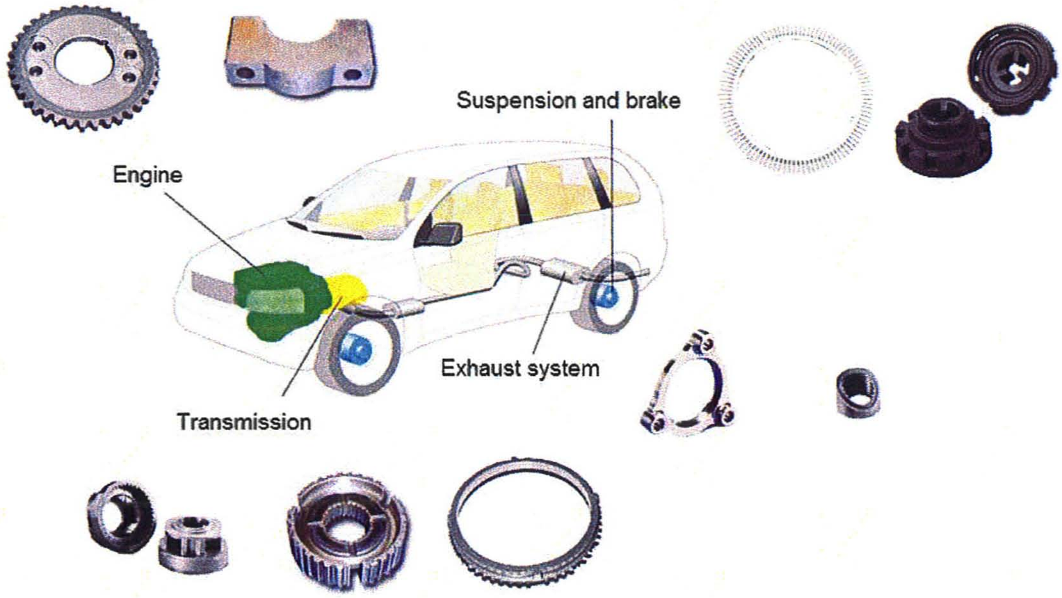

Figure 1-1. P/M parts in automobile applications [www.hoganas.com].

Generally P/M forming process produces parts by cold compaction, sintering, and finishing. An overall sketch of P/M manufacturing process and a general description of the complete P/M processes are shown in Figure 1-2 and Figure 1-3 respectively. Major steps involved in P/M are described below.

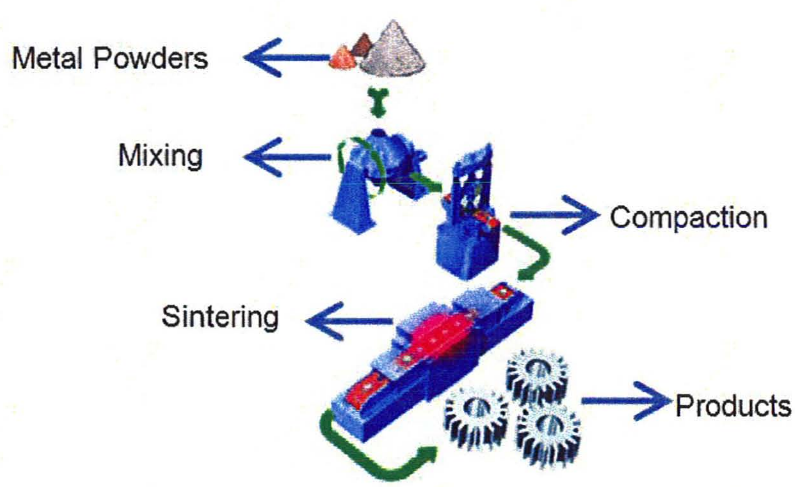

Figure 1–2. An overall sketch of P/M manufacturing process [www.hoganas.com].

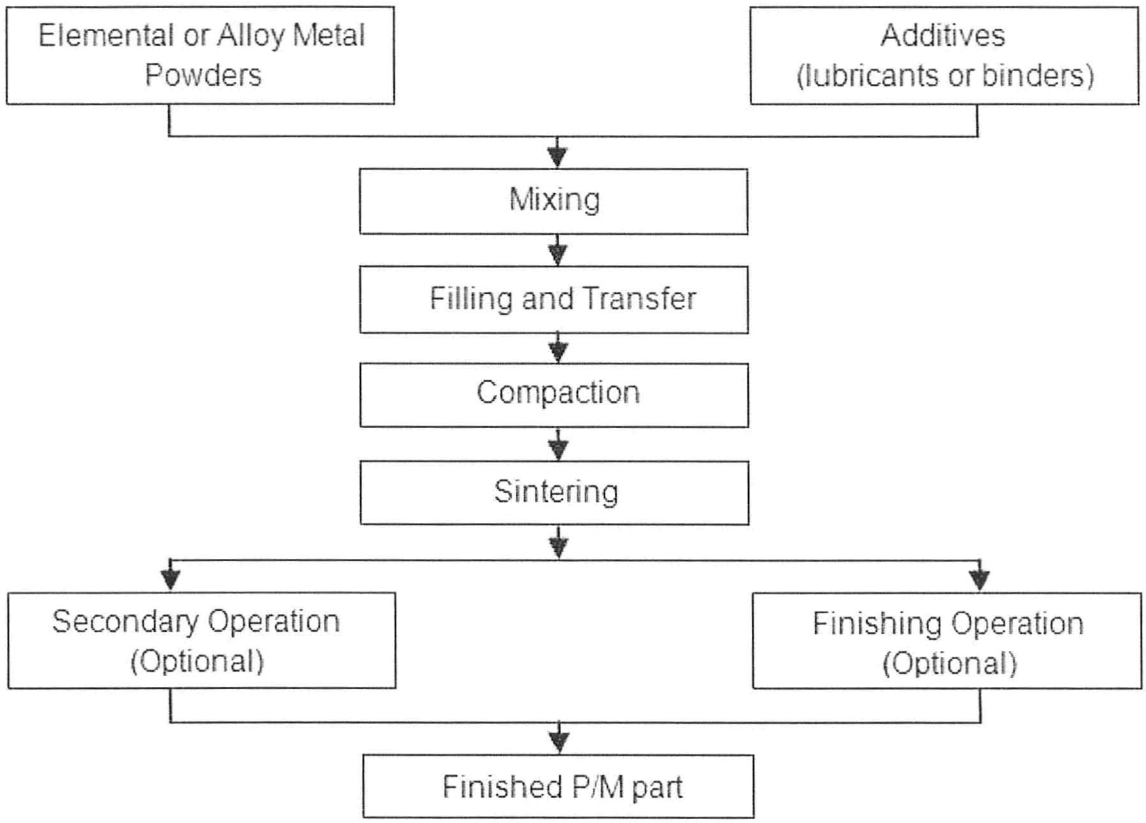

Figure 1-3. P/M parts manufacturing processes [Kim, 2007].

Mixing: Raw powders, having the desired size, shape, and other important characteristics are blended with additives such as lubricants or alloy additions in a device. Usually a double-cone or V shape mixer is used to ensure the production of a homogeneous mix [Kim, 2007].

Filling and Transfer: A feed shoe fills the die cavity with metal powders. The feed shoe moves forward and backward to ensure the even distribution of powders. The powder is then moved to the compaction position. Filling and transfer is directly related to the quality of P/M compacts and the cycle time of the production [Cocks, 2001; Kim, 2007].

Compaction: Metal powder in a die cavity is compacted with upper and lower punches. Upon compaction, each metal powder experiences plastic deformation. Green compact maintains its shape by mechanical bonding, which is very fragile. Mechanical or hydraulic presses with separate movements of multiple punches are typically used [Kim, 2007].

Sintering: Sintering is carried out in a furnace at temperature slightly below the melting point of the metal powder and under the environments of hydrogen or argon gas. During this stage, strong bonding develops between powder particles and internal diffusion happens of any alloying additions. Microstructure images of a compact before sintering and after sintering are shown in Figure 1-4. There are generally no significant changes in size and shape, although changes of internal pore structure and some relaxation of the internal residual stresses do occur during sintering [Cocks, 2001; Kim, 2007]. Sintering imparts significant strength improvement to the green part to enable its usage for in-service components.

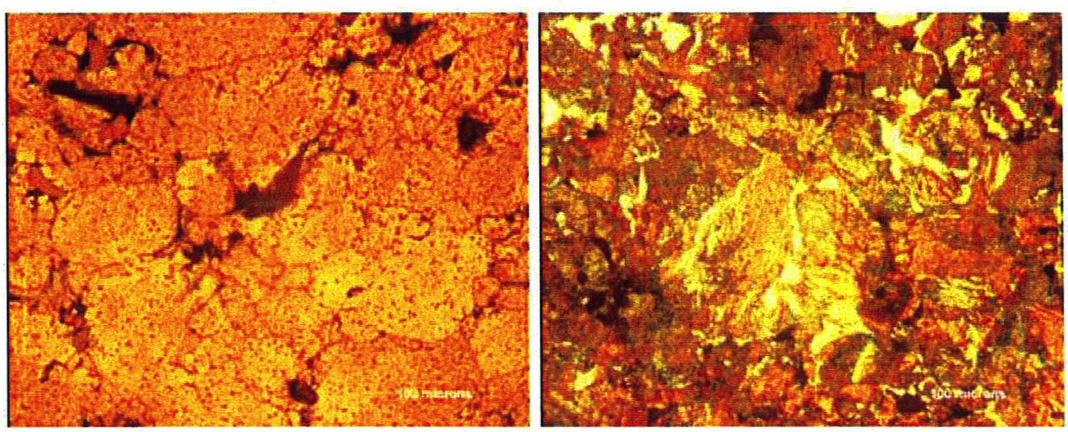

(a) (b)

Figure 1-4. Images of a compact surface (a) before sintering and (b) after sintering.

The main manufacturing route in P/M products is via die compaction. P/M parts formed by die compaction have inhomogeneous density distribution because of improper die filling and the friction between the powder compact and the die wall and punches [Kwon et al., 1997]. For the continued growth of P/M parts two main factors are important, close tolerances and high mechanical strength [Berg, 2005]. The green density and its distribution within a part is a critical factor that has a significant effect on the tolerance and mechanical strength.

Due to the complex powder deformation mechanisms occurring during the compaction process, part and tooling design is a very delicate task. Except for routine parts, for which P/M engineers have developed extensive know-how, this task is traditionally performed through expensive trial and error approach [Chtourou et al., 2002]. Therefore, the finite element (FE) simulation method has recently been used as an alternative design tool in P/M industry. This method, through the use of an appropriate constitutive model of the powder medium, permits the prediction of density and stress distributions in the pressed compact prior to the actual tooling design and manufacturing activity. However, the accuracy of FE prediction highly depends on the choice of an appropriate and well calibrated powder material model, as well as on the effectiveness of the computational environment.

1.2 Objectives of Present Research

This research focuses on a study of factors having impact on the green density of P/M parts in laboratory experiment of P/M cold die compaction. These factors include the apparent density after filling and transfer, compaction load, compaction mechanism and powder types which will all have influence on the green density and its distribution in a P/M part. Specifically, the main objectives of this research are:

1. Development of a well instrumented, powder filling, transfer and compaction system with the existing MTS double action press for continuous observation of powder flow and rearrangement during various stages.

2. A comprehensive experimental study of die fill, powder transfer and powder compaction processes in a sequential manner using the above system. Emphasis is placed on analyzing the nature of punch speed and load during these processes.

3. Investigation of 2D green compaction density and its distribution within the part by various new techniques such as Digital Image Correlation (DIC) by utilizing the ARAMIS on-line optical imaging system, Vickers hardness measurements and surface roughness measurements as a function of process parameters.

4. FE Simulation of lab-based compaction experiments using a well accepted modified Drucker-Prager Cap material model to further understand the experimental results.

Chapter 2

Literature Review

2.1 Metal Powders for P/M Parts Manufacturing

Metal powders have been used as engineering materials to manufacture parts by powder metallurgical (P/M) techniques for more than 50 years [Cocks, 2001]. For different P/M applications, metal powders have developed into wide range products with different chemical compositions, particle sizes and particle shapes. There are four main methods for powder production: solid-state reduction, atomization, electrolysis, and chemical, as shown as in Figure 2-1, resulting in variations in particle shape, size and size distribution that profoundly affect the way the powder behaves during die filling, compaction and sintering. The range of shapes can be irregular, spherical, flake, angular and sponge [German, 1994]. For production of automotive structural parts, water atomised iron powder is typically used. This powder has an irregular shape and is free of internal porosity [Smith, 1996]. In addition to the chemical and physical properties derived from the materials, there are a number of other properties that are important to metal powders. They include particle size distribution, flow rate, bulk density, compressibility, green strength and spring-back characteristics of the metal powder. Lubricant is generally added into the powder mixture, which plays a critical role in reducing forces, both interparticle and die wall, during powder compaction and ejection processes [German, 1994].

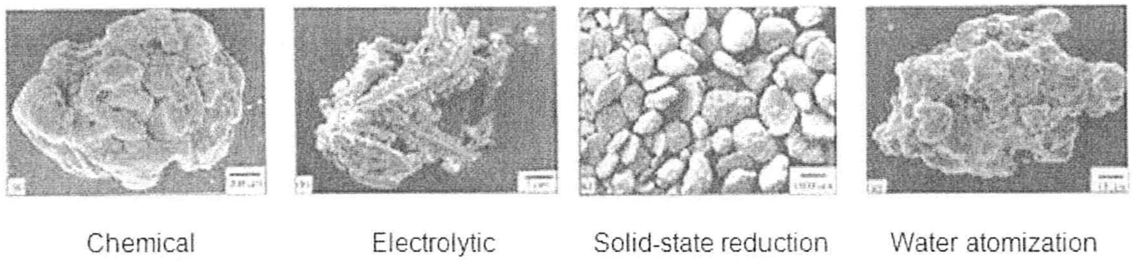

Figure 2-1. Metal powders: Chemical: Sponge iron-reduced ore; Electrolytic: copper; Solid-state reduction: milled aluminum; Water atomization: iron [www.mpif.org].

Particle size distribution plays an important role in particle packing to determine the apparent and tap density, with a larger particle size distribution usually yielding a larger tap density. To overcome the inherent packing limits of powder, it is possible to tailor the particle size distribution for a higher packing density [German, 1994].

2.2 Powder Filling and Transfer during P/M Process

Powder filling, the first step in P/M process, has an important influence on subsequent P/M processes, and final part density distribution, and part in-service performance. This critical step has not been well understood. The main factor that influences the mechanical properties of powder components is the fill density in die cavity. This leads to the density differences between front and rear of the components, which results in internal cracks in the components and tool breakage. Since it is the first step in the process of P/M, on which the rest of the steps depend on, an improper powder filling with a feed shoe ends up with a poor quality part no matter how perfect the rest of the processes are [Wu et al., 2004].

There are two major die filling techniques, gravity filling and suction filling [Jackson et al., 2007]. For gravity filling, Demery et al. evaluated the quality of the powder fill in the die cavity using tactile sensors [Demery, 1998]. Wu and

Cocks et al. have been investigating powder flow using an experimental set-up with a transparent die and high speed video, as shown in Figure 2-2. Main studies of the die filling process were related to gravity/drop fill and based on the lactose powder and fine sand material. The studies carried out by Cocks and co-workers are useful in obtaining an understanding of the powder distribution during die filling. However, using this set-up they could not investigate in a sequential manner of all stages of the PM process; powder fill, transfer, compaction and ejection of the green compact [Wu et al., 2003 and 2004].

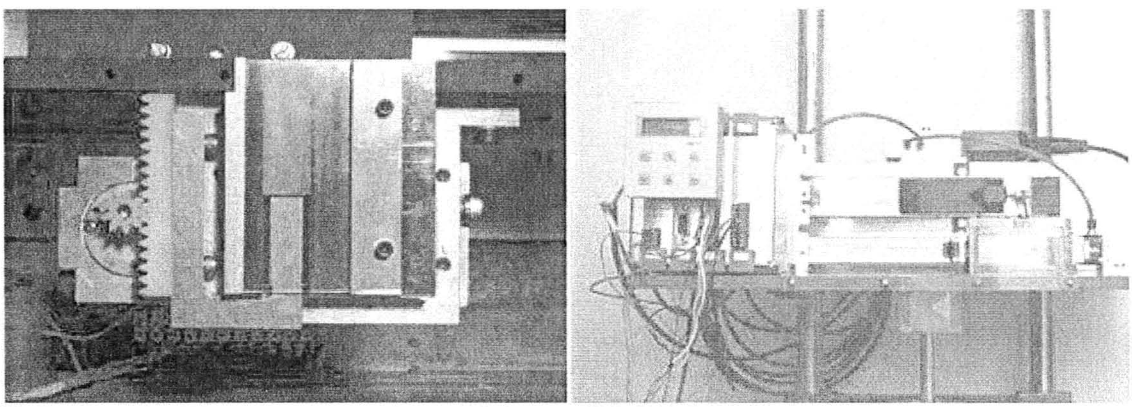

(a) (b)

Figure 2-2. Experimental set up with (a) a transparent die, (b) automatic feed system [Cocks et al., 2009].

In these studies, Wu et al. also introduced the concept of a critical velocity, the maximum shoe velocity at which a standard die is filled, as a measure of flowability. Figure 2-3 shows a typical fill ratio-shoe velocity graph obtained using gravity filling. The amount of powder delivered into the die or fill ratio (mass of powder in the die divided by mass of powder when the die is full) is plotted as a function of shoe velocity [Wu et al., 2004].

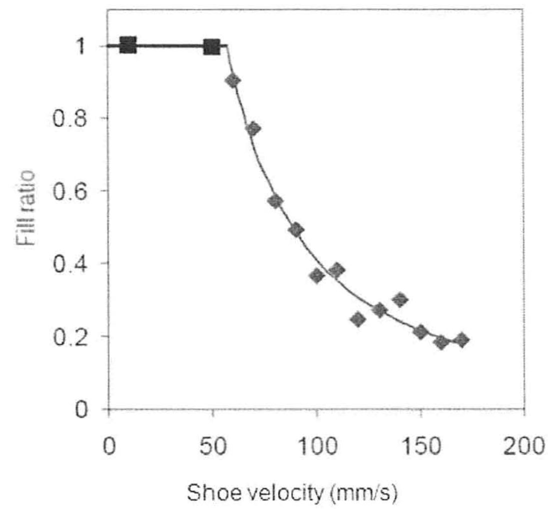

Figure 2-3. Fill ratio versus shoe velocity [Wu et al. 2004].

Suction filling, on the other hand, has received far less attention than gravity filling and as a result, the compaction behaviour of the iron powder material, utilized for nearly all automobile P/M parts, by suction has not been fully analyzed. Recently, Cocks et al. have found for pharmaceutical powders that suction fill can improve die fill uniformity that is often a limiting factor for setting the operating speed. For gravity fill, the incoming powder interacts with the air present in the die which permeates through the powder bed in the shoe. The air pressure build up reduces the net flow rate of powder into the die and creates turbulence which can cause segregation. Suction fill creates a partial vacuum under the powder in the shoe as the lower punch is withdrawn at the same time as the powder is fed into the die. Thus, air is not trapped to oppose the flow of the powder into the die, which also reduces the opportunity for segregation [Cocks et al., 2009].

The density distribution of powder particles in the die cavity before compaction is critical to the compaction characteristics and density distribution after pressing. However, despite the importance of solids transport phenomena, there have been few experimental studies of powder transfer in the die in the context of P/M processes. The particles motion during powder transfer using a screw-driven motor and a pneumatic cylinder has been analyzed using a laboratory built apparatus and a numerical model [Wu et al., 2003]. Wu et al. also mentioned the influence of powder characteristics such as particle size on the powder transfer process in the hopper [Wu et al., 2003]. Sielamowicz et al. had observed a non-uniform granular flow using the digital particle image optical technique and they found that this effect of the flow is associated with shear deformation and discontinuities in the velocity fields [Sielamowicz et al., 2006]. Also, for granular material, during transfer, powders are sheared along the shear bands which influence the packing density. This shear deformation under certain compaction conditions can develop into cracks [Zhang, 2003]. However, these studies have not been carried out on iron powders in a closed die system.

2.3 Compaction Behaviour of Metal Powders

2.3.1 Fundamentals of compaction

The compaction process can be divided into 3 stages. In the first stage, the packing of powders is generally loose and compaction results in rearrangement of the powders. In the second stage, as the relative density increases, further compaction is accommodated by plastic deformation of powders. In the third stage, with higher relative density, the networks of interconnected channels pinch off to form a distribution of isolated pores [Cocks, 2001].

Steinberg et al. were the first to investigate the distribution of density in powder compact as a function of pressure, height and diameter of the compact [Steinberg, 1947]. Mathematical expressions for pressure distribution have been obtained by many researchers. German presented a general expression for a cylindrical compact of diameter *D* and height *H* during a single action compaction, as shown in Figure 2-4 [German, 1994]. Analyzing a thin section of height *dH* when there is an external pressing force *P* on top of the element and that transmitted through the element P_b will differ by the normal force acting against friction. Mathematically, on this thin section, the balance of forces along the axis can be expressed as follows:

$$P_x = P \exp\left(-4 \mu z x / D\right) \tag{2-1}$$

where μ is the coefficient of friction between the powder and the die wall, and x is the distance below the punch. A proportionality constant z varies with the compact density [Shima and Oyane, 1976; German, 1994]. The equation shows that pressure decreases with depth in the powder bed, as plotted in Figure 2-5.

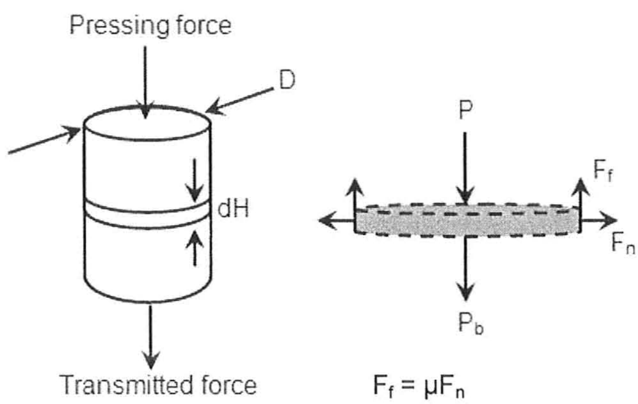

Figure 2-4. The balance of force during die compaction for a thin section [German, 1994].

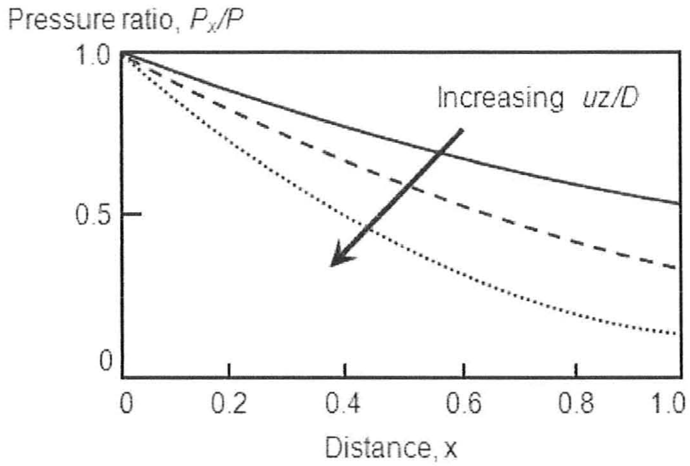

Figure 2-5. The pressure gradient below the top punch in single action die pressing as given by equation 2-1 [German, 1994].

For double action compaction, there is a simultaneous pressure distribution from both the top and bottom punches. This results in a more homogenous pressure distribution in the compact. The above equation is also valid for double action compaction, but the distance *x* is now the distance to the nearest punch [German, 1994].

2.3.2 Effect of die wall friction during compaction

Friction during the powder compaction process is important in powder compaction because it can lead to spacial variation in density, occurrence of defects. Friction also influences the pressing and ejection forces and induces wear. Friction may depend on several factors: contact pressure, local powder sliding velocity and distance, temperature and die wall roughness. In addition, friction is not only dependent on the amount of lubricant present in the powder system but also on whether this lubricant is admixed with the powder or deposited on the die wall [Meerson et al., 1970; German, 1994; Sinka et al., 2003].

In order to determine the friction force during compaction of pharmaceutical powder, Sinka et al. used the following equation to calculate the friction coefficient during a single action compaction in a closed cylindrical die (see Figure 2-6):

$$\mu = \frac{D}{4H} \frac{\sigma_B}{\sigma_r(z)} \left(\frac{\sigma_T}{\sigma_B}\right)^{\frac{z}{H}} ln \frac{\sigma_T}{\sigma_B} \tag{2-2}$$

where *D* is the die interior diameter, H is the compaction height in the die, $\sigma_r(z)$ is the pressure in the transverse direction at the position z from the top surface of the powder compact, and σ_T and σ_B are axial compression stresses applied by the top and bottom punches respectively [Sinka et al., 2003].

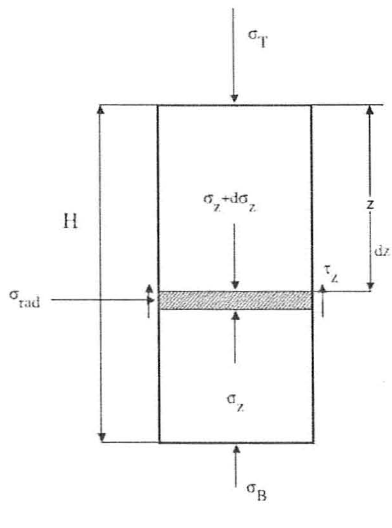

Figure 2-6. Analysis of instrumented die data and extraction of the coefficient of friction [Sinka et al., 2003].

2.3.3 Particle bonding in the green state

Cocks pointed out that the inter-particle bonds formed due to compaction provide the green strength. The solid interfaces are created by deformation at the point contacts between particles [Cocks, 2001]. German also mentioned that at a high initial packing density and a clean (smooth) powder surface aid the formation of inter-particle bonds. When the compaction force is sufficiently high, shear forces will act to disrupt surface films. However, German also pointed out that there is no evidence of cold welding of the particles. The attractive forces acting between particles are weak compared with forces after sintering where substantial strength increase is observed [German, 1994]. The properties of a typical iron powder compact before sintering and after sintering are shown in Figure 2-7.

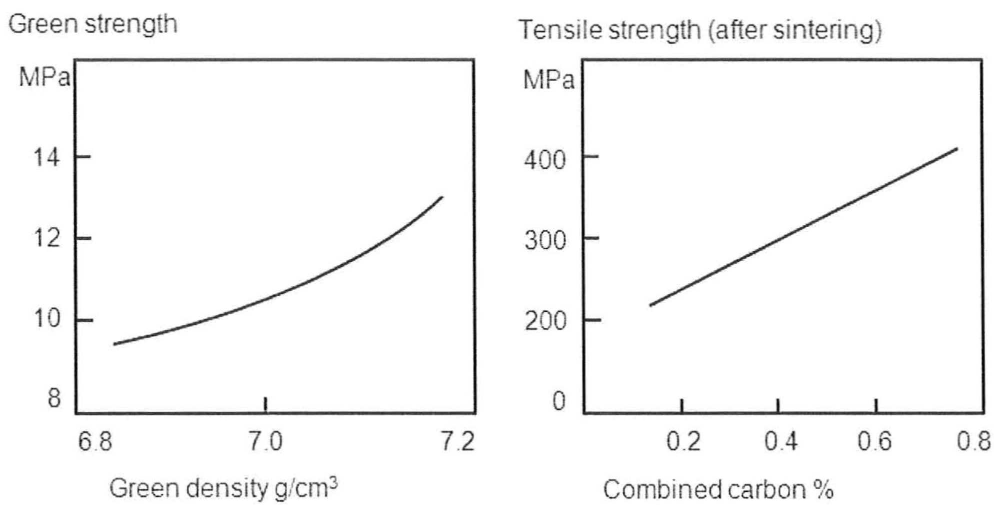

Figure 2-7. The green strength of an iron powder compact and the tensile strength of a 6.8 g/cm^3 compact after sintering at 1120°C for 30 min [QMP, 2006].

2.3.4 Goals in compaction

The predominant goal in powder compaction is to achieve uniform high compact properties or density. Effort is often directed toward reducing the wall friction during compaction or designing the parts with lower height to diameter ratio. Die wall friction dominates at low lubricant contents, thus adding sufficient lubricant can help. When the height to diameter ratio exceeds five, die compaction is often unsuccessful [German, 1994]. By adopting double action compaction also can improve the uniformity of powder compact than single action compaction as shown in Figure 2-8.

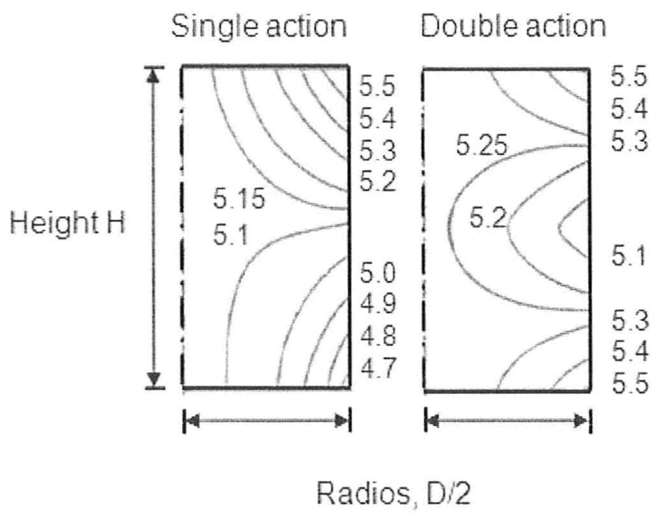

Figure 2-8. Constant density line in cylindrical compacted copper powder for single and double compactions [German, 1994]. Note that measurements of density are shown for the symmetric half of the two parts.

Conventional P/M processing of metal powder to achieving near full density requires long time sintering at high temperatures. In recent times, the use of smaller size powder has been an established technique to improve the quality of metal powder compacted parts [Tanwongwan et al., 2005]. However, German and Olevsky have suggested the use of high compaction load can help in reducing the sintering time and temperature, as shown in Figure 2-9. The smaller the particle size, higher is the required compaction load [German and Olevsky, 2005].

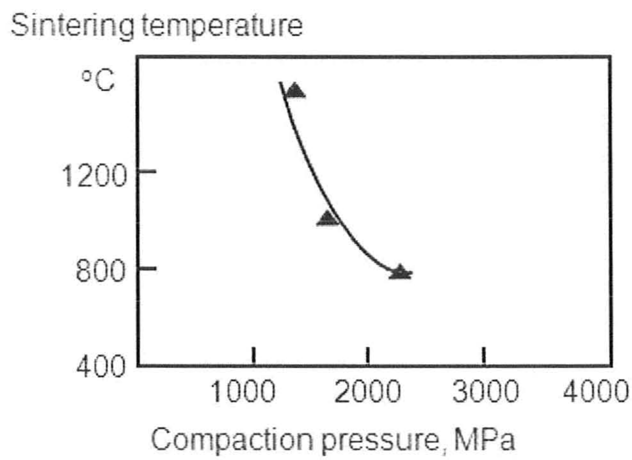

Figure 2-9. Sintering temperatures required for 20 nm tungsten powder compact at different compaction pressure [German and Olevsky, 2005].

2.3.5 Powder compaction systems

The uniaxial closed die compaction has been used to produce the majority of P/M components in industry for over 50 years. Experimentalists have also adopted such a set up to study powder compaction. In 1970's, Green [Green, 1972], Kuhn and Downey [Kuhn and Downey, 1971], Shima and Oyane [Shima and Oyane, 1976] used closed-die compaction to help study the basic porous metal theory. More recently, Fleck [Fleck, 1995], Kim and Kim [Kim, 1996], Kwon et al. [Kwon et al., 1997] and Han et al. [Han et al., 2007] used the closed-die system for single action or double action compaction tests to study the compaction behavior of various powders and build sophisticated computer simulation models. However, the uniaxial die pressing is shown to exhibit two significant limitations. The first is that the length-to-diameter ratio of the compact is very limited; the second is that the density of die pressing is not uniform.

The limitations discussed above indicate why other P/M process such as hydrostatic pressing is also utilized. Equipment for carry out hydrostatic pressing consists of a pressure vessel with an assembled elastomeric tooling inside, a pumping system to develop the required pressure and a control system [Gripshover, 1970]. Since the uniform density can be achieved throughout the pressing, hydrostatic pressing is particularly well suited for large components. However, hydrostatic pressing is not without its limitations. The production rates of components made by hydrostatic pressings are generally much lower than those for conventional die pressing.

Hydrostatic pressing systems equipped with displacement transducer and pressure measuring and recording system are often adopted by scientists to investgate the nature of compaction and to obtain the mechanical properties such as elastic modulus, yield strength, and flow stress of compacted powder. In early 1970's, Meerson et al. used a composite die whose walls were assembled from separate rings to measure the pressure and strain in transverse direction for compacting tungsten carbide-cobalt mixture [Mearson et al. 1970]. More recently, Lee and Kim adopted a hydrostatic compression test apparatus to investigate the mechanical properties of aluminum alloy powder compact, as shown in Figure 2-10 [Lee and Kim, 2002].

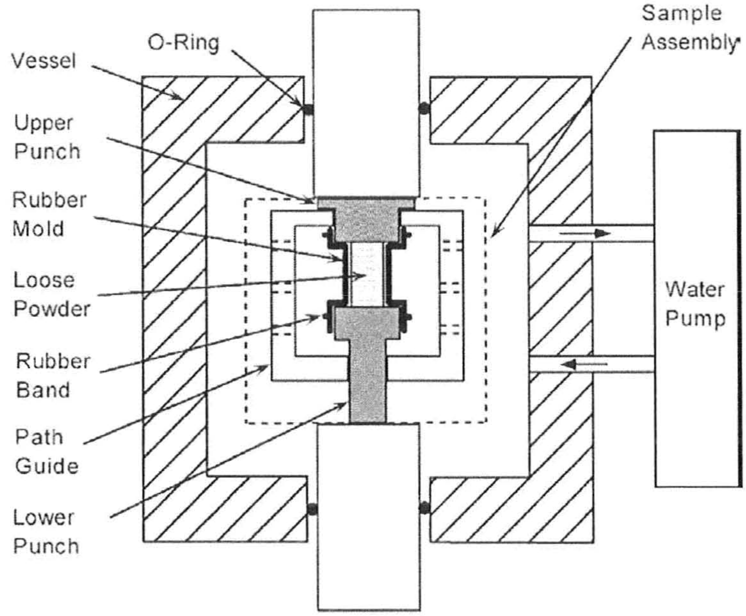

Figure 2-10. A schematic drawing of hydrostatic compression test apparatus [Lee and Kim, 2002].

However, these are no direct visual monitoring techniques reported in the literature for either the uniaxial closed die or hydrostatic compaction systems to provide visual evidence about the powder movements or particle bonding that occur during powder compaction.

2.3.6 Green density and apparent density measurements

Different techniques for green density evaluation have been developed. Unfortunately, most of these techniques are still under development for local density measurement for reason of considerable measurement variability that is caused by inadequate control of sample preparation and testing.

In the early 1950's Kuczynski and Zaplatynsky published a technical note describing a new method to determine the density distribution in green powder compacts by using a hardness measurement. The relationship between hardness and density was obtained by measuring hardness value and densities of thin compacts, assuming that the density for these compacts was constant throughout [Kiczynski and Zaplatynsky, 1956]. The hardness and green density relation has been widely used by the industry and scientist. More recently, Kwon et al. investigated the variation of relative density of 316L stainless steel powder compacts with Rockwell hardness, as shown in Figure 2-11 [Kwon et al. 1997]. In 2002, Chtourou et al. obtained a linear relationship between the green density of 316L stainless steel powder compacts and the logarithm of Vickers hardness. This relationship was then utilized to obtain the local density distribution in compact by making spatial Vickers hardness measurements [Chtourou et al, 2002].

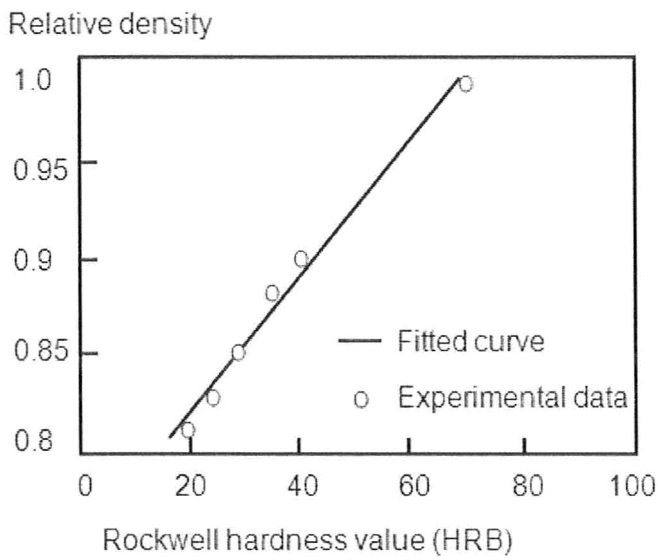

Figure 2-11. Variation of relative density with Rockwell hardness for stainless steel powder compacts [Kwon et al., 1997].

In 1970's, Shulishava and Shcherbak described a new method for the quantitative study of density distribution in compaction process by filling the pores of a part with a fluorescent substance and then placing the part under an ultraviolet light source. The distribution of the intensity of the resultant luminescence corresponded to the distribution of porosity (i.e., inverse of density) in the part [Shulishava and Shcherbak, 1973].

A tactile sensing technique was demonstrated as a feasible tool to evaluate the apparent density after filling. However the reliability of these techniques still needs to be improved for industrial use [Demetry, 1998]. Image analysis based on the light intensity acquired in an image of the object has also shown to be suitable to measure the apparent density after die filling [Obregon, 2007].

A few other methods for predicting the green density and its distribution have been reported by using DC voltage measurement and γ-ray [Ludwig et al. 2005].

2.4 Modeling of Metal Powder Compaction

2.4.1 Review of the different modeling methods for metal powder compaction

The computer-based process simulation of powder metal compaction has been performed by two different approaches: the discrete element model and the continuum finite element (FE) model [Cocks, 2001; Chtourou et al., 2002; Han et al., 2008]. The discrete model method (DEM) [Fleck, 1995; Fleck et al., 1992] simulates individual particles and analyses the contact interaction and deformation of these particles, while the continuum FE models consider the powder as a continuous media.

In the DEM model, each powder particle is typically modeled as a sphere that interacts with surrounding spheres providing insight into the powder flow and rearrangement during die filling and powder transfer as well as aspects of deformation such as during compaction. However, a large number of particles need to be incorporated into these types of models adding to considerable computational cost. So the DEM models are more useful for understanding the fundamental physical processes of powder flow and rearrangement (see Figure 2-12). The limitation of this approach is that it is not suitable for modelling engineering components that require a large number of powder particles than is currently possible with the available computing technology. In addition, majority of the previous works have been investigated using a mono-size spherical (or circular in 2D) powder particle with an initial uniform arrangement [Fleck et al., 1992; Gethin et al., 2001]. Only a few studies have considered modelling powder with several sizes and different initial size distributions [Liu et al., 2000; Tanwongwan et al. 2005].

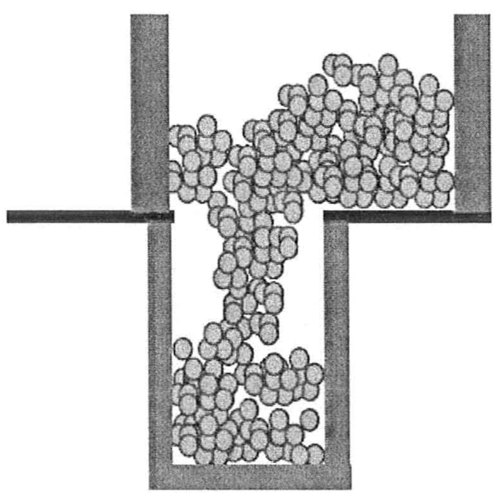

Figure 2-12. A DEM model of P/M compaction die filling process [German, 2006].

The continuum based FE models, on the other hand, consider the compacted powders as a continuous porous media represented by a constitutive model for a porous material with a yield criterion. Thus, the continuum FE models are more suitable for engineering applications [Cocks, 2001; Chtourou et al., 2002]. Some of the commonly used yield criteria include the Drucker-Prager Cap [Drucker and Prager, 1952] (see Figure 2-13 (a)) and the Cam-Clay models [Schofield, 1776] which were originally developed for geological materials. In recent years, several modified models for powder compaction simulation have been developed. In these simulation studies the stress and density distribution during compaction can be quantitatively reproduced [Chtourou et al., 2002; Wu et al., 2005; Sinka et al. 2003]. The other kind of continuum model is based on the classic elastoplasticity models, such as "Kuhn-Shima" model [Kuhn and Downey, 1973; Shima and Oyane, 1976] (see Figure 2-13 (b)) and Gurson model [Gurson, 1977] These models have been adopted to carry out powder compaction simulation based on the assumption that only powder particles undergo plastic deformation and that particle rearrangement is negligible. The models utilize associative flow rule and isotropic hardening [Kwon et al., 1997; Chtourou et al., 2002].

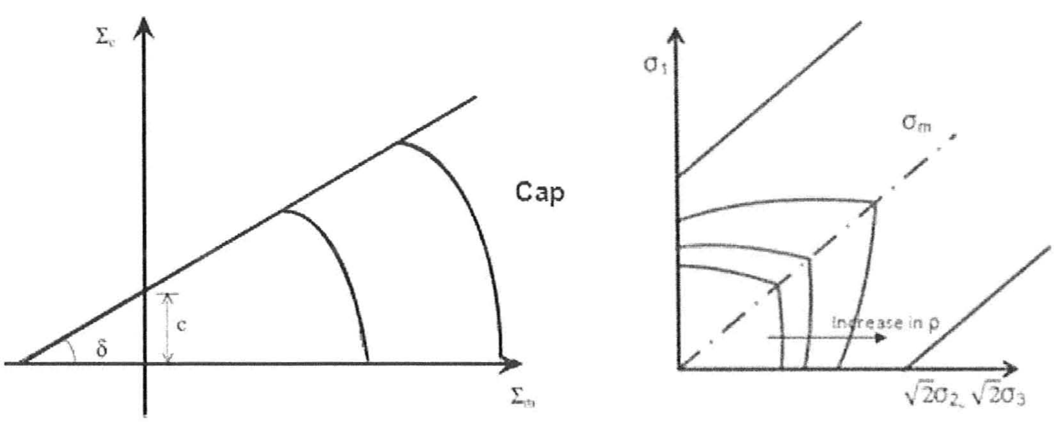

(a) Drucker-Prager Cap (b) Shima and Oyane yield surface

Figure 2-13. (a) The Drucker-Prager Cap model [Drucker and Prager, 1952]; (b) Yield surface of Kuhn-Shima type of model [Shima and Oyane, 1976].

2.4.2 Review of development of various plastic material models for FE simulation of metal powder compaction

Component modeling approach is useful for the optimization of part and die design to achieve manufacturing efficiency. The quality of component modeling result depends strongly on the choice of material model and the determination of calibration parameters for the models. Typically, a general plasticity theory for porous materials is utilized, which differs from the traditional yield function such as Mises function as it incorporates the change in volume of the porous body during compaction. Originally, Kuhn et al. and Green have independently proposed yield criteria and stress-strain relations for porous metals [Kuhn and Downey, 1973]. Under the assumption of isotropic material, in both cases, the yield function proposed for porous materials should include J_1 and the second invariant of the deviatoric stress tensor J'_2. Moreover, it has to fulfil the following condition: as a relative density of porous body ρ increases, the yield surface of P/M material must approach the Mises cylinder, taking this shape at ρ of 1 [Kuhn and Downey, 1973].

Shima and Oyane were concerned with the development of basic equations of plasticity theory for porous materials which are similar to those described above. They made some improvements to determine the material parameters and introduced some examples of the application of this theory [Shima and Oyane, 1976]. For metal powder compaction, the Kuhn-Shima type of model assumes the material response can be described in terms of a single state variable, the relative density [Cocks, 2001]. Due to shape of the Kuhn-Shima yield surface and despite the fact that they correctly model the last stages of compaction, these models are not appropriate for modeling the early stages of compaction where the density level is very low. Subsequently, Kim and Lee have proposed significant changes to the Kuhn-Shima type of model by adding a friction factor to better represent the shear behaviour of the loose powder and to account for internal friction [Kim and Lee, 1992]. Another well-known plasticity theory for porous materials has been proposed by Gurson [Gurson, 1977]. This theory is reliable for relative densities larger than 0.9 for metals and its extension by Tvergaard and Needleman is also well accepted [Biswas, 2005]. Kwon et al. compared the Kuhn-Shima and Fleck-Gurson material models in a FE based simulation of compaction process with experimental data. These results are shown in Figure 2-14.

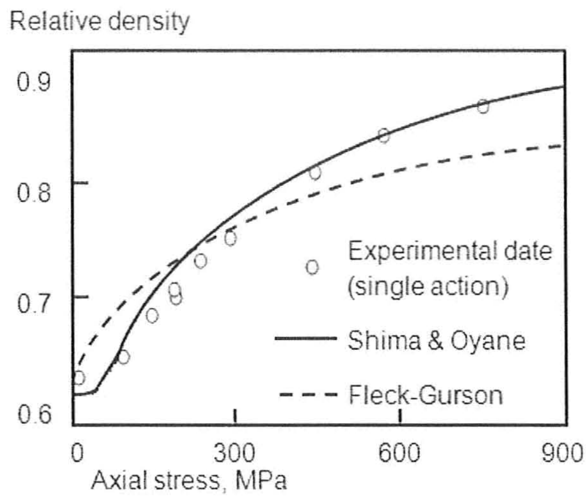

Figure 2-14. Comparison between experimental data and calculated results for incremental relative densities with axial stress of stainless steel powder during compaction [Kwon, 1997].

Some progress has been also made in the construction of plasticity theories for soils, by Scholfield and Drucker. These theories aim to account for some important characteristics of soil material behaviour, such as the dependence of the failure envelope on the hydrostatic stress state, the ability to either soften or harden according to some measure of density, and the ability of dilation or compaction when deviatorically stressed at different densities [Drucker and Prager, 1952; Schofield, 1776]. These soil plasticity theories generally involve macroscopic scale assumptions concerning the means by which the plastic work is dissipated.

Due to the similarities in behavioural response of soil materials and powders the Cap model has been extensively adopted and used to simulate the cold die compaction of powders [Chtourou et al., 2002; Wu et al., 2005; Sinka et al. 2003]. Most common among them, the Drucker-Prager Cap plasticity model, is widely used for powder compaction analysis. More recently, a modified density dependent Drucker-Prager Cap plasticity model has been used to simulate the compaction behaviour of a pharmaceutical powder, as shown in Figure 2-15. Modified DPC has ability to represent the densification and hardening of the powder, as well as the interparticle friction [Sinka et al. 2003, Wu et al., 2005; Han et al, 2008]. This model is available in ABAQUS FEA software, which has been used by researchers to simulate powder compaction. However, the local deformations in powder compact during compaction were not represented in term of strain in these simulation results.

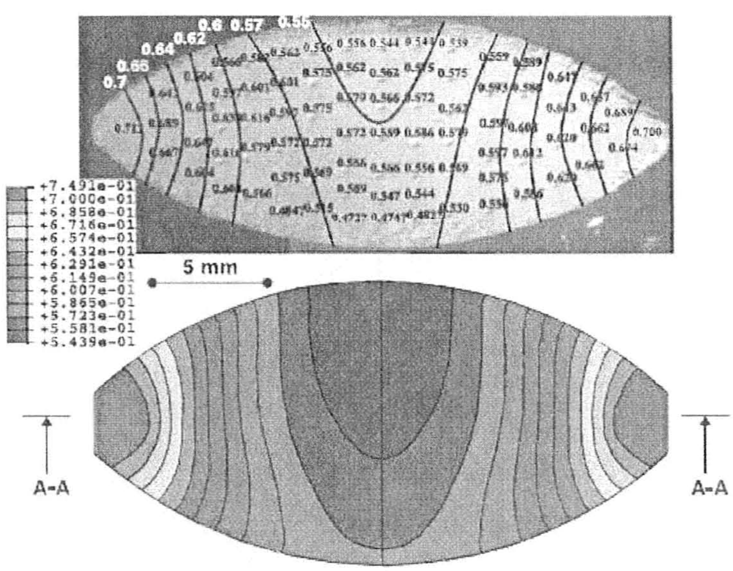

Figure 2-15. The experimental and FE simulation resulting density maps for unlubricated die compaction of pharmaceutical tablet [Sinka et al. 2003].

In summary, starting from the basic plastic theory, researchers have added useful additional material parameters to the governing equations that reflect more accurately the material characteristics during compaction. These material parameters should be determined and calibrated from experiments for specific applications [Cocks, 2001]. Table 2-1 below gives a summary of the various plastic material models and associated material parameters for use in modeling powder compaction processes [Kim, 1992; Biswas, 2005].

Table 2-1. Various plasticity models and their parameters.

Theory	Equation and Parameters
Von Mises (1913)	$J_2^{1/2} = \sigma_m/\sqrt{3}$
Drucker-Prager (1952)	$J_2' = [\alpha J_1 + k]^2$
Kuhn-Downey (1971)	$\sigma_{eq} = [3J_2' - (1-2v)J_2]^{1/2}$
Green (1972)	$\sigma_{eq} = [(3J_2' + \alpha J_1^2)/\delta]^{1/2}$
Shima-Oyane (1975)	$\sigma_{eq} = \frac{1}{\rho^n}[\{(\sigma_1-\sigma_2)^2 + (\sigma_2-\sigma_3)^2 + (\sigma_3-\sigma_1)^2 + (\sigma_m/f)^2\}]^{1/2}$
Gurson (1977)	$\frac{3J_2'}{\sigma_{eq}^2} + 2ncosh\left(\frac{J_1}{2\sigma_{eq}}\right) - (1+n^2) = 0$
Tvergaard (1981)	$\frac{3J_2'}{\sigma_{eq}^2} + 2nq_1cosh\left(\frac{q_2J_1}{2\sigma_{eq}}\right) - (1+(nq_1)^2) = 0$
Lee-Kim (1992)	$[(2+R^2)J_2' + \left(\frac{1-R^2}{3}\right)J_1]^{1/2} = (\frac{R-Rc}{1-Rc})^2\sigma_{eq}$

Chapter 3

Experimental Methodologies

This chapter presents the development of a metal powder compaction test system and various types of compaction tests that are carried out on iron powder mixtures. In addition, several local density measurement techniques utilized in the present work are described.

3.1 Metal Powder Compaction Test System

3.1.1 Properties of metal powders used in this research

Two different powder mixtures are primarily used in this research. First, without Kenolube lubricant is the ATOMET 1001 powder, manufactured by QMP. Second, with Kenolube lubricant is the SL5506 powder mixture consisting primarily of ATOMET 1001 iron powder. Kenolube is an industrial lubricant manufactured by Hoganas AB, commonly used in the production of P/M components. As supplied chemical properties, particle size analysis and flowability are given below in Table 3-1.

Table 3-1. Chemical composition and other properties of powders used in the experiments.

ATOMET 1001 powder	
Chemical component	wt%
Fe	99.4
O	0.08
S	0.007
C	0.003
Mn	0.2
Apparent Density (g/cm^3)	2.95
Flowability (s/50g)	26
Particle Size (micron)	wt%
+250	10
-250/+150	65
-150/+45	25

SL5506 Powder Mixture	
Chemical component	wt%
ATOMET 1001 powder	97.05
Kenolube	0.7
C	0.65
Mn	0.6
Cr	0.55
Ni	0.45
Apparent Density (g/cm^3)	2.98 -3.18
Flowability (s/50g)	40

ATOMET 1001 powder is a water-atomized steel powder with irregular shape, which is a base powder not directly used for producing P/M parts. SL5506 is a blended powder mixture of ATMOET 1001 powder with added alloys and Kenolube, which is used to produce P/M parts. SEM Images, presented in Figure 3-1, provide morphological characteristics of these two powders.

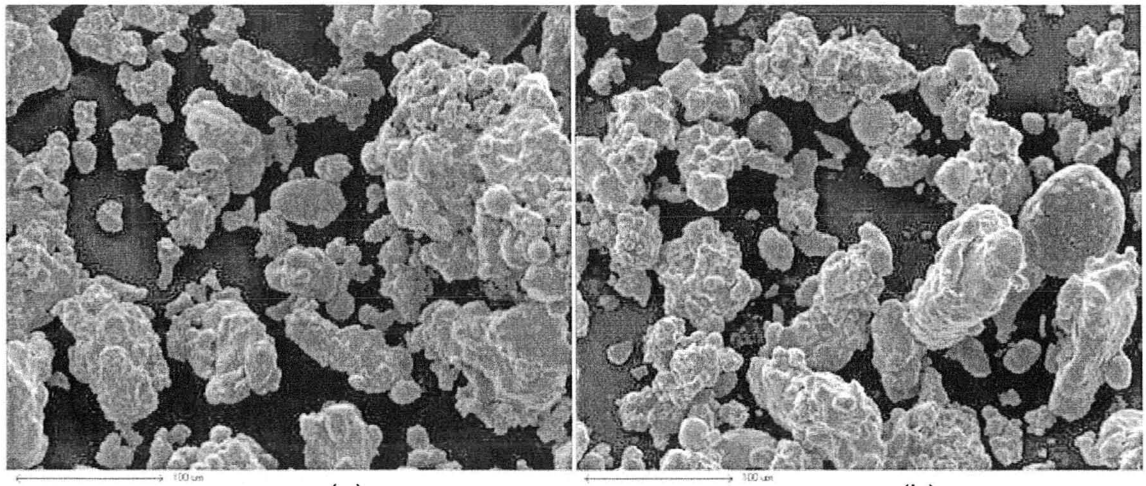

(a) (b)

Figure 3-1. Scanning electron microscope images of (a) ATOMET 1001 powder, (b) powder mixture SL5506.

3.1.2 Mechanical Test System

In this study, die pressing is used as the method of compaction. The mechanical setup consists of two major parts: A dual-actuator servo-hydraulic mechanical test machine (MTS) and a P/M compaction die set consisting of top and bottom punches and a die. The punches are attached to the two actuators, as shown in Figure 3-2 (a). The P/M compaction die set is made of hardened mild steel. As shown in Figure 3-3 (a), the compaction die unit is attached to the support columns by using the screws so the die will not move under load. Subsequently, a reinforced design with a support frame was built to allow for a more stable compaction with higher compaction load, as shown in Figure 3-2 (b) and Figure 3-3 (b).

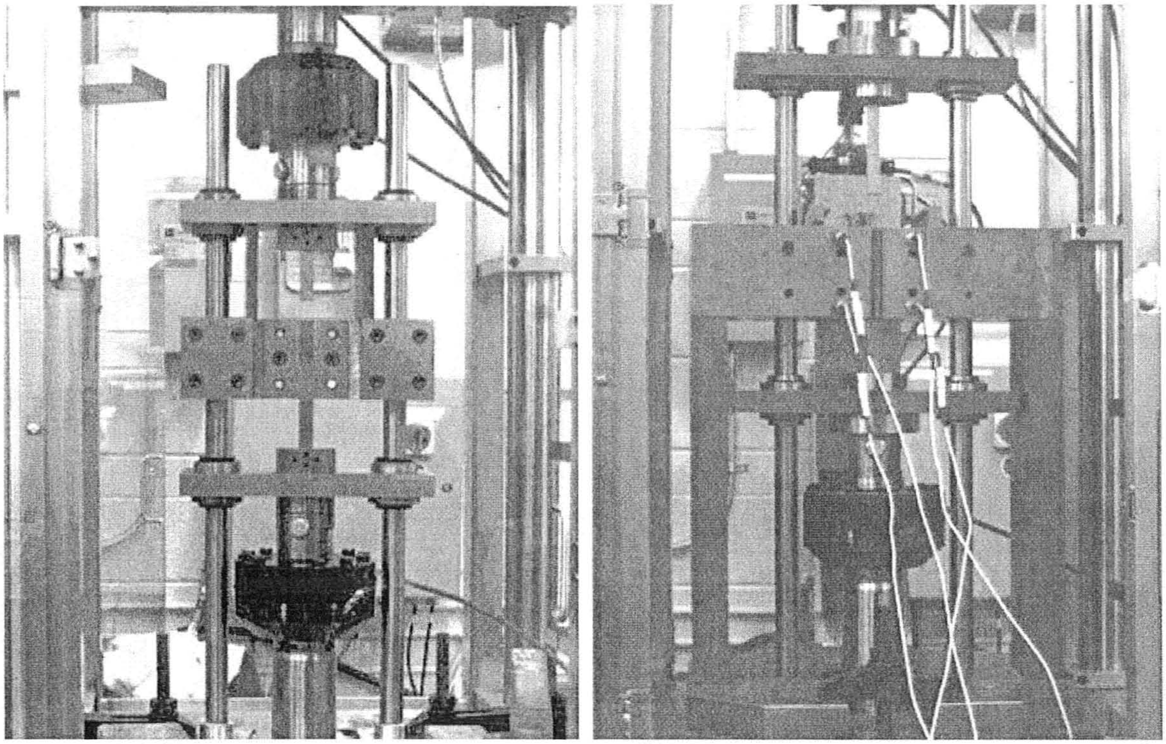

(a) (b)

Figure 3-2. Photographs of experimental setup with rigid die and MTS press frame for compaction test (a) first design, and (b) reinforced design.

The MTS hydraulic double action mechanical system which has a limit of 24000 lbs is controlled by ITC Unitest software through a computer which can control the maximum pressing load or the traveling distances of the two punches. This software also enables a recording of load and displacement of the punches from a load cell and a linear variable differential transducer (LVDT) respectively to which the two punches are connected via the hydraulic actuators. Recorded punch load and punch displacement traces will be presented in the results chapter.

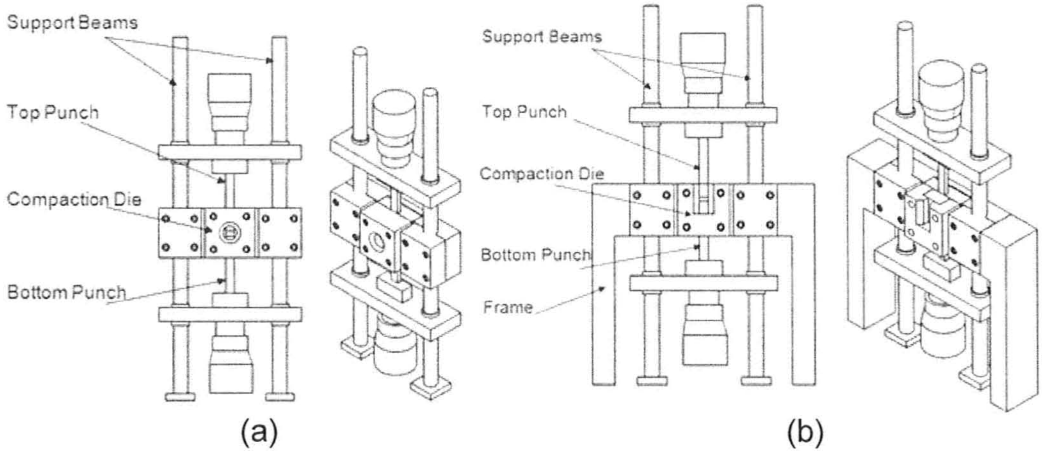

Figure 3-3. A two actuators MTS test frame with compaction die – top and – bottom punches (a) first design, (b) reinforced design.

In both die sets, the compaction die cavity can be opened by unscrewing a set of 4 screws on the compaction die and removing the compaction die cover, as shown in Figure 3-4 (a). The die cavity needs to be open to reduce friction during part ejection. The die cavity width is 15.24 mm (0.6 inch) for the first design and 14.73mm (0.58 inch) for the reinforced design, the depth is 7.62 mm (0.30 inch) for the first design and 8.13 mm (0.32 inch) for the reinforced design which is also the nominal width and thickness of both sets of punches respectively, (see Figure 3-4 (b)).

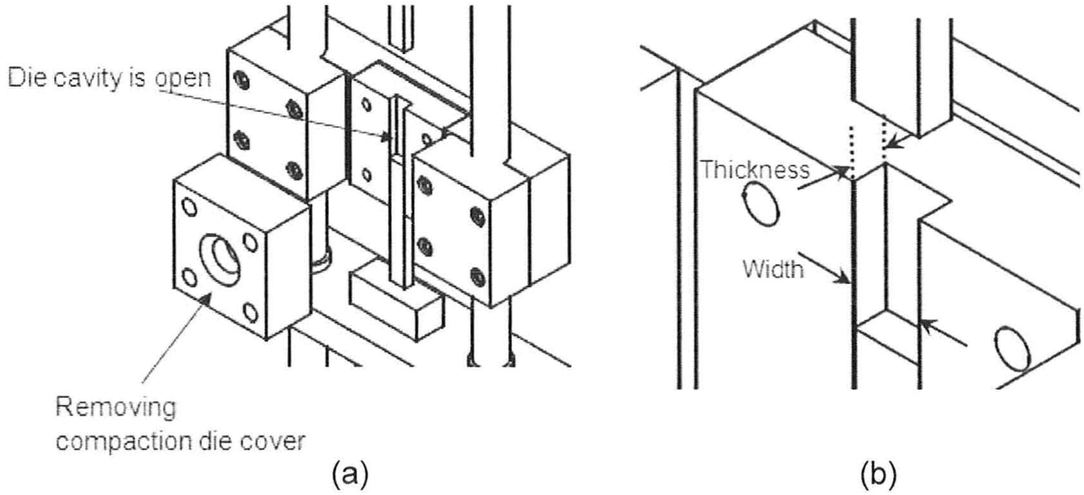

Figure 3-4. A close up of die with die cover plate removed.

A transparent glass window is incorporated on one side of the die to observe the filling and compaction processes during the test and to record the process by using cameras, as shown in Figure 3-5. The glass has a safe compressive load limit of 5000 lbs in both designs.

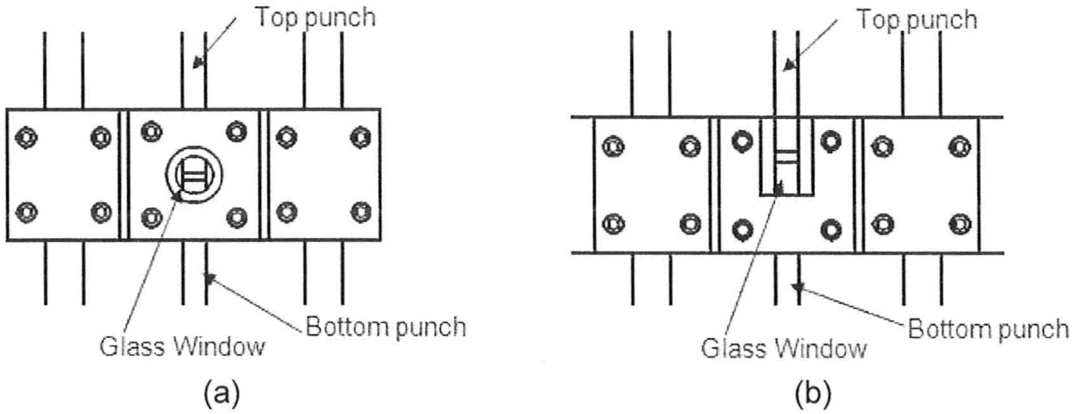

Figure 3-5. A close up of the transparent glass window, (a) first design, (b) reinforced design.

3.1.3 Image acquisition and analysis - ARAMIS system

3.1.3.1 ARAMIS camera setup

ARAMIS is a useful and robust optical system for analysing the development of strains in complex materials and structures during loading. The system provides a full-field, non-contact spatial and temporal displacement and strain data based on the principle of digital image correlation (DIC) [GOM, 2009].

The compact under load is viewed by one CCD camera. The powder particles act as a "pseudo" speckle pattern which deforms along with the compact during the compaction process. The deformation of the compact under different loading conditions is recorded by the CCD camera. The initial image processing defines the macro-image facets. These facets are tracked in each successive image with sub-pixel accuracy. Using photogrammetric principals, the coordinates of the surface of the compact which are related to the facets at each stage of load can be calculated precisely [ARAMIS manual, GOM 2009].

A Schneider CCD-1300BG camera, as part of the ARAMIS system, captures a series of images of the powder body through the transparent glass window. The light reflected from the surface of the object, an important condition, directly influences on the quality of images. In the absence of special lighting, the poor quality images resulted in either false result or no result. Therefore, a light was incorporated in the test setup to improve the image quality. A photograph of the experimental setup is shown in Figure 3-6.

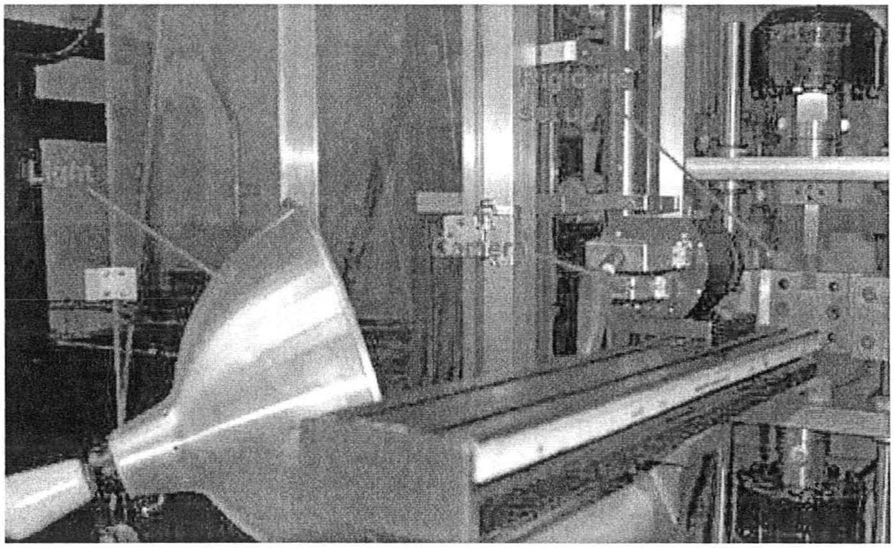

Figure 3-6. ARAMIS camera setup with light.

3.1.3.2 Image recording

ARAMIS system can be set up to take a series of images during a compaction test each separated by a pre-selected time interval. However, in order to capture powder particle movements during the entire process, a new data analysis procedure within the existing digital image correlation (DIC) methodology was introduced. This procedure is discussed next.

3.1.3.3 Digital Image Correlation (DIC) method with re-meshing procedure for strain calculation

Large deformation of the powder during compaction, small gray level gradient, the pixel sizes in the image close to the particle size at large deformations, and the hourglass effect of the facet size are the many causes which result in the strain calculations to stop. A facet size chosen at the beginning or the analysis is insufficient to analyze the entire compaction process. At the beginning of the compaction, the powder particles are clearly seen in the images. The particles are pushed by both top and bottom punches and move towards the middle. The strain calculation, however, stops shortly after as a result of unsteady facet deformation and hourglass effect. Therefore, a re-meshing procedure is implemented to carry out the image analysis till the end of the compaction process. This process is discussed below.

The re-meshing procedure essentially divides the entire set of recorded images into *n* steps. In order to have the same number of facets, a facet size and a facet pitch are assigned to each of the steps for the purpose of continuous reliable strain calculations at each step. For one compaction process, depending on the compaction ratio and compaction speed, it can take from 3 to 8 calculation steps. These strains are then added to obtain the total strain over the entire compaction process:

$$\varepsilon_{Total} = \varepsilon_{Step1} + \varepsilon_{Step2} + \varepsilon_{Step3} + \ldots\ldots \varepsilon_{Stepn} \tag{3-1}$$

This is referred to as digital image correlation with re-meshing (DICR) method.

3.1.3.4 Conversion of strain into green density

From mathematical point of view, assuming the compaction process to be a constant mass process, the current mass, volume and density (m, v and ρ) can be expressed as:

$$m = m_o \text{ and } m = v\rho\ ,\ \text{so } v\rho = v_o\rho_o \tag{3-2}$$

where m_o, v_o and ρ_o are the initial mass, volume and density respectively. Taking logarithms of two sides of the above equation, the constant mass equation yields:

$$ln(v/v_o) + ln(\rho/\rho_o) = 0 \tag{3-3}$$

where $ln(\rho/\rho_o)$ is the logarithms of the relative density and $ln(v/v_o)$ is the volumetric strain ε_V. Volumetric strain is expressed as:

$$\varepsilon_V = \varepsilon_h + \varepsilon_w + \varepsilon_b \tag{3-4}$$

where ε_h, ε_w and ε_b are the strain along in height (or axial), width and length directions respectively (see Figure 3-7).

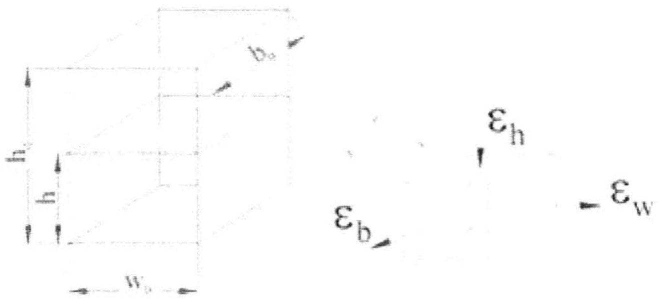

Figure 3-7. A demonstration of a rectangular compact specimen with strain state causing volume change.

Since ε_h is the axial strain and ε_w and ε_b are zero due to fixed width and length of the die, one obtains from equations (3-3) and (3-4),

$$\varepsilon_V = \varepsilon_h = -ln(\rho/\rho_o) \tag{3-5}$$

Equation (3-5) relates density to the axial strain [German, 1994; Hua, Cocks, 2001; Qin et at., 2006 and Alves et al. 2006].

The constant mass assumption was utilized to convert the true compaction strain obtained from the axial powder compression tests to powder density. Equation (3-5) can be rewritten to yield the density of the green compact as follows:

$$\rho = exp(-\varepsilon_h) * \rho_o \tag{3-6}$$

where ρ_0 and ρ are the initial and current density of the powder compact. The axial strain ε_h, can be calculated using ARAMIS system.

3.1.4 Load cell bolts

Load cell bolts are incorporated in the test setup to measure preload due to clamping of the front and back plates in the die assembly and to monitor the transverse load generated by the compact body on the die wall during the compaction process. Load cell bolts are very useful in determining the effect of transverse loads. Four standard internally-gaged hex head cap bolts are adopted to replace the standard hex head bolts to fasten the die assembly. Each bolt is proof-loaded to 7000 lbs and calibration certified from suppler within an accuracy of 99%. A photograph of one of the load cell bolts is shown in Figure 3-8.

Figure 3-8. A standard internally gaged hex head cap bolt [Strainsert, 2009].

The load cell bolts were interfaced with the ITC Unitest computer system with the MTS frame to continuously record the loads during the test. Under the condition when the transverse load generated from compaction is larger than the clamping preload, the total transverse load is equal to the sum of four bolt loads during compaction.

3.1.5 Powder compaction test system inter-relationships

The inter-relationships among various components that make up the powder compaction system are shown schematically in Figure 3-9.

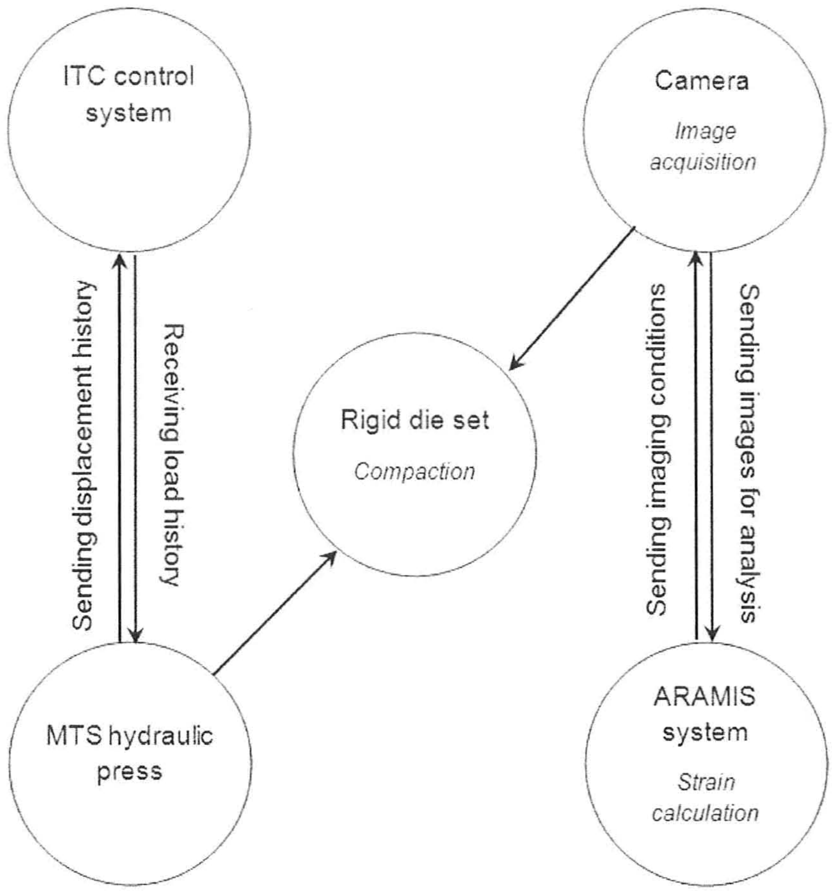

Figure 3-9. A schematic of powder compaction test system.

3.2 Metal Powder Compaction Test Procedure

3.2.1 Powder filling

There are two common procedures for die filling - gravity filling and suction filling. In gravity filling, the powder drops into the empty die cavity under its own weight as the shoe (container) moves across the die by a hydraulic arm, as shown in Figure 3-10. The feed shoe moves forward and backward to ensure the even distribution of powder. The lower punch, making up the "bottom" of the die, remains fixed in position.

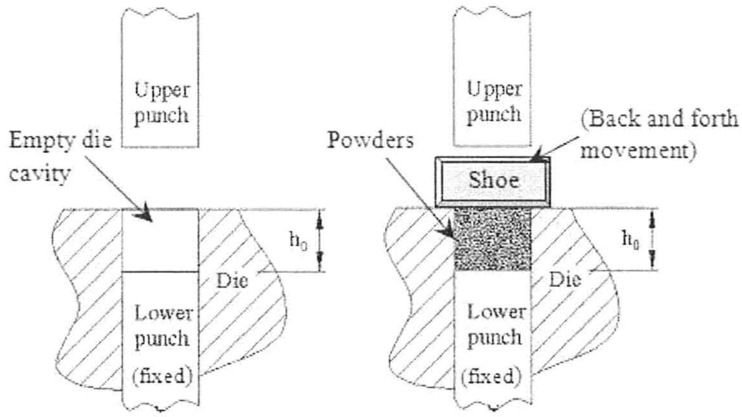

Figure 3-10. Gravity powder filling.

In suction filling, the shoe completely covers the die opening. The lower punch is then driven downward by the lower hydraulic actuator at a constant speed to create the empty die cavity and suction force as the powder is being delivered from the feed shoe into this die cavity, as shown in Figure 3-11.

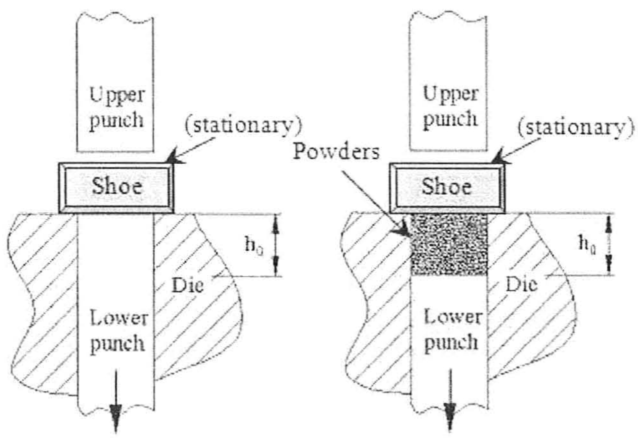

Figure 3-11. Suction powder filling.

3.2.2 Powder transfer

After the powder is filled into the die cavity, upper punch is moved down to contact the powder body and then the two punches move simultaneously downward to bring the powder to the compaction position, as shown in Figure 3-12. The transfer distance of the powders was selected to be 17.78 mm (0.7 in), which would bring the powders to the middle of transparent die section and have a high resolution for imaging via the ARAMIS on-line strain measurement system.

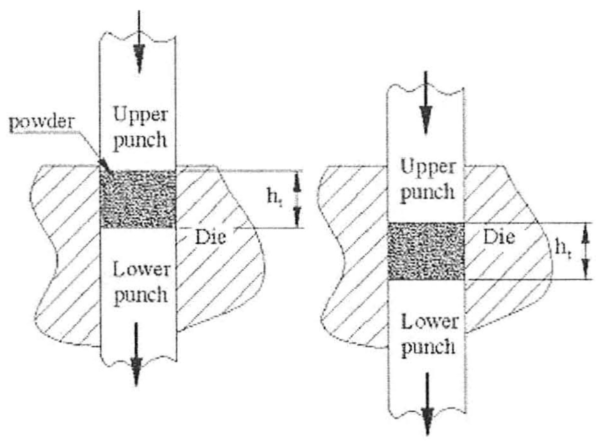

Figure 3-12. Powder transfer.

3.2.3 Compaction

3.2.3.1 Loading stage

Since different compaction mechanisms have different effects on the density distribution of the P/M parts, two compaction mechanisms are employed in our experiments, single and double action compaction. During the single action compaction, the top punch moves downward to compress the powder sample and the bottom punch is kept fixed in its original position, as shown in Figure 3-13.

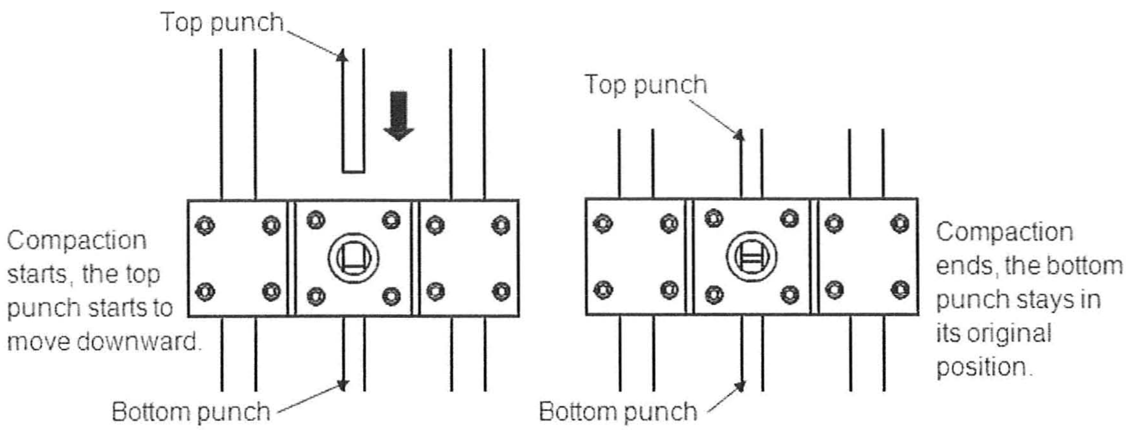

Figure 3-13. Single action compaction procedure.

To achieve more uniform density in the compact, double action compaction is preferable. During double action compaction, the top punch moves downward and the bottom punch moves upward at the same time and at the same speed to compress the powder sample, as shown in Figure 3-14.

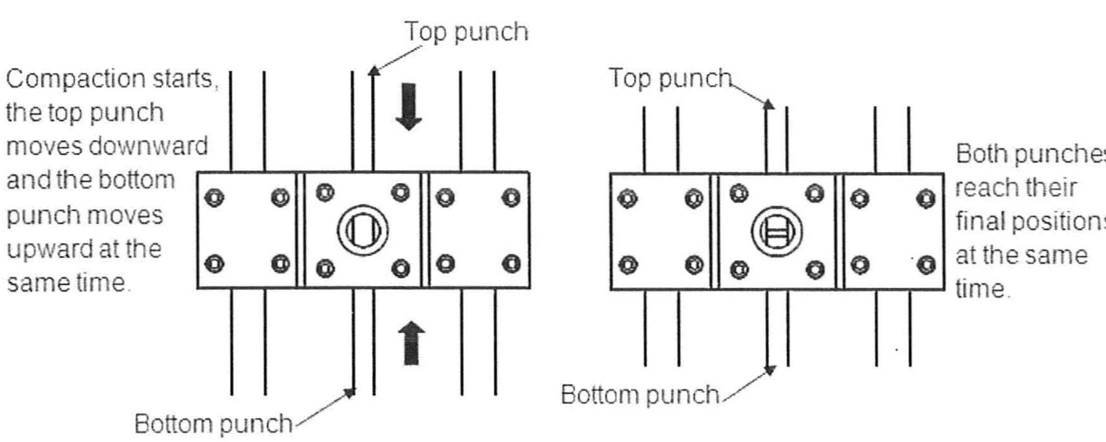

Figure 3-14. Double action compaction procedure.

3.2.3.2 Unloading stage

During the compaction process, the punches stop moving when they reach the pre-selected compressing distance. Since both punches are still under a large load, top punch is moved upward to release this load until the load reaches zero (see Figure 3-15). Note that the die cover is not removed during the unloading process and is not shown in Figure 3-15 for clarity. This unloading data is also recorded by using ITC Unitest system and will be presented in the next chapter on results.

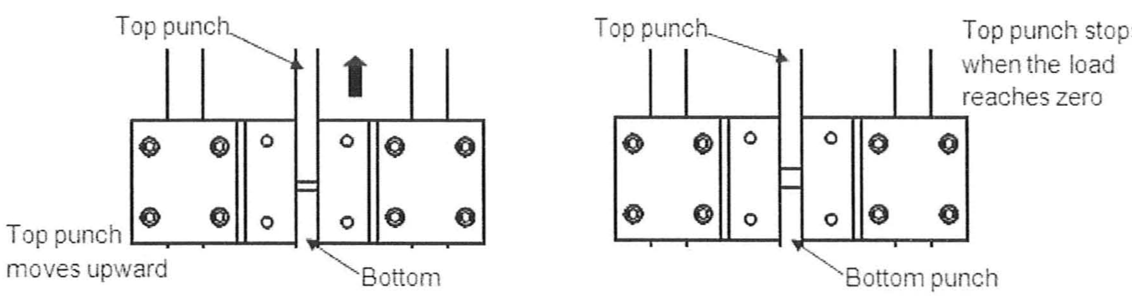

Figure 3-15. Unloading procedure.

3.2.3.3 Ejection stage

After the loading and unloading, the P/M sample is removed from the die. In order to protect the inside surface of the die cavity and the transparent glass window, and to reduce the friction before the ejection, the die cover plate is first removed. In the ejection process, the bottom punch is moved upward to push the P/M sample until it is out of the die cavity (see Figure 3-16). The load on the bottom is recorded.

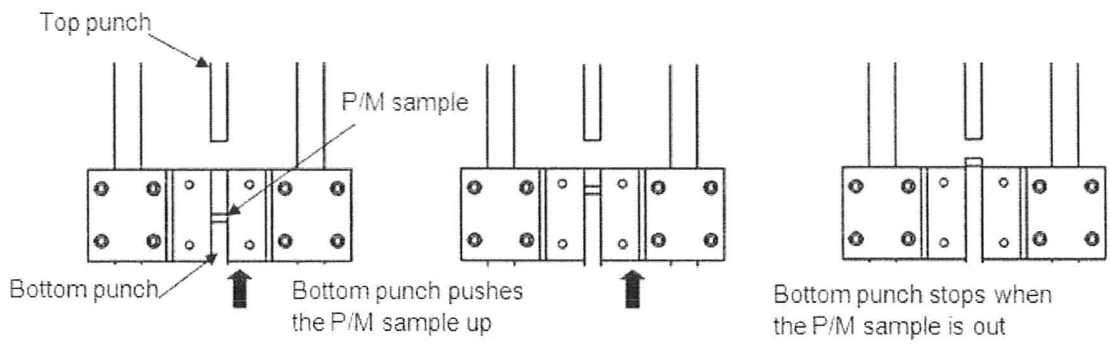

Figure 3-16. Bottom punch moves upward to eject the P/M sample.

3.3 Sample Density Measurements

3.3.1 Mass, volume and density

Immediately after the P/M samples are ejected and removed, the mass of each sample is measured using calibrated Acculab digital lab scale, VIC-212, and then using calliper the length, width, and height of each sample are measured. Each measurement is taken three times to yield an average value for each dimension. Finally, the density of each sample is calculated from average mass and average volume values.

3.3.2 Water emersion measurements

The other approach to get the density of compact sample is by using a water emersion measurement based on the Archimedes' method. A body is placed in the distilled water so that it undergoes an apparent loss of weight, which is equal to the weight of the water displaced. The scale setup with a gravity kit for these measurements is shown in Figure 3-17.

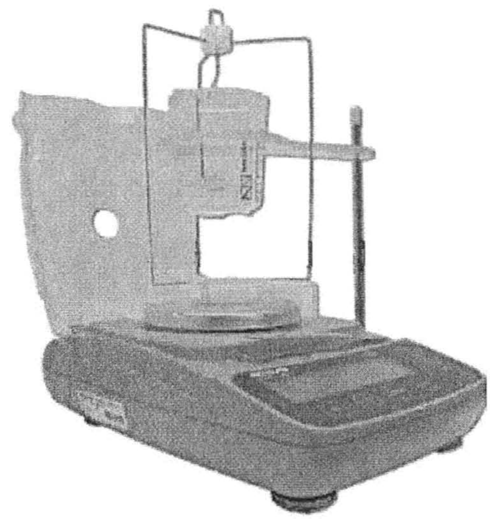

Figure 3-17. Laboratory scale with gravity kit [balances.com, 2009].

The weight of a compact in air is obtained first and then the weight of compact in the distilled water using the gravity kit. The density of compact is calculated as follows:

$$\rho_{compact} = \frac{W_{compact\ in\ air}}{W_{compact\ in\ air} - W_{compact\ in\ water}} * \rho_{\ water} \qquad (3\text{-}7)$$

where $\rho_{compact}$ is the density of compact, $W_{compact\ in\ air}$ and $W_{compact\ in\ water}$ are the weights of the compact in air and water respectively, $\rho_{\ water}$ is the density of distilled water at room temperature of 1.0 g/cm^3.

3.4 Micro-hardness Measurements

The Vickers hardness (HV) measurements on compacted iron powder samples are conducted using Vickers Hardness tester, Mitutoyo Entela MVK-H1. The measurement procedure is well documented in ASTM E92-82 standard [ATSM Standard E92-8, 2005]. In this work, a 1 kgf load is used and the P/M samples produced by double action compaction using SL5506 powder mixture are utilized.

Vickers Hardness measurements are taken at 6 different locations for each P/M sample of height, width and length of 7.11 mm, 8.13 mm and 14.73 mm (0.28 x 0.32 in x 0.58 inch) respectively. The locations of the measurements on each sample are qualitatively shown in Figure 3-18. Test result for each measurement is recorded and later processed to obtain an average Vickers hardness number.

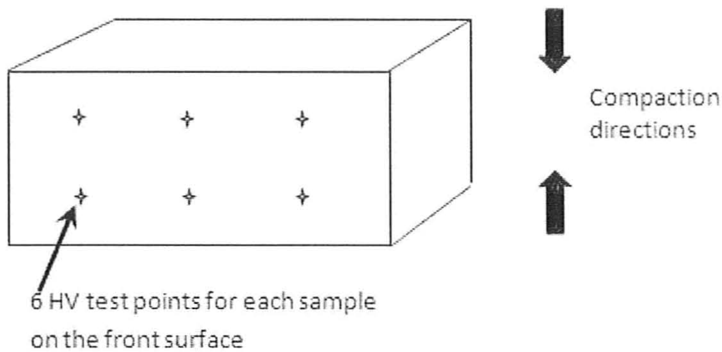

Figure 3-18. Orientation of Vickers Hardness measurements.

In the present work, a feasible experimentally validated measurement method for the density variations on a real P/M green part is developed based on correlation of green density with Vickers hardness number. These results are presented in the next chapter.

3.5 Surface Roughness Measurements

The surface roughness tests are conducted in the Micromachining Lab by using a contact profilometer, Mitutoyo Formtracer CS-5000CNC. This machine is a high-accuracy stylus type CNC surface measuring instrument that allows simultaneous measurement of surface roughness and form [Mitutoyo, 2009]. It is connected to a computer system which has full functions of recording measured data and roughness calculations. All of the surface roughness results in later sections are directly received from this computer system. The test parameters are shown in Table 3-2. P/M samples for surface roughness measurement are produced by double action compaction using SL5506 powder mixture.

Table 3-2. Surface roughness testing parameters.

Stylus tip radius	5 μm
Stylus tip angle	40^{0}
Measuring force	4 mN
Measuring speed	0.1 mm/s

Surface roughness measurements are taken at 3 different locations for each P/M sample of height, width and length is 7.11 mm, 8.13 mm and 14.73 mm (0.28 x 0.32 in x 0.58 inch) respectively. The locations of the tests on each sample are qualitatively shown in Figure 3-19. Test results for each measurement are recorded and later processed to receive an average surface roughness, Ra value, in micrometers. This value is the arithmetic average value of filtered roughness profile determined from deviations about the centerline within the evaluation length. Surface roughness can also be measured in terms of Rz value, which is the ten-point height or the absolute value of the five highest peaks and five lowest valleys over the evaluation length [ATSM Designation: B 946-06].

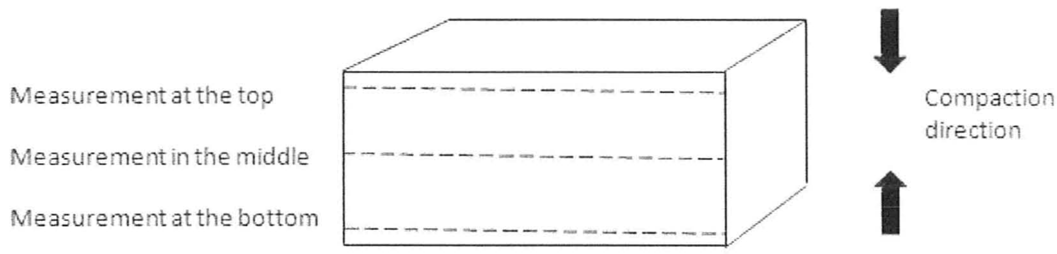

Figure 3-19. Orientation of surface roughness measurements.

A feasible experimentally validated measurement method for the density variations in a real P/M green part is also developed in the present work based on a correlation of green density with the average surface roughness, Ra value. These results are also presented in the next chapter.

Chapter 4

Experimental Results and Analysis

Experimental results and analysis of data obtained from powder fill, transfer and compaction experiments and subsequent analysis of compactions are presented in this chapter. Also, strain development in the compact during the test are illustrated in the form of strain maps. Further, the global and local density data obtained from different measurement techniques are presented.

4.1 Powder Filling Results and Analysis

4.1.1 Powder flow into the die cavity by gravity

To examine the influence of the motion of powder on the die filling process, a die cavity with a sapphire window has been designed as introduced in the previous chapter. The tests were carried out on an MTS 100 kN testing machine and coupled with strain measurement methodology based on digital image correlation (DIC). The flow analysis was limited to the area of compact observation to have a high resolution for imaging via the ARAMIS on-line strain measurement system. Therefore, the studies were conducted using rectangular die cavity geometry of 8.13 mm deep and 14.73 mm wide (0.32 x 0.58 inch) and the suction stroke (or initial powder material height) was kept constant at 16 mm (0.63 inch).

In order to measure the consistency (repeatability) of gravity and suction filling, 10 filling tests for each filling method were conducted and the weights of powder in the die were recorded. The gravity and suction filling experiments resulted in identical standard deviation values (see Table 4-1).

Table 4-1. Standard deviation of repeated die filling experiments.

10 fillings	Gravity filling (g)	Suction filling (g)
Test 1	5.96	6.098
Test 2	5.99	5.956
Test 3	5.97	5.923
Test 4	6.056	5.948
Test 5	6.318	6.092
Test 6	6.011	5.965
Test 7	6.024	5.949
Test 8	6.008	5.790
Test 9	6.005	6.063
Test 10	5.996	6.133
Average weight	6.03	5.99
Standard deviation	0.10	0.10

4.1.2 Powder flow during suction process

This study was concerned with experimental evaluation of non-homogeneous powder material flow and local granular distribution which is critical in production quality PM parts. The suction process was investigated by filling the die cavity with a fixed volume of powder. Also, the influence of suction speed on the mechanism of die filling was investigated. High speed CCD camera was utilized to observe the powder flow from the transparent die wall section. The suction tests were carried out at a rate of 0.635 to 50.8 mm/s (0.025 to 2.0 in/s). The frequency of the recorded images during the test was between 50 to 1000 fps. The particle distributions of PM material for different suction speeds are shown in Figure 4-1.

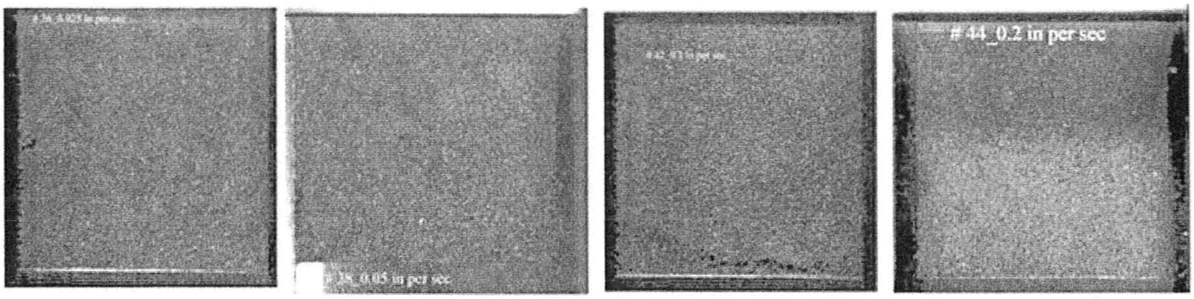

(a) 0.635 (0.025 in/s)

(b) 1.27 mm/s (0.05 in/s)

(c) 2.54 mm/s (0.1 in/s)

(d) 5.08 mm/s (0.2 in/s)

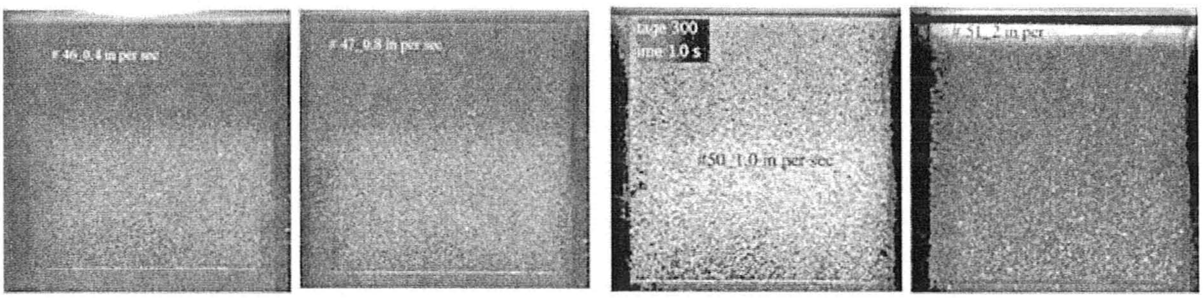

(e) 10.16 mm/s (0.4 in/s)

(f) 20.32 mm/s (0.8 in/s)

(g) 25.4 mm/s (1.0 in/s)

(h) 50.8 mm/s (2.0 in/s)

Figure 4-1. Particles rearrangement during suction fill (using SL5506 powder mixture).

The suction tests show that the powder material has a lot of pores along the side steel die wall. At a slow speed of ≤ 2.54mm/s (0.1 in/s), powder body exhibits many air pockets from the top to bottom of the die cavity. More uniform mass flow occurred at suction speeds of 5.08 to 50.8 mm/s (0.2 to 2.0 in/s). However, at lower speeds of 1.27 and 2.54 mm/s (0.05 and 0.1 in/s), Figure 4-1(b) and 4-1(c), one can see that at the bottom of die cavity the powder is in the loose state, while at the top of the die cavity the powder is tightly packed. The powder rearrangement during suction can be characterized by two zones: (i) uniformly packed region from the top to bottom of the die cavity and (ii) a region of high porosity close to the die walls (see in Figure 4-2). The die-wall high porosity region is formed due to interface friction.

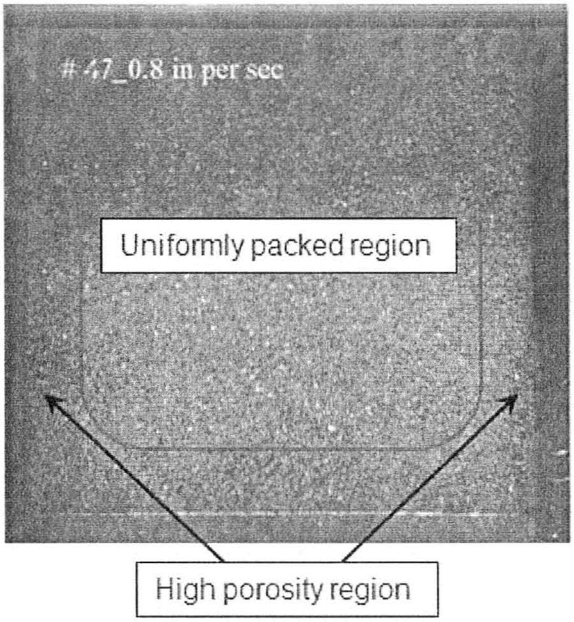

Figure 4-2. A closer look of uniformly packed region and high porosity region during suction fill (using SL5506 powder mixture).

Assuming that the density of the powder bed in a die after suction filling is uniform, an average suction weight m of 6.0 g (from Table 4-1), and a constant suction of 16 mm, the apparent density ρ_0 can be expressed as:

$$\rho_0 = m/V_s = 6.0/(0.813 * 1.47 * 1.6) = 3.14\ g/\ cm^3 \quad (4\text{-}1)$$

where V_s is the volume of PM after suction stage. This calculated apparent density value is in the range of SL5506 powder mixture density 2.98-3.18 g/cm^3 data supplied by Gates (see sub-section 3.1.1).

4.2 Powder Transfer Results and Analysis

4.2.1 Powder transfer at different speeds

The powder transfer results presented in this chapter were obtained with high speed CCD camera, which allowed monitoring of the powder transfer process. The underlying mechanisms that determine the global behaviour during the motion of particles in the die cavity were observed.

After the die-fill by the suction, as described in the previous section, the upper punch compressed the powder material from the height h_0 *of* 16.0 mm (0.63 in) to a height of h_t *of* 15 mm (0.59 in) to close the cracks and to reduce the air-filled pore volume, as shown in Figure 4-3 (b). More importantly, this pre-transfer step guaranteed the upper punch was lodged in the die cavity to prevent the upper punch from getting damaged due to any misalignment. The distance h_t was the starting distance between upper and bottom punches before compaction. The apparent density after transfer and before compaction is obtained as:

$$\rho_t = \frac{m}{V_t} = \frac{6.0}{0.813 * 1.47 * 1.5} = 3.35\ g/cm^3 \tag{4-2}$$

where ρ_t is the average transfer density, and V_t is the volume of powders after the transfer operation. Squeezed between upper and bottom punches, a constant volume of the powder was transferred to the compaction position in the middle of the die cativity. The transferred distance was held at 17.8 mm (0.7 in) for all of the tests.

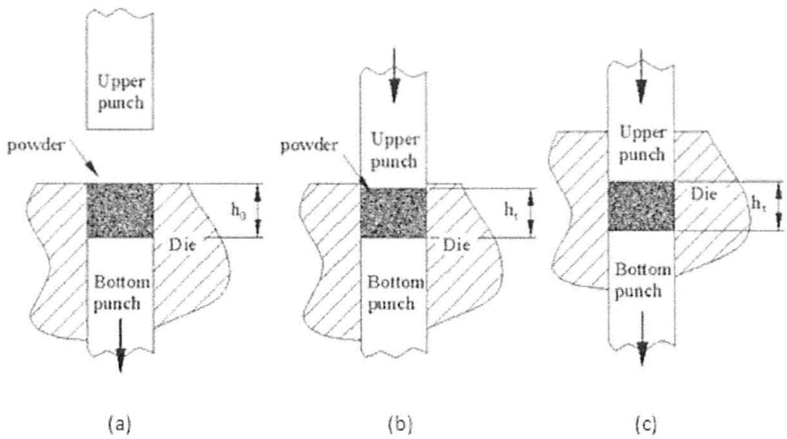

Figure 4-3. Diagram of powder transfer (a) after filling, (b) process of the crack closing, and (c) powder transfer.

The transfer tests were carried out using the same punch speed as in the suction filling step. During the transfer tests, a single-camera ARAMIS system continuously recorded images from the transparent region and later displacements versus time curve was plotted.

The images from a portion of transfer region were recorded during the tests carried out at a transfer speed of 0.635 mm/s (0.025 in/s). The powder material showed breaks close to the top of the die cavity as shown in Figure 4-4 (a). At a transfer speed of 1.27 mm/s (0.05 in/s) powder material showed breaks close to the bottom of the die cavity and this crack was seen from the beginning to end of transfer process as shown in Figure 4-4 (b, c).

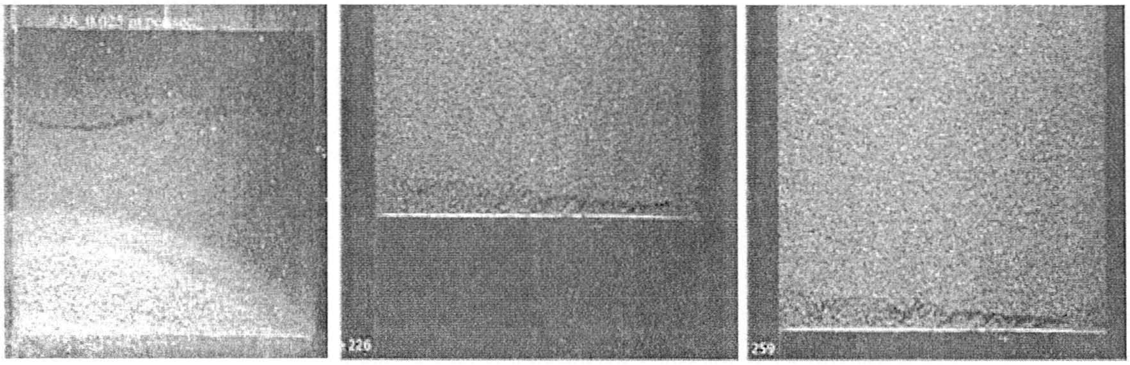

(a) 0.635 mm/s

(b) 1.27 mm/s

(c) 1.27 mm/s

Figure 4-4. Powder flow during transfer (a) transfer speed at 0.635 mm/s (0.025 in/s), (b) and (c) transfer speed at 1.27 mm/s (0.05 in/s) at the end of the suction (using SL5506 powder mixture).

The same results of a crack developed during powder transfer were obtained with a transfer speed of 2.54 mm/s (0.1 in/s) as shown in Figure 4-5. The results are presented in the form of a series of colour maps corresponding to different transfer distances where each colour represents a different displacement level.

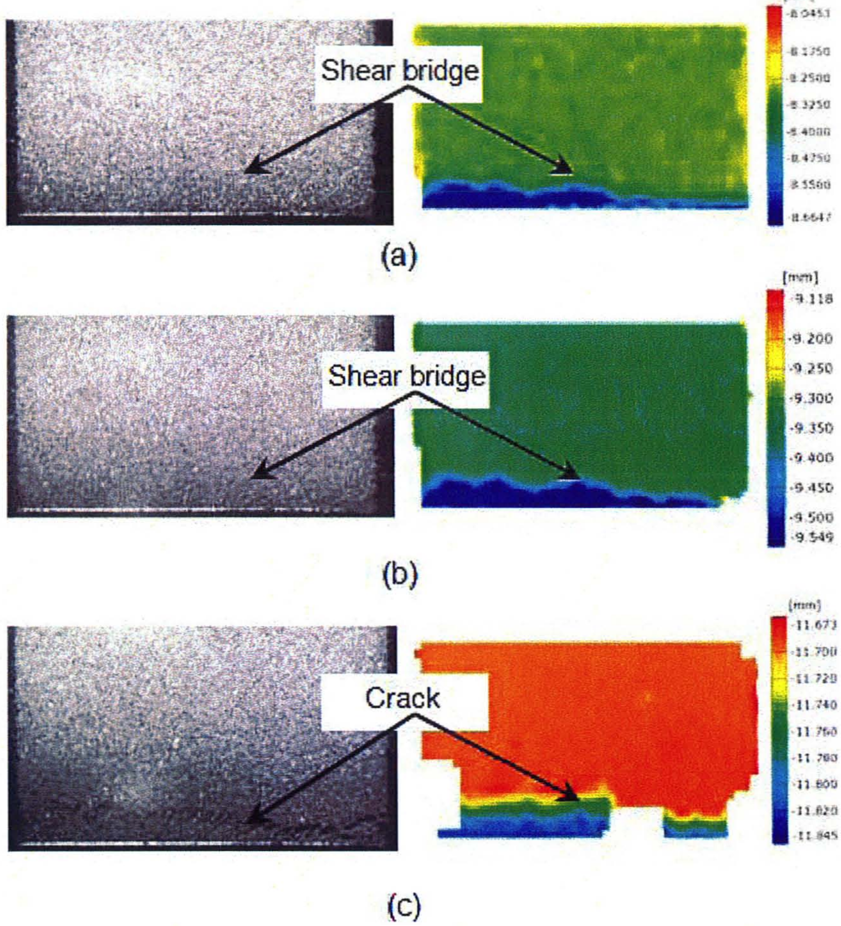

Figure 4-5. Powder transfer process with speed of 2.54 mm/s (0.1in/s) (a) transfer distance at 8.636 mm, (b) transfer distance at 9.398 mm, (c) transfer distance at 11.811 mm (using SL5506 powder mixture).

A series of experiments were also conducted at transfer speeds from 10.16 to 50.8 mm/s (0.4 to 2.0 in/s). Figure 4-6 shows a sequence of images of the powder movement recorded by the CCD camera at the end of the transfer process. The displacement field during the transfer process became more complex with increases in the speed. In summary, the powder body showed breaks at the end of process when the transfer speed was smaller than 5.08 mm/s (0.2 in/s) and higher than12.7 mm/s (0.5 in/s). However, when the transfer speeds were between 5.08-12.7 mm/s (0.2-0.5 in/s), as shown in Figure 4-6 (a) (b) and (c), and 50.8 mm/s (2.0 in/s), as shown in Figure 4-6 (f), well established and stable arc-shaped bridges without separation were observed. Also, at a transfer speed of 50.8 mm/s (2.0 in/s), a nearly uniform density in the powder resulted after the transfer process.

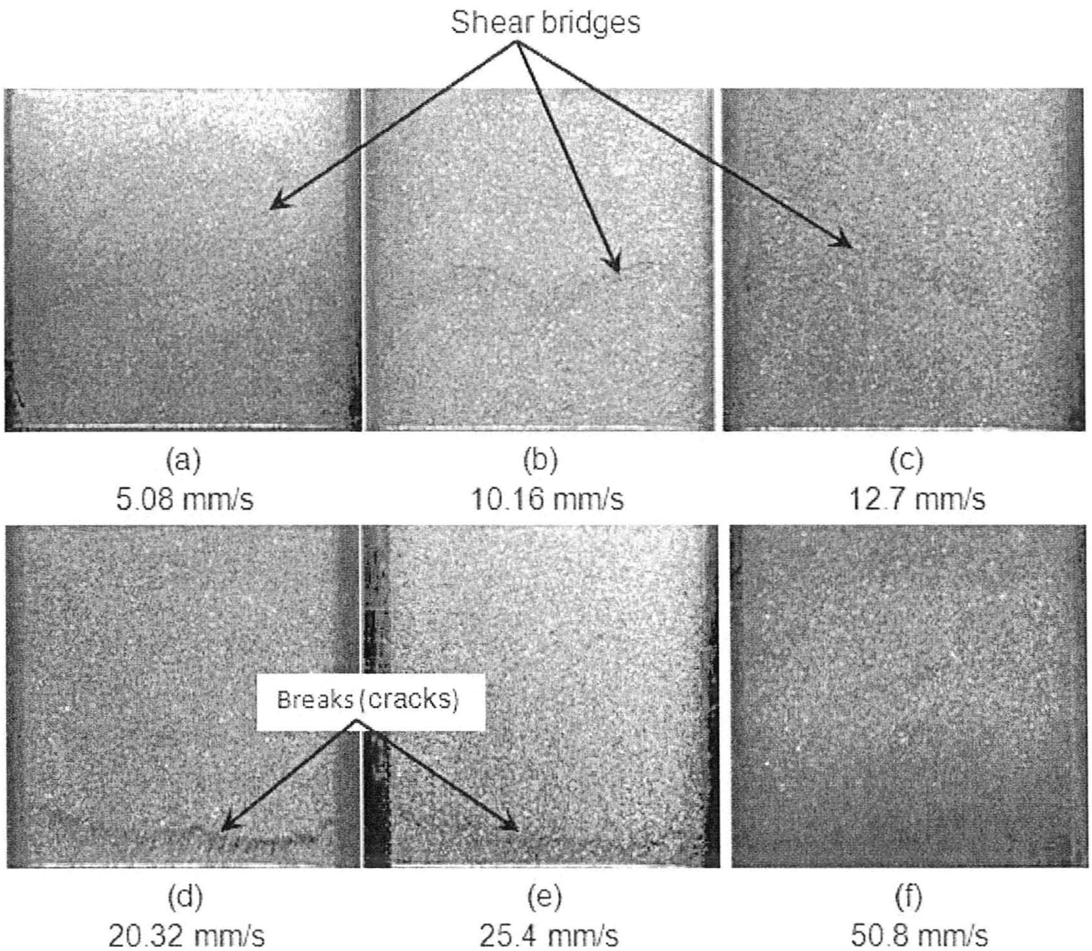

Figure 4-6. Powder flow during process at different transfer speed (a) 5.08 mm/s (0.2 in/s), (b) 10.16 mm/s (0.4 in/s), (c) 12.7 mm/s (0.5 in/s), (d) 20.32 mm/s (0.8 in/s), (e) 25.4 mm/s (1.0 in/s) and (f) 50.8 mm/s (2.0 in/s) (using SL5506 powder mixture).

4.2.2 Appearances of the shear bridges during transfer

At a transfer speed of 5.08 mm/s (2.0 in/s) powder material exhibited an arc-shaped shear bridge without separation as shown in Figure 4-7. This figure shows the intermediate stage during the transfer test, with several red spots indicating lower local displacement value compared to the other regions marked in green.

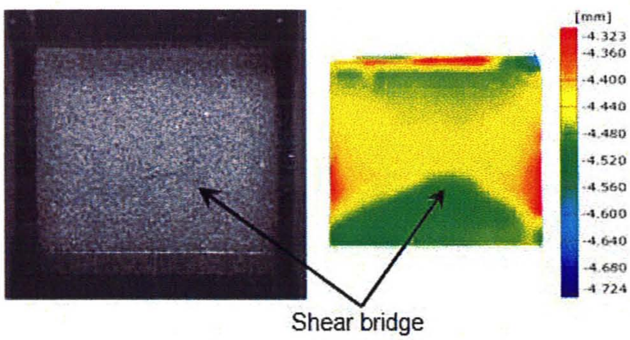

Figure 4-7. Powder flow during transfer with speed of 5.08 mm/s (0.2 in/s) and transfer distance at 4.58 mm (using SL5506 powder mixture).

As the transfer process proceeded, at a speed of 5.08 mm/s (0.2 in/s), a second arc-shaped shear bridge developed, as shown in Figure 4-8. The incremental displacement field shows that the arc bridges first form from the bottom and propagate to the top of the powder bed. Also, the shear bridge increases in width. The two bridges lead to intermittent flow which created three distinct flow regions; (1) a low displacement region at the top, marked in yellow, (2) an intermediate region between two bridges, marked in green, and (3) a high displacement region at the bottom, as shown in blue. The arc bridges are stable and this displacement fields exists until the end of the transfer process.

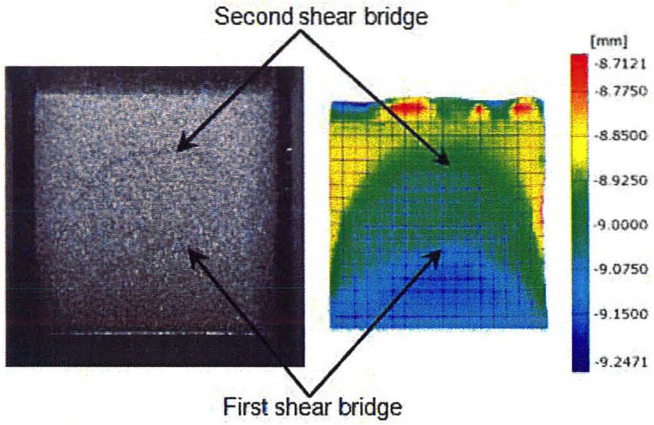

Figure 4-8. Powder flow during transfer at speed of 5.08 mm/s (0.2 in/s) and transfer distance at 9.144 mm (using SL5506 powder mixture).

As the transfer speed is increased further to 15.24 mm/s (0.6 in/s), the shear bridge developed along the powder body, as shown in Figure 4-9. The frequency of the recorded images during the test was 320 fps. The displacement map obtained from the digital images shows that the curved shear bridge propagated upwards from the bottom of the die wall. The displacements of the particles on one side of the shear bridge (dark blue region) were greater than those on the other side (light blue region).

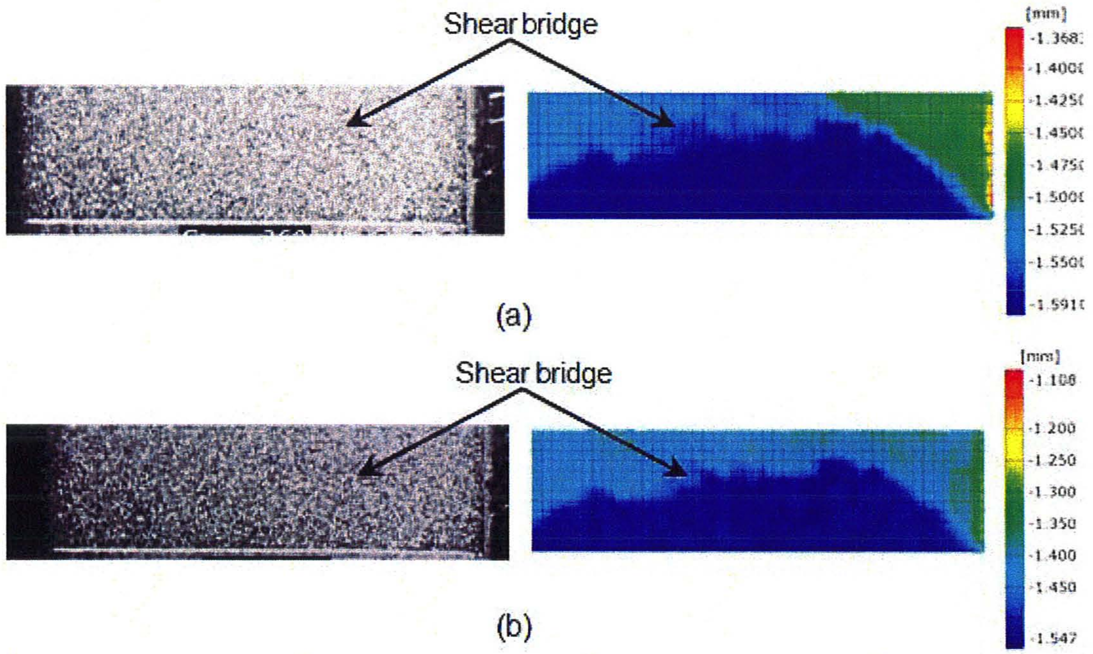

Figure 4-9. Powder flow during transfer with speed of 15.24 mm/s (0.6 in/s) (a) at transfer distance of 1.511 mm, (b) at transfer distance of 2.578 mm (using SL5506 powder mixture).

Image data at the transfer speed of 50.8 mm/s (2.0 in/s), with a very high image recording rate of 900 fps are shown in Figure 4-10. The results from the observed displacement map sequences show the formation and propagation of shear bridges. At this high speed, the shear bridges have a smaller profile compared with the previous slower transfer speeds. The displacement field in the powder body close to the bottom punch was lower than the displacement field close to the top punch. The gradient of displacement between each shear bridge is much smaller. This condition creates almost uniform packing density of the powder mass between shear bridges. In this case when the displacement of the material at the bottom is smaller and no break resulted in the powder body during the transfer process as shown in Figure 4-10.

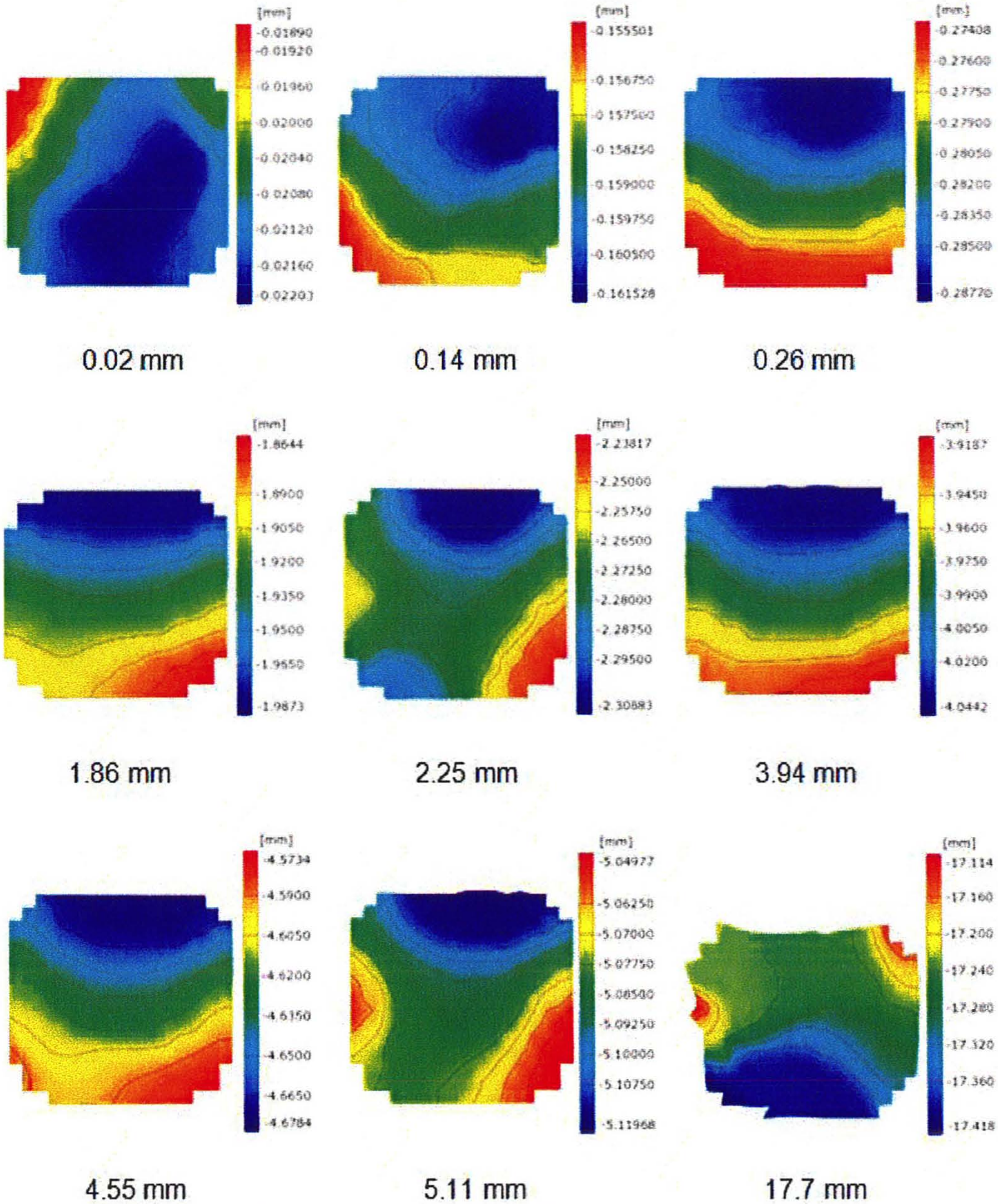

Figure 4-10. Displacement maps of powder at different transfer distance with speed of 50.8 mm/s (2.0 in/s) (using SL5506 powder mixture).

4.2.3 The effect of die wall friction during transfer

As the bottom punch starts to move downwards, friction develops along the steel die wall interface. Figure 4-11 shows flow patterns in powder transfer with only bottom punch moving at a speed of 0.05 in/s (1.27 mm/s). The recorded images during the transfer process shows that the powder material flows at a slower speed in a narrow area along the die wall.

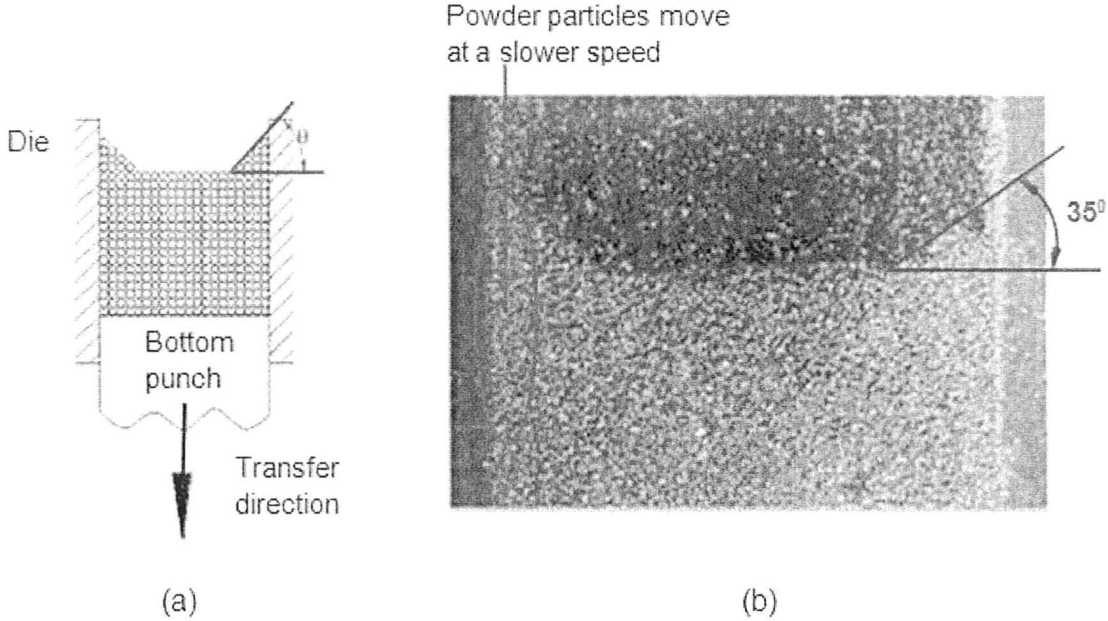

Figure 4-11. Position of powder particles during the transfer at speed of 1.27 mm/s (0.05 in/s) with only bottom punch moving.

The shear angle of powder movement is of practical interest. This angle is related to powder-die wall interface friction. The powder-die wall friction effect leads to the formation of two particle piles "friction hills" at the top of powder bed (see Figure 4-11 (b)). The powder pile angle with the horizontal was found to be 35^0 for powder mixture.

4.3 Powder Compaction Results and Analysis

4.3.1 Single action compaction

Single compaction was carried out by moving the top punch downward while keeping the bottom punch fixed at its transfer position. The load increases as the top punch moves to compress the powder. The load-displacement traces from three repeat compaction tests (tests #1-3) are shown in Figure 4-12. The unloading load-displacement data was not recorded during these tests.

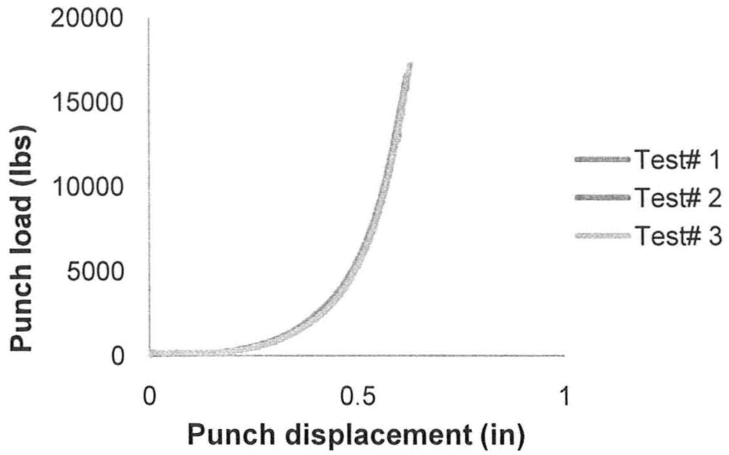

Figure 4-12. Load versus displacement curve of single compaction tests (using ATOMET 1001 powder with 0.7% Kenolube).

As showing in Figure 4-12, the 3 load and displacement curves have an identical shape. The final punch load and displacement values vary depending upon the compaction pressure. In the early stage of compaction, load increment with the punch displacement is small because the loose metal powder particles rearrange under load at this initial stage, there is no elastic or plastic loading of the powder particles. At the later stage, the powder undergoes bulk deformation, where material properties play an important role as there is elastic and plastic deformation (and work hardening) of the powder body. Therefore, the compaction load increment with displacement is much larger. It is to be noted that, for all compaction tests introduced in this chapter, the testing conditions and compaction pressures are presented in Appendix I.

4.3.2 Double action compaction

Double action compaction was carried out by moving the top punch downward and the bottom punch upward simultaneously into the powder body. Figure 4-13 shows the loading portion of load versus displacement curves for the top and bottom punches. Once again several repeat tests were performed. The loading starts at zero load and zero displacement, and as the punch moves to compress the powder, the load increases until it reaches a maximum. The trend of double action load versus displacement curve during loading is similar to the single action compression test and for all powder mixtures.

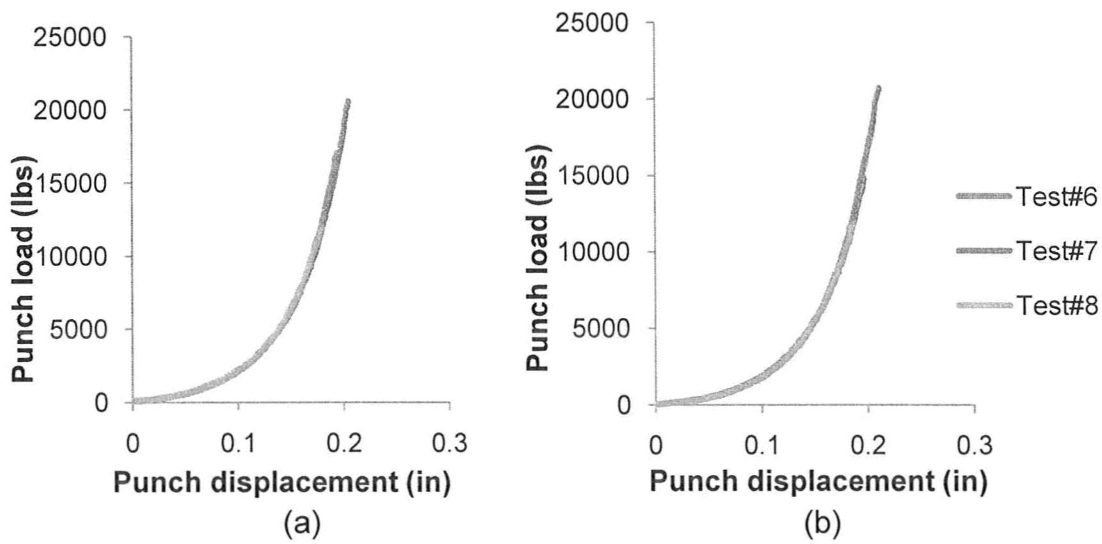

Figure 4-13. Load versus displacement curves for double action compaction tests (a) top punch, (b) bottom punch (using ATOMET 1001 powder with 0.7% Kenolube).

Figure 4-14 shows load versus displacement traces from the top and bottom punch for both loading and unloading. For unloading the bottom punch was kept stationary while the top punch was moved upwards and away from the compact. The unloading starts at the maximum pressed load and continues until the load drops to zero again. Once again the load-displacement traces from the tests are nearly identical in repeated tests.

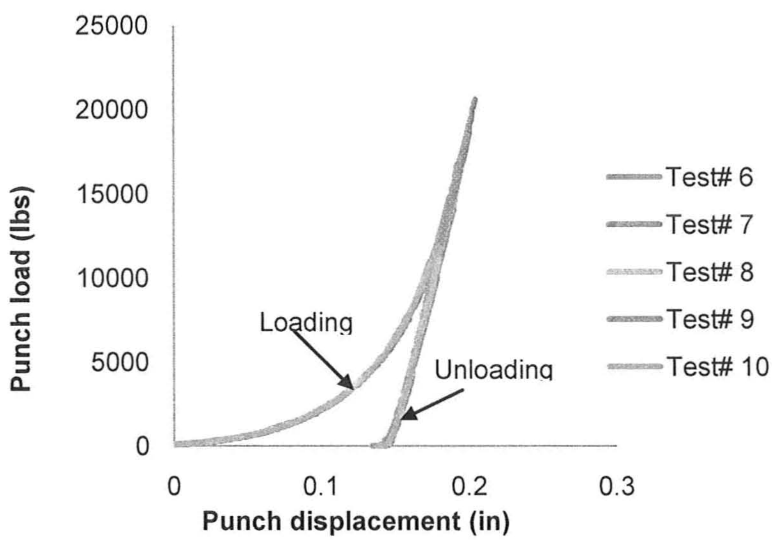

Figure 4-14. Punch load during loading and unloading steps versus displacement curve of double action compaction tests (using ATOMET 1001 powder with 0.7% Kenolube).

The unloading reflects the relaxation of the compacted part to release the elastic deformation energy generated from the compaction process. Since the die cavity is not open and the bottom punch does not move during unloading, the elastic relaxation is only permited in the vertical direction. The load of the bottom punch does not reach zero when the load on the top punch reaches zero. This is likely caused by friction between the P/M sample and the die wall which prevents the sample from moving upward to achieve a 'stress free' state at the bottom.

4.3.3 Strain history and strain distribution during compaction

4.3.3.1 Single action compaction – axial strain

The strain in the axial (loading) direction is perhaps more important because powder particles are primarily moving in this direction due to the axial movement of the punches. ARAMIS strain maps in the axial direction utilizing the re-meshing procedure discussed earlier in Chapter 3 are shown in Figure 4-15. These results are for 3 re-meshing calculation steps for a single action compaction experiment (test #11). As shown in Figure 4-15, the strain value decreases from the top to bottom portions of the compact due to the friction. This also means that there is more powder particles packing occurring at the top than at the bottom.

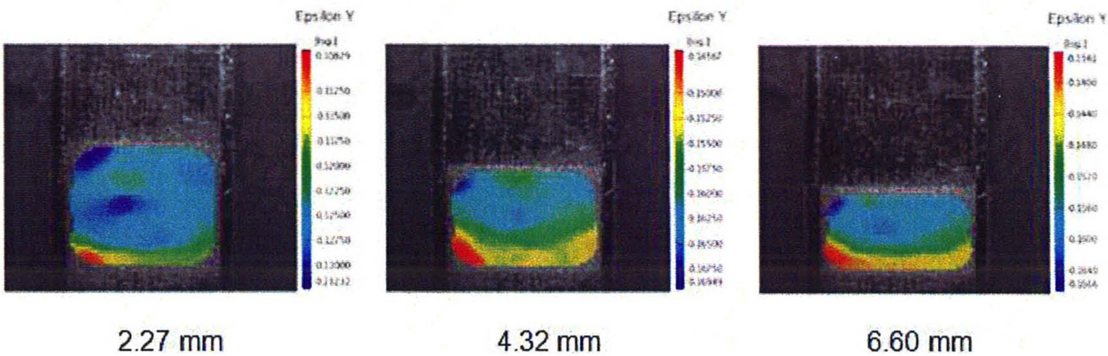

Figure 4-15. Strain map in axial (loading) direction for a single action compaction while top punch displacement at 2.27 mm (0.089 in), 4.32mm (0.170 in) and 6.60mm (0.260 in) (test #11, using SL5506 powder mixture).

The average compressive strain in the axial direction calculated in ARAMIS by using a line section measurement in the middle, is represented as a function of time is shown in Figure 4-16. The magnitude of compressive strain increases linearly with time while the top punch moves with a constant speed of 0.032 mm/s (0.00125 in/s). The unloading portion of the curve has a very small slope indicative of little change in strain during this stage. It is to be noted that for all the strain calculations the positive value of axial strain denotes compression.

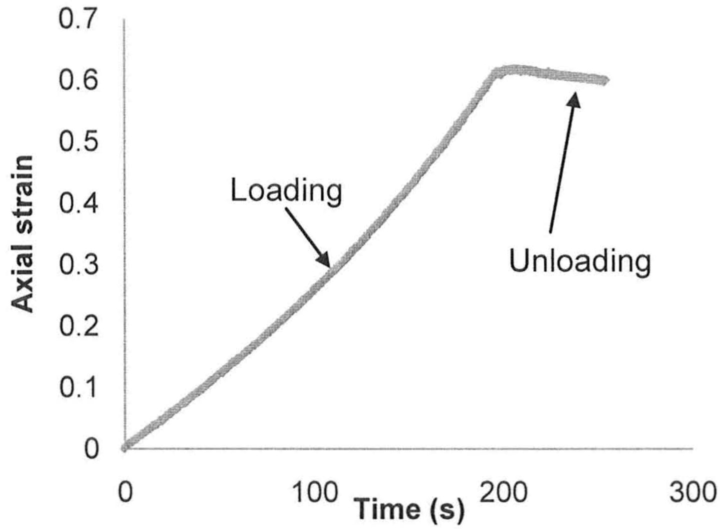

Figure 4-16. Average strain for a single action compaction in axial direction (test #11, using SL5506 powder mixture).

4.3.3.2 Single action compaction – transverse strain

The strain in the transverse direction is much smaller compared to the strain in the axial (or loading) direction as the powder particles are primarily moving in the loading direction. The overall strain in the transverse direction theoretically should be zero because the dimension in this direction is not changing at all. However, the powder particles are still moving in this direction due to the non-uniform filling and the friction between the die wall and the compact. The strain maps in transverse direction (test #11), as shown in Figure 4-17, illustrate that powder particles move without any clear trends. The average strain in the transverse direction as a function of time is shown in Figure 4-18. The magnitude of transverse strain is much smaller compared with the axial strain.

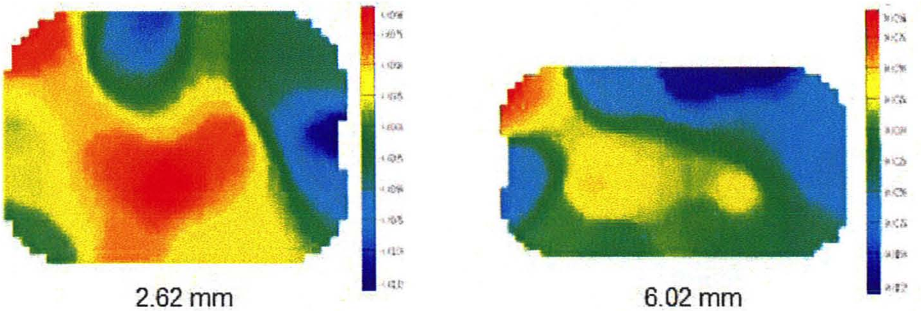

Figure 4-17. Strain map in transverse direction for a single action compaction while top punch displacement at 2.62 mm (0.103 in) and 6.02 mm (0.237 in) (test #11, using SL5506 powder mixture).

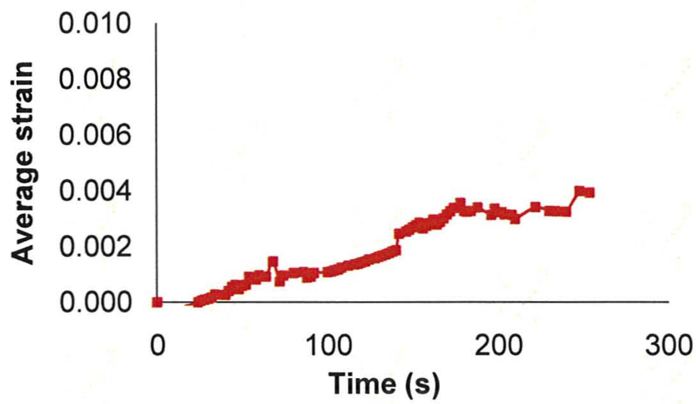

Figure 4-18. Average strain of a single action compaction in transverse direction (test #11, using SL5506 powder mixture).

4.3.3.3 Double action compaction – axial strain

ARAMIS strain maps for 3 re-meshing calculation steps for a double action compaction (test #12) are shown in Figure 4-19. The top and bottom portions of the compact have large axial strains which directly reflect that there is more deformation in these sections of the compact. This also means that there are more powder particles packing occurring at these locations. The average compressive strain in the axial direction as a function of time is shown in Figure 4-20. The magnitude of compressive strain increases almost linearly with time while the punches move with a constant speed of 0.032 mm/s (0.00125 in/s). Once again, the unloading portion of the curve is almost flat indicative of very little change in strain during this stage.

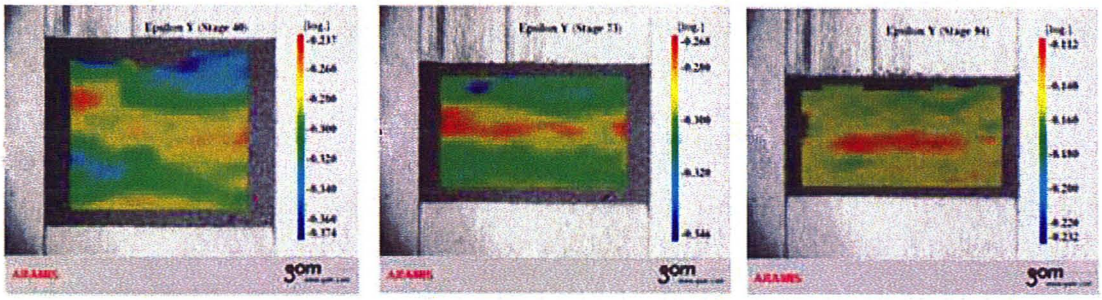

0.84 mm 2.10 mm 3.18 mm

Figure 4-19. Strain map in axial (loading) direction for a double action compaction while top punch displacement at 0.84 mm (0.033 in), 2.10 mm (0.083 in) and 3.18 mm (0.125) (test #12, using SL5506 powder mixture).

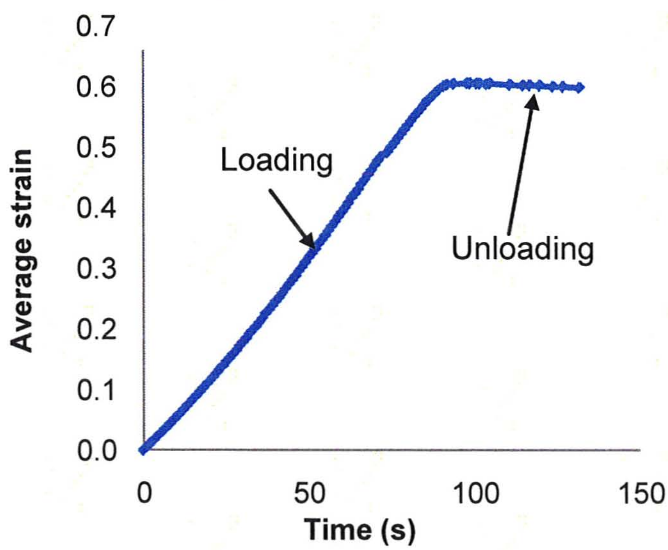

Figure 4-20. Average strain for a double action compaction in axial direction (test #12, using SL5506 powder mixture).

4.3.3.4 Double action compaction – transverse strain

The strain map in transverse direction after double action compaction (test #12), as shown in Figure 4-21, illustrates the local powder particles move away from the steel die wall during loading. The average strain in the transverse direction as a function of time is also shown in Figure 4-22. The magnitude of transverse strain is once again much smaller compared to the axial strain.

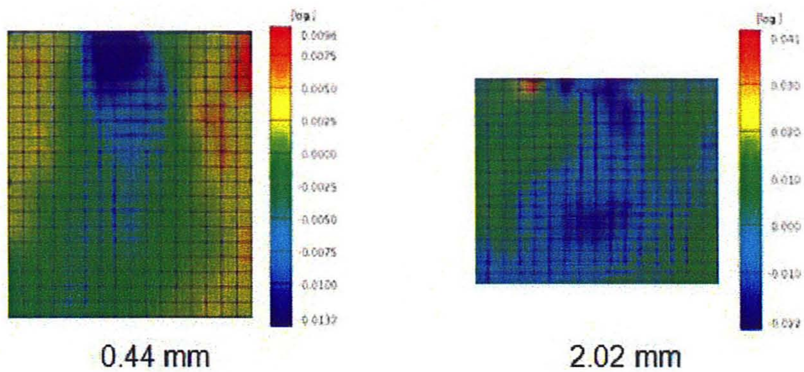

Figure 4-21. Strain map in transverse direction for a double action compaction while top punch displacement at 0.44 mm (0.017 in) and 2.02 mm (0.080 in) (test #12, using SL5506 powder mixture).

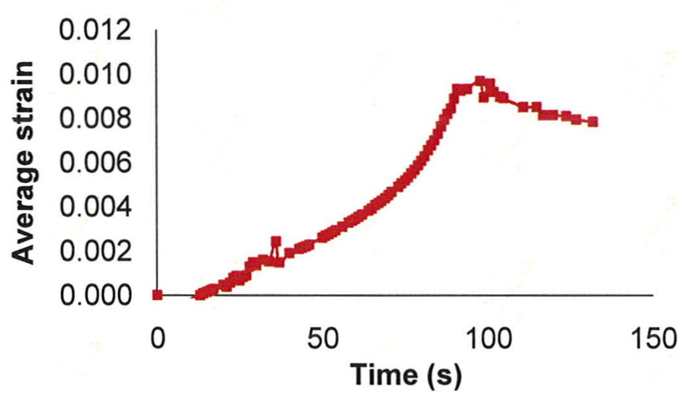

Figure 4-22. Average strain of a double action compaction in transverse direction (test #12, using SL5506 powder mixture).

4.3.3.5 Double action compaction – local strain analysis

Strain histories of three points at the top, mid-width, and at the bottom, along the middle of the compact for test (#12), were further analyzed to obtain the distribution of the local strains as shown in Figure 4-23 (a). For the re-meshing DIC method, after each calculation step, the reference points are reselected, so the specific points are not exactly the same points but they are in very close proximity to the previous chosen locations. So these specific strain points properly represent the local strain environment surrounding these points. The true local strains distribution across the powder surface can be seen in Figure 23 (b). The red dotted line represents the time when maximum axial strain reached and the start of unloading.

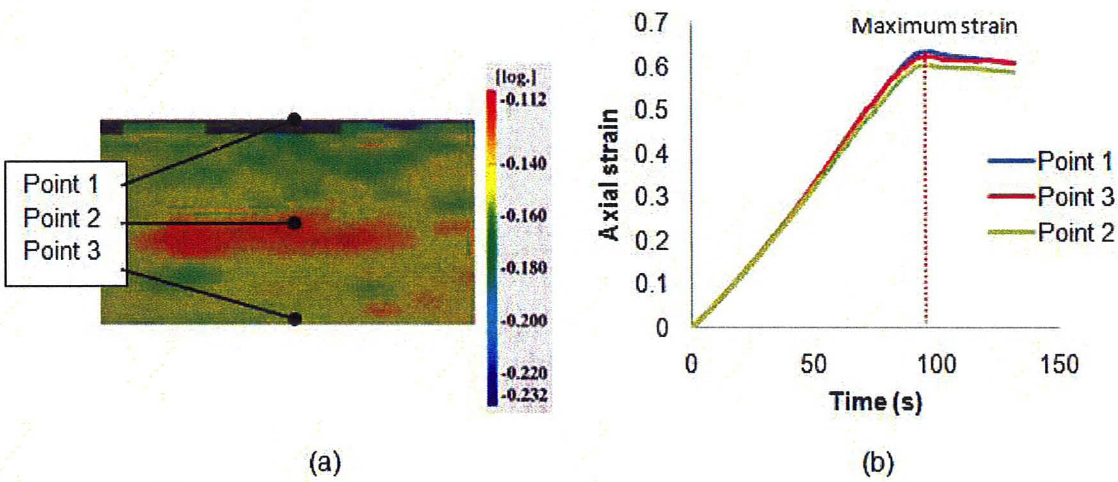

Figure 4-23. (a) Strain maps of the three local points, (b) the true local axial strains versus time (test #12, using SL5506 powder mixture).

An expanded view of the axial strain curve of these local points is shown in Figure 4-24. It is obvious that the points at top and bottom have slightly larger maximum axial strains than the point in the middle. Moreover, the middle and bottom points have slightly 'flatter' strain curves during unloading, which may be caused by the mechanism of unloading with only upper punch moving upward and lower punch keeping steady.

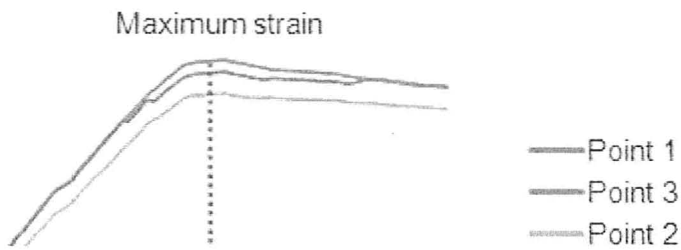

Figure 4-24. A closer look of the local axial strain (test #12, using SL5506 powder mixture).

4.3.4 Compaction with and without lubricant

The loads versus displacement traces for powder SL5506 with lubricant and ATOMET1001 with lubricant and without lubricant during double action compactions are shown in Figure 4-25 (tests #13-15). The ATOMET1001 powder without lubricant behaves differently from the other two powders with lubricant. At the same displacement, ATOMET1001 powder without lubricant shows a higher load compared to the case with lubricant. This is caused by increased powder die wall friction during compaction for the powder without lubricant. Addition of the lubricant reduces the friction between powder compact and die wall.

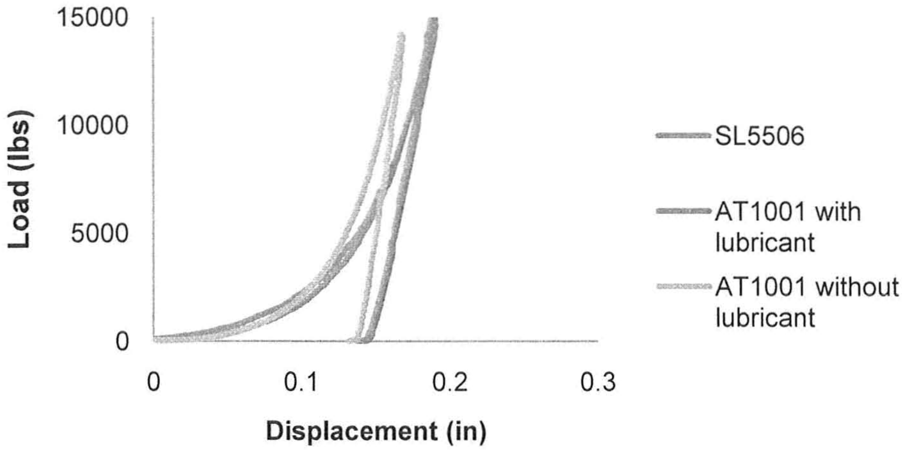

Figure 4-25. Load verses displacement for different powder mixutures (ATOMET1001powder, ATOMET1001 with 0.7% Kenolube powder mixture and SL5506 powder mixture).

4.3.5 Ejection of the compact

Ejection forces for double compaction tests (tests #6-10) described earlier as well as other tests (tests #16-19) are shown in Figure 4-26. The higher green density samples require higher ejection forces. Such higher ejection forces for very high density compacts can lead to cracking during part release. However, for the powders with lubricant the ejection forces are much less than those without the lubricant. Lubricant, therefore, plays an important in reducing the forces and in the occurrence of cracking in the compact.

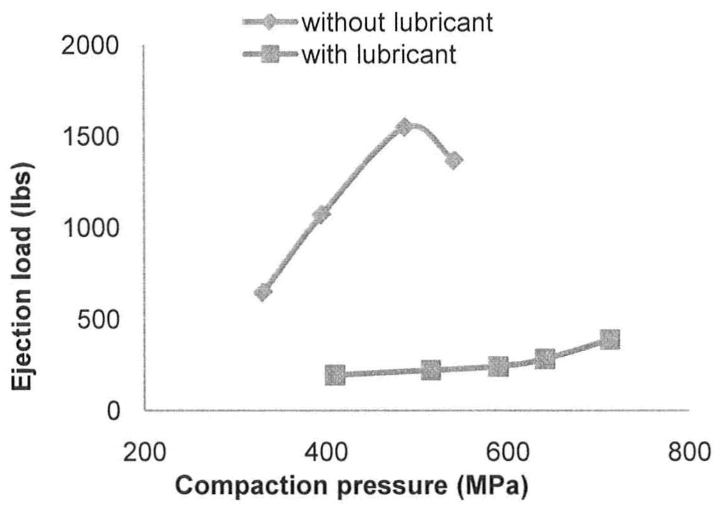

Figure 4-26. Ejection load verses compaction pressure for powders with & without lubricant (ATOMET 1001 and ATOMET 1001 powder with 7% Kenolube powder mixture).

The ejection forces increase with the compaction pressure although there appears to be an anamolous drop in the ejection force versus compaction pressure curve at a large compaction pressure for test without lubricant (see top curve in Figure 4-26). This may be attributed to die sliding on the support column due to a large friction that existed during ejection for powder without lubricant at a large compaction pressure. In order to protect the die compaction system, no further ejection experiments without the lubricant were carried out.

4.3.6 Relationship of compaction load and green density

Figure 4-27 shows a relationship between compaction load and green density in the form of measured data, a polynomial fit and a logarithmic fit to the data.

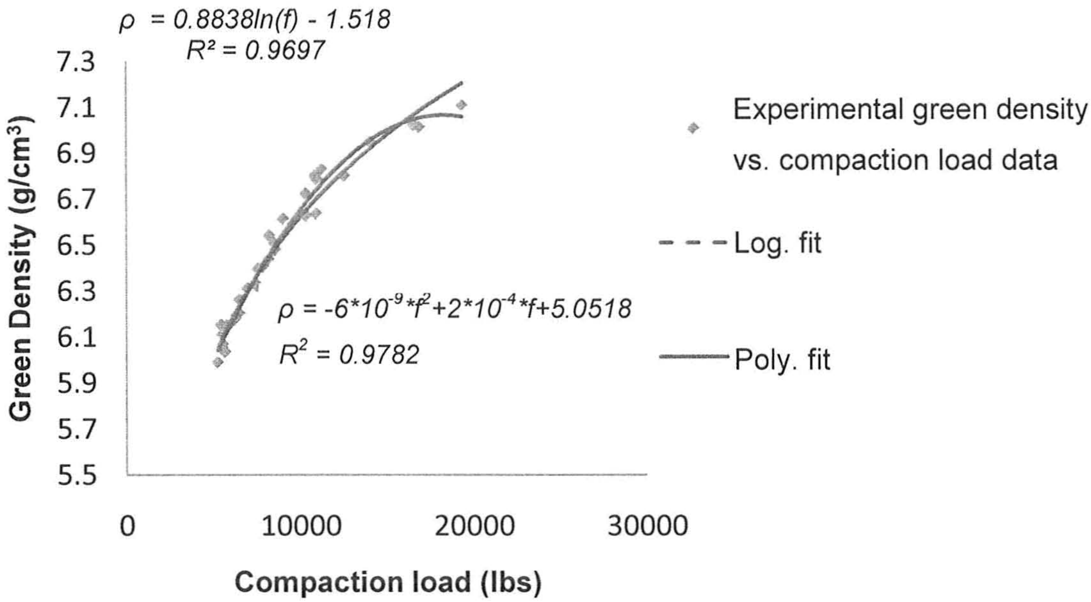

Figure 4-27. Relationship between compaction load and green density for 30 P/M samples (using SL5506 powder mixture). (see Appendix II for details)

In order to evaluate the goodness of fit, the R^2 coefficient of determination is adopted, which is a statistical measure of how well the regression line approximates the real data points. An R^2 of 1.0 indicates that the regression line perfectly fits the data. In Figure 4-27, all the data points are close to these trend lines and the R^2 value is calculated to be about 0.97 and 0.98 for logarithmic and polynomial fits respectively, which indicate that these trend lines are good fit to the data. However, for higher compact densities, the logarithmic regression line trends to move upward whereas the polynomial fit tends to be flat. The real data appears to lie between the two fitting functions.

4.3.7 Relationship between compaction pressure and green density

The compaction pressure and green density relationship is commonly utilized in the P/M industry to determine the characteristics of a certain type of powder mixture. This relationship for the powder mixture SL5506 from the present work is shown in Figure 4-28. A green density of 7.0 g/cm^3 was achieved using a compaction pressure of about 600 MPa. The pressure is calculated using the maximum compaction load divided by the cross section area of die cavity. The pressure and density relationship is also expressed in the form of the following logarithmic equation:

$$\rho = 0.8838\ ln(P) + 3.7964 \tag{4-3}$$

where ρ is the green density and P is the compaction pressure.

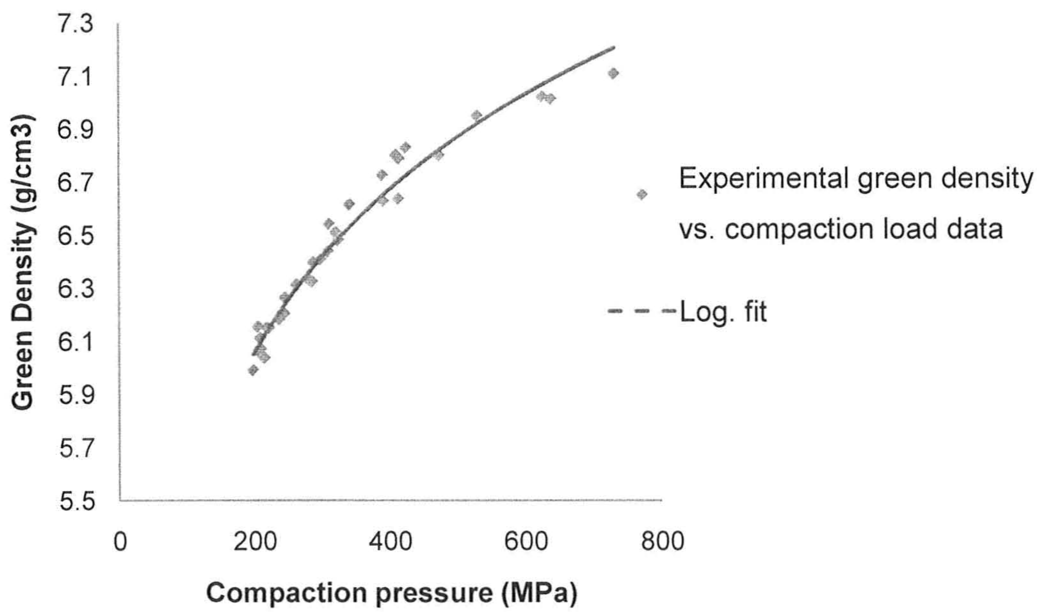

Figure 4-28. Relationship between compaction pressure and green density for 30 P/M samples (using SL5506 powder mixture). (See Appendix II for detail)

4.3.8 Relationship between compaction pressure and average strain during compaction

Compaction pressure versus ARAMIS axial strain curves during double action compaction are shown in Figure 4-29. As shown, the absolute average strain values in axial direction increase non-linearly with the compacting pressure in 2 separate compaction tests. The 2 compaction pressure curves are on the same trace during loading stage. Although, one of compaction tests (test #20, green density 6.32 g/cm^3) was stopped at a lower compaction pressure and unloaded. A comparison of unloading curves indicates that the unloading slopes are very similar and nearly linear.

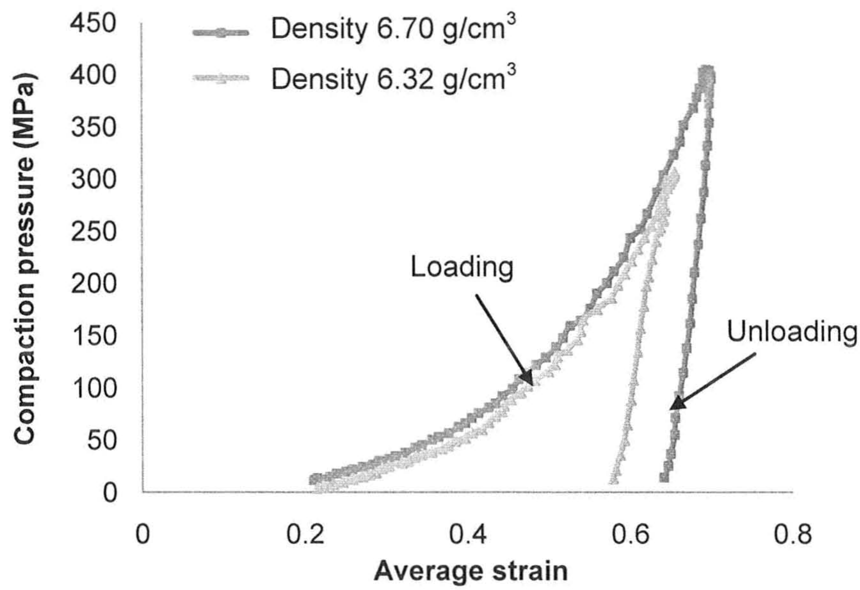

Figure 4-29. Average compacting pressure verses average strain in axial (loading) direction for 2 double action compaction tests (using SL5506 powder mixture).

4.3.9 Die wall friction during compaction

The equation 2-2 in Chapter 2 (Sinka et al, 2003) can be used to calculate the friction coefficient during powder compaction in a closed cylindrical die for single action compaction. In our case of a square cross-section die compaction, as shown as Figure 4-30, the equation can be modified as follows:

$$\mu = \frac{L}{4H}\frac{F_z^l}{F_T(z)}\left(\frac{F_z^u}{F_z^l}\right)^{\frac{z}{H}} ln\frac{F_z^u}{F_z^l} \tag{4-4}$$

where L is the die interior length, H is the compaction height in the die, $F_T(z)$ is the force in the transverse direction at the position z from the top surface of the powder compact, and F_z^u and F_z^l are axial compression forces applied by the upper and lower punches respectively. In this study, for compacted density ranges from 6.5 to 6.8 g/cm^3, the calculated friction coefficient is from 0.205 to 0.226 as shown in Table 4-2.

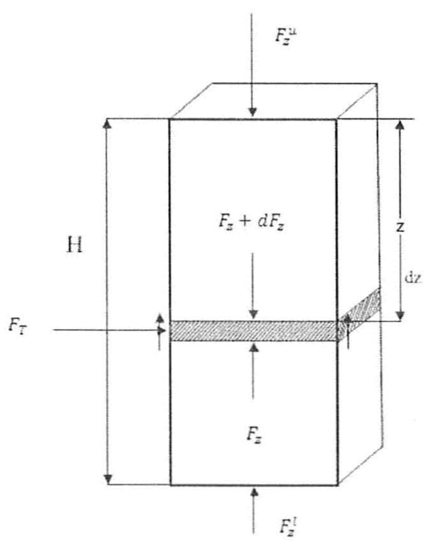

Figure 4-30. The analysis of die wall friction during compaction.

Table 4-2. Calculated die wall friction coefficient for three single action compaction tests using equation (4-4) (using SL5506 powder mixture).

Test	Density	friction coefficient	Length	Height of compact	Upper Load	lower Load	Transverse Load
#	g/cm^3	μ	L	H	F_z^u	F_z^l	F_T
22	6.675	0.205	0.583	0.289	11077	8742	5102
23	6.626	0.226	0.583	0.293	11373	8779	4996
24	6.754	0.211	0.584	0.288	11469	8877	5470

4.4 Green Density Measurement from Different Methods

4.4.1 Conversion of ARAMIS strain into density

The initial powder fill of the die cavity is non-uniform, and as a result powder particles move in axial and transverse directions during compaction. However, in closed die compaction the particle movement in the transverse direction, as noted earlier, is much smaller compared with the axial displacement. Thus, one can assume that there is no deformation in the transverse (i.e., width and depth) directions ($\varepsilon_W = \varepsilon_b = 0$). With this assumption the density of the compact can be related to the volumetric strain and by using equation (3-6), the green density of a sample (test# 25) with an axial strain of -0.613 is calculated as follows:

$$\rho = exp(-\varepsilon_h) * \rho_o = exp(0.613) * 3.35 = 6.18 g/cm^3 \tag{4-5}$$

Using the measured density of this compacted sample of 6.27 g/cm^3, the following percentage error in density can be obtained:

$$\rho_{error} = \frac{\rho_{measured} - \rho_{ARAMIS}}{\rho_{emasured}} = \frac{6.27 - 6.18}{6.27} = 0.032 = 1.4\% \tag{4-6}$$

In other words, the error of using the calculated axial strain from ARAMIS system to predict the green density of compact part is around 1.4% for the chosen test sample.

In order to evaluate the density distribution throughout the compaction, the green compact was cut into three slices using EDM, as shown in Figure 4-31 . The cutting operation consisted of one slice each from the top (#1), the middle (#2), and the bottom (#3) region of the compact.

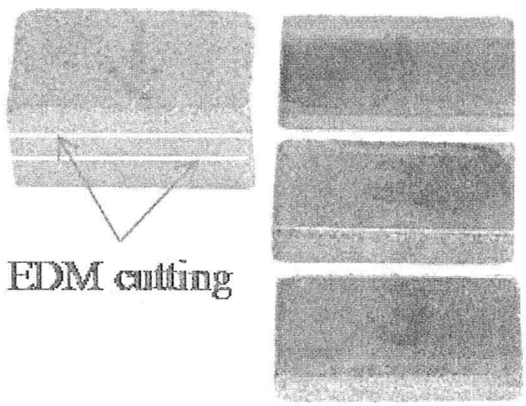

Figure 4-31. A photograph of a green compact cut into three slices by EDM (using SL5506 powder mixture).

The ARAMIS system has capability to provide the global average true strain in different regions of interest by using DIC method with re-meshing techniques as introduced in previous section 3.1.3.3. The results are shown in Figure 4-32.

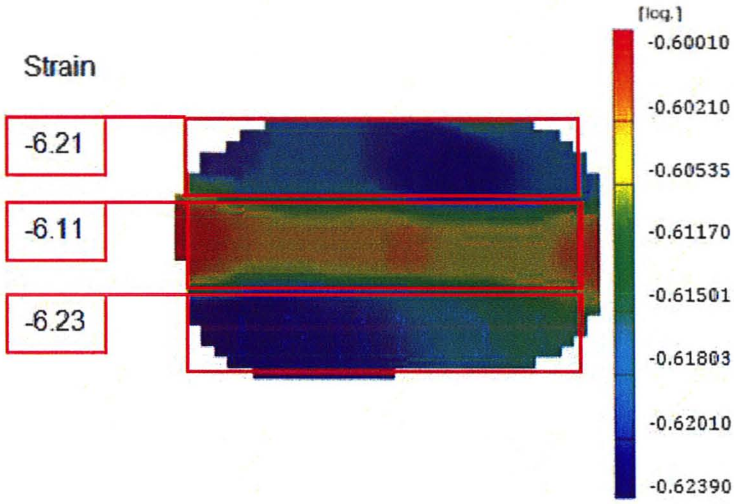

Figure 4-32. The average global strains at the top, middle, and bottom slice (using SL5506 powder mixture).

Using DIC the global true strain in each slice and corresponding density for each slice is obtained as follows:

top slice: ε_1 = -0.618, middle slice: ε_2 = -0.576, bottom slice: ε_3 = -0.621

$$\rho_{top} = exp(-\varepsilon_{h\text{-}top}) * \rho_o = exp(0.618) * 3.35 = 6.21\ g/cm^3 \quad (4\text{-}7)$$

$$\rho_{middle} = exp(-\varepsilon_{h\text{-}middle}) * \rho_o = exp(0.601) * 3.35 = 6.11\ g/cm^3 \quad (4\text{-}8)$$

$$\rho_{bottom} = exp(-\varepsilon_{h\text{-}bottom}) * \rho_o = exp(0.621) * 3.35 = 6.23\ g/cm^3 \quad (4\text{-}9)$$

After EDM cutting, the weight and volume was measured to obtain density of each of the 3 slices. Thus, by comparison with the ARAMIS based density values, a density error value was obtained for each slice as shown in Table 4-3.

Table 4-3. Predicted density and error for (test#25).

Part	Actual density	Predicted density (ARAMIS)	Error
Slice	g/cm^3	g/cm^3	%
Top	6.4	6.21	3.0%
Middle	6.12	6.11	0.2%
Bottom	6.32	6.23	1.4%

The major error in this calculation is caused by the assumption of the uniform apparent density before compaction as discussed in chapter 6.

4.4.2 Using micro-hardness to predict green density

The Vickers hardness measurement results of 22 P/M samples, in compaction load range from 5000 lbs to 17000 lbs, are shown in Appendix III. The compaction load of each sample, the six Vickers hardness values of each sample, as well as the average Vickers hardness value are also presented in a table in Appendix III. The samples with higher green density exhibited a higher Vickers hardness value as shown in Figure 4-33. The data was fitted using linear regression to obtain the following correlation:

$$HV = 53.945\,\rho - 300.14 \qquad (4\text{-}10)$$

where ρ is in g/cm^3. A R^2 value of 0.96 indicates that this trend line is a good fit to the data.

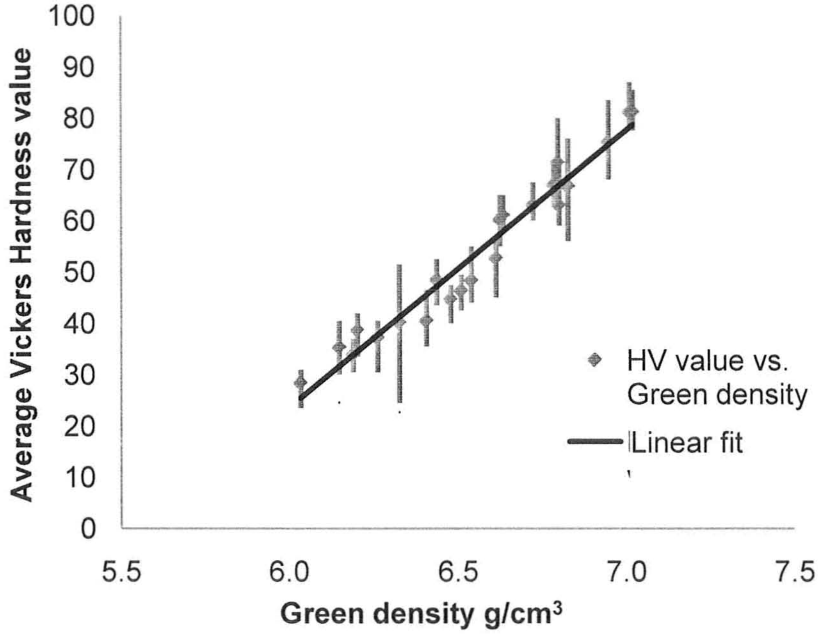

Figure 4-33. A plot of average Vickers hardness values versus green density for P/M samples (using SL5506 powder mixture) (see Appendix III).

A correlation between Vickers hardness number and green density provides a useful method to evaluate the green density of P/M parts. The top and bottom portion of the P/M double action compacted samples have higher green density than the middle portion of a compact. To obtain the local density for a larger P/M sample of height, width and length of 26.67 mm (1.05 in), 8.13 mm (0.32 in) and 14.73 mm (0.58 in) respectively, equation 4-10 was utilized in its inverted form as follows:

$$\rho = \frac{HV + 300.14}{53.945} \tag{4-11}$$

After taking Vickers hardness measurements, this P/M sample (test #26) was also cut using EDM into 5 sections as shown in Figure 4-34. The density of each piece was obtained from weight and volume measurements. The predicted densities from hardness data using equation 4-8 and measured densities for each section are compared in Figure 4-35.

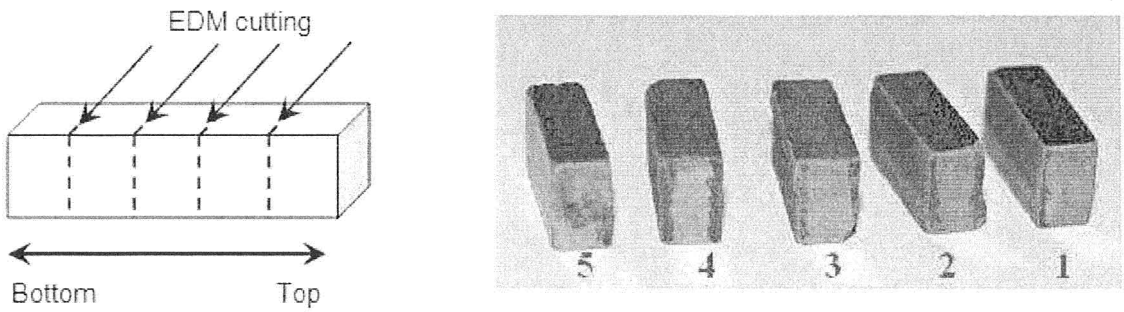

Figure 4-34. A P/M sample cutted into 5 sections (test #26, using SL5506 powder mixture).

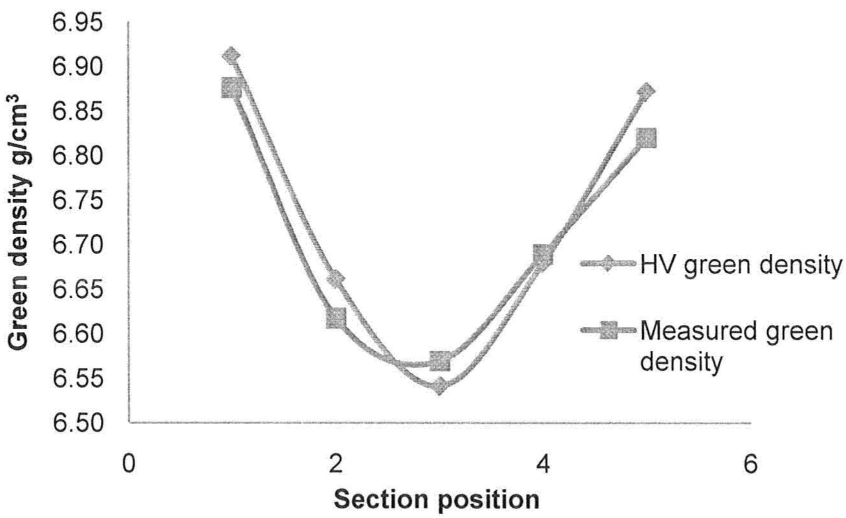

Figure 4-35. A comparison of predicted and measured green density (test #26, using SL5506 powder mixture).

A maximum density difference of 0.05 g/cm^3 between predicted and measured value is noted. This scatter in the results may be caused by sample preparation factors and by inherent variability in the hardness measurements. Thus, to obtain the local density distribution in any compact made from metal powder mixture, Vickers hardness measurement could be taken and translated into density measurements using the established calibration line. A set of 6 Vickers hardness measurements with distance, *d*, from 2.54 mm (0.1 in) to 5.08mm (0.2) from adjacent points is suggested for local density measurements.

4.4.3 Using surface roughness to predict green density

4.4.3.1 Relationship between surface roughness value and compaction load

The surface roughness measurement results of 20 P/M samples, in compaction load range from 5000 lbs to 15000 lbs, are shown in Appendix IV. The compaction load of each sample, the three measurements of R_a and R_z values of each sample, and the average R_a and R_z value of each sample are presented in a table in Appendix IV.

The sample with higher compaction load exhibited lower R_a and R_z values suggesting a better surface finish in the compact with an increase in the compaction load. Since the porosity is eliminated by an increase in the compaction load, a higher compaction load results in a lower porosity on the surface, i.e., more pores on the surface are closed as the compaction load is increased leading to a better surface finish. The plots of average surface roughness parameters R_a and R_z as a function of compaction load are shown in Figure 4-36 and Figure 4-37 respectively.

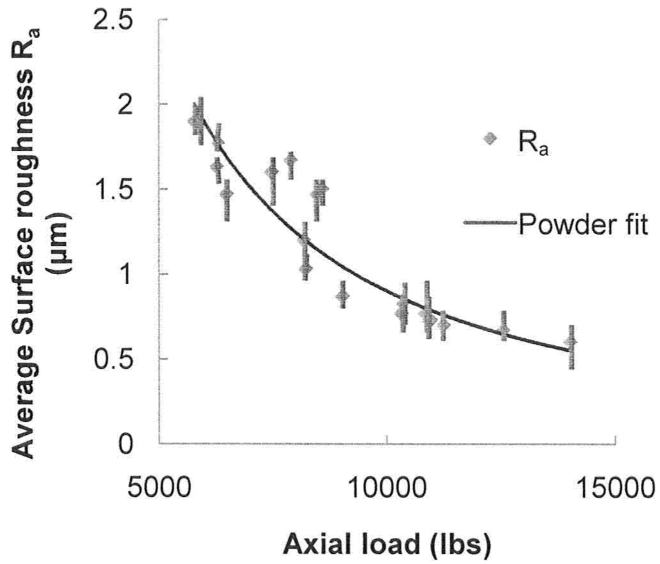

Figure 4-36. A plot of average surface roughness (R_a) versus compaction load for green P/M samples (using SL5506 powder mixture).

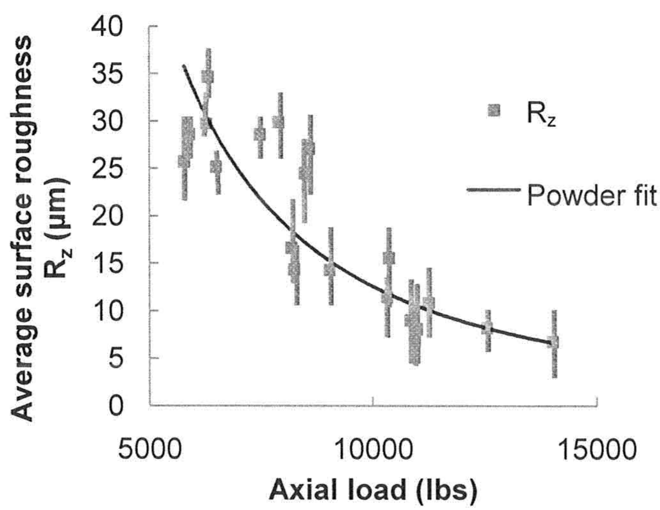

Figure 4-37. A plot of surface roughness (R_z) versus compaction load for green P/M samples (using SL5506 powder mixture).

In these figures, a non-linear regression line has been added to the experimental data. In Figure 4-36, all the data points are quite close to this trend line. However, in Figure 4-37, the data points are somewhat scattered. Therefore, it appears that the surface roughness R_a value of P/M samples has a more reliable relationship with the compaction load compared to R_z value.

4.4.3.2 Relationship between surface roughness value and green density

The green density of a P/M sample is largely influenced by the compaction load. The higher the compaction load, the higher is the green density generated and more pores are closed in the green P/M samples. Since fewer pores exist in the higher compacting load P/M samples, a better surface finish is expected. In order to obtain a relationship between the surface roughness and the green density, a plot of the average R_a of each P/M sample against its green density is shown in Figure 4-38. The following non-linear regression line is obtained from the data:

$$\rho = (R_a/10^8)^{-0.119} \tag{4-12}$$

where ρ is in g/cm^3. A R^2 value of about 0.93 is obtained for this fitted data.

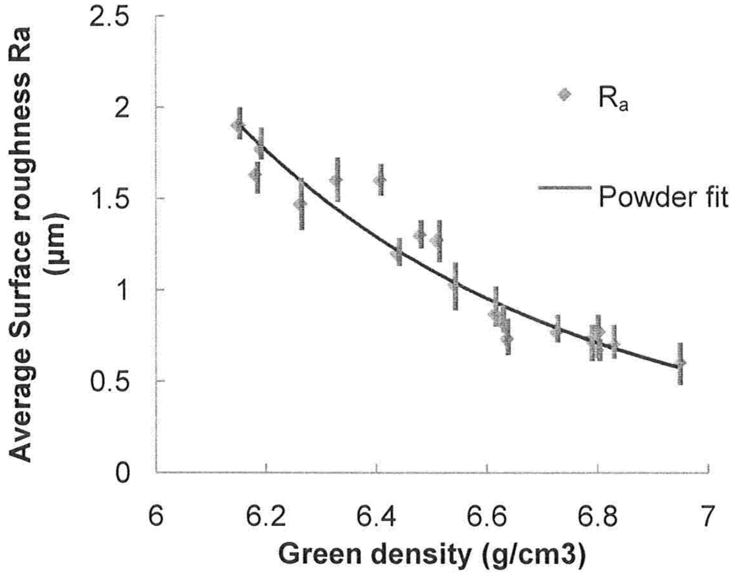

Figure 4-38. A relationship between surface roughness R_a and green density for P/M samples (using SL5506 powder mixture).

Chapter 5

FE Simulation of Metal Powder Compaction

5.1 Overview

To determine the density distribution within a component through experiments is costly as well as time consuming. In recent years, numerical simulation of the compaction process has become increasingly important, offering possibilities of faster and cheaper die design and component development. However, critical to the success of such simulations are proper calibrations of the material models and the capability to capture the influence from three-dimensional features of the component [Cedergren, 2002].

A finite element (FE) simulation of compaction experiments was carried out by employing a modified density dependent Drucker-Prager material model. The density distributions from FE simulations are compared with those obtained from the experiments. The goal is to demonstrate the usefulness of the FE simulation for obtaining average as well as local density values in the compact.

5.2 FE Model Development in ABAQUS CAE

5.2.1 CAE model

The model geometry was built by using ABAQUS CAE software and consisted of a die, two punches and a powder compact. The model set-up was identical to that in the experiments. The powder compact, punches and the die were constructed independently, and then assembled together with the powder compact into the die cavity between two punches, as shown as in Figure 5-1. This closed die compaction process is a plane strain process, since the punches and die are rigid and the compact does not undergo any dimensional changes in the two transverse directions.

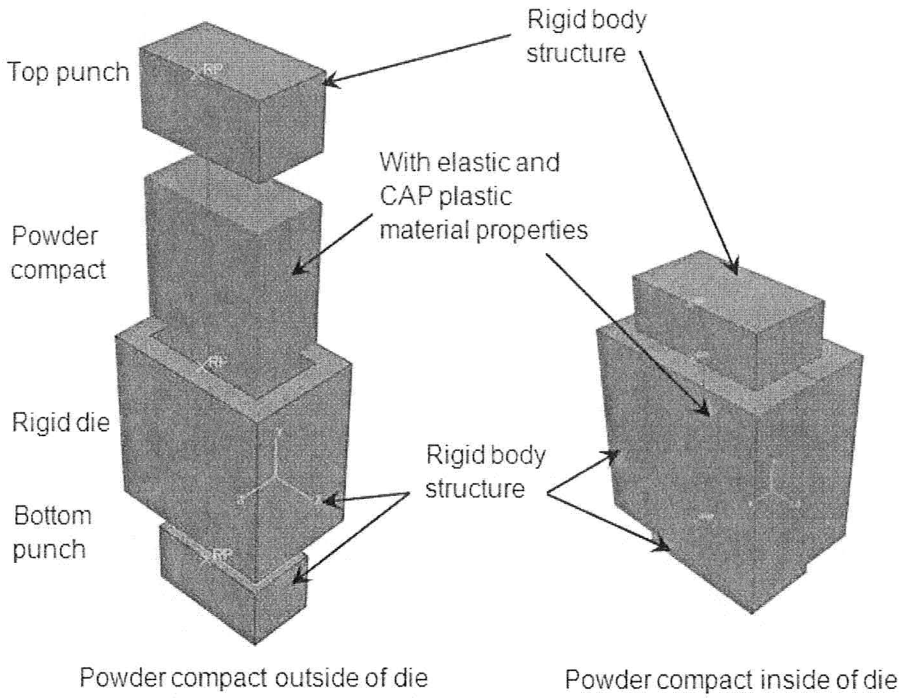

Figure 5-1. CAE geometry for the FE based powder compaction model.

The powder compact is represented by elastic and Cap plastic material properties, described in following section. Representation of punches and die as rigid bodies simplifies the analysis and reduces the computation time significantly. A reference node for each of the top punch, bottom punch and rigid die is also used, where boundary conditions specifying motion and constraints are applied.

5.2.2 Material model

5.2.2.1 Elastic parameters

In the material model for the powder compact, the elastic properties of Young's modulus *E* and Poisson's ratio ν are required. According to Wu et al., for a closed die compaction test, ν can be obtained as a function of the axial stress (compaction pressure), σ_z, and relative density of compact, ρ, from the axial stress and horizontal stress (die wall pressure) unloading curve, as shown in Figure 5-2 (a). *E* can be obtained as a function of the axial stress, σ_z, and relative density of compact, ρ, from the axial stress and axial strain unloading curve, as shown in Figure 5-2 (b) [Wu et al., 2003; Han et al., 2008].

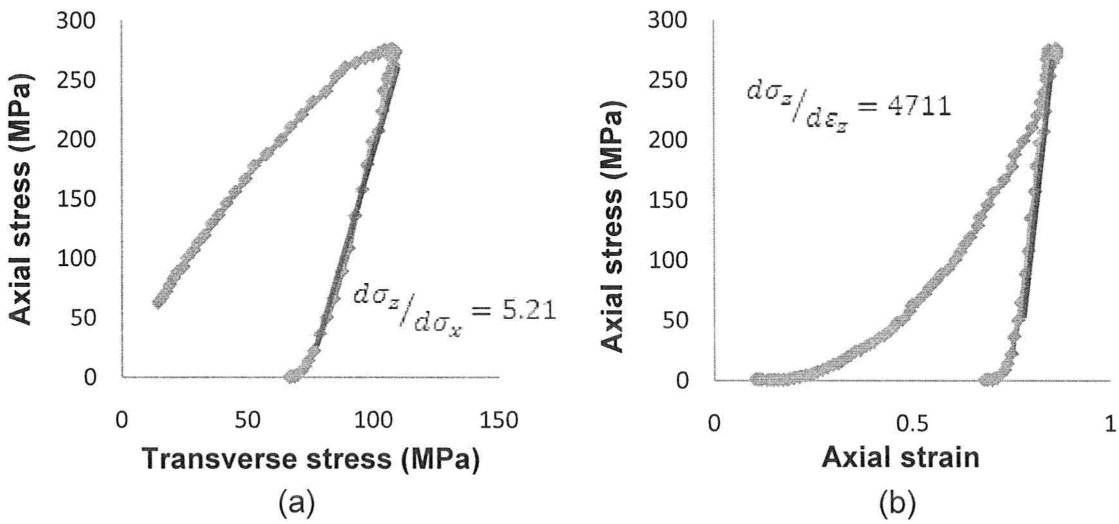

Figure 5-2. The relationships of axial stress with (a) transverse stress, and (b) axial strain during unloading.

In order to calculate Poisson's ratio for a closed die compaction test the bulk modulus can be written as

$$K = \sigma_x/\sigma_z = \sigma_y/\sigma_z \tag{5-1}$$

and the Poisson's ratio can be written as

$$\nu = K/(1 + K) \tag{5-2}$$

In the case of the compaction result in Figure 5-2 (a), the linear relation of axial stress and transverse stress can be expressed as ${d\sigma_z}/{d\sigma_x} = 5.21$ or $K = 0.1919$, so the Poisson's ratio for this compact is $\nu = K/(1 + K)$ = 0.16. For a closed die compaction test the Young's modulus can be written as,

$$E = M(1 - 2\nu K) \tag{5-3}$$

where as *M* is the linear relation between axial stress and axial stain during unloading as shown in Figure 5-2 (b), and

$$M = {d\sigma_z}/{d\varepsilon_z} = 4711\ MPa \tag{5-4}$$

Considering $\nu = 0.16$ and $K = 0.1919$, the Young's modulus E is obtained as

$$E = M(1 - 2\nu K) = 4420 \text{ MPa}.$$

By adopting the same approach, the Poisson's ratio and Young's modulus for other 9 compaction tests with incremental density are also calculated, as shown as in Table 5-1.

Table 5-1. The calculated Poisson's ratios and Young's modulus of compacts with incremental green density (using SL5506 powder mixture).

Density (g/cm^3)	$d\sigma_z/d\sigma_r$	$d\sigma_z/d\varepsilon_r$	Poisson's ratio	Young's modulus (MPa)
6.26	7.158	4108	0.12	3967
6.32	6.393	4278	0.14	4097
6.4	5.532	4510	0.15	4260
6.5	5.213	4711	0.16	4420
6.59	4.719	5064	0.17	4689
6.7	4.327	5365	0.19	4899
6.75	4.192	5590	0.19	5076
6.82	3.78	5982	0.21	5320
6.95	3.556	6589	0.22	5776

The trend curve of Poisson's ratio and Young's modulus values as a function of density are also shown in Figure 5-3. Thus, using equations 5-1 5-2, we can obtain the Poisson's ratio, ν, as a function of the axial stress, σ_z, and the density of compact, ρ, from the axial stress/transverse stress unloading curve in Figure 5-2 (a). Consequently, using equations 5-3, 5-4, and the Poisson's ratio, we can obtain the Young's modulus as a function of the axial stress, σ_z, and the density of compact, ρ, from the axial stress/axial strain unloading curve.

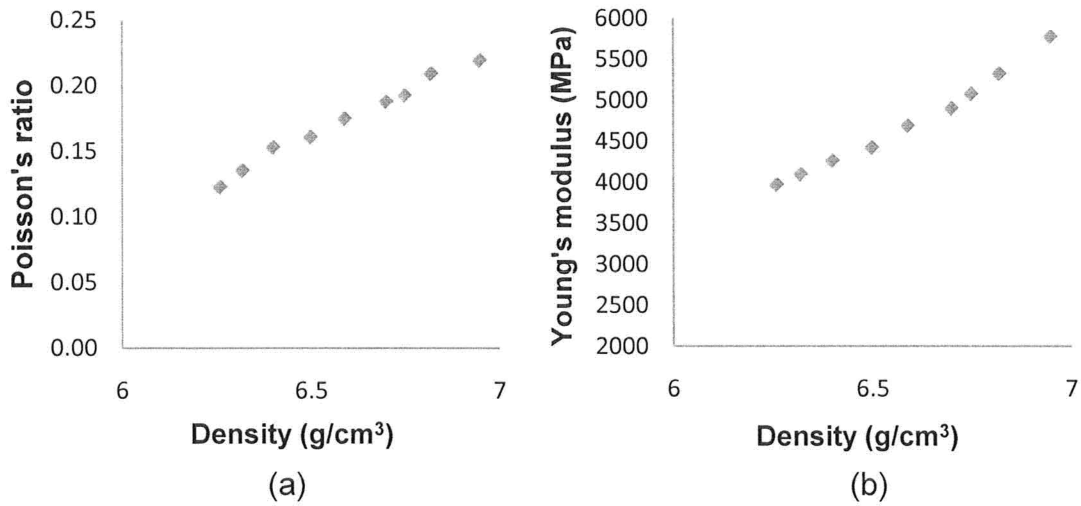

Figure 5-3. (a)Poisson's ratio and (b) Young's modulus as function of the density (using SL5506 powder mixture).

5.2.2.2 A modified density dependent Drucker-Prager Cap plasticity model

A modified density dependent Drucker-Prager Cap plasticity model associated with plastic hardening was adopted in the FE simulation of compaction. The model is assumed to be isotropic and its yield surface includes three segments: a shear failure surface, providing dominantly shearing flow, a "cap," providing an inelastic hardening mechanism to represent plastic compaction, and a transition region between these segments, introduced to provide a smooth surface purely for facilitating the numerical simulations. A typical Drucker-Prager Cap model is shown in Figure 5-4.

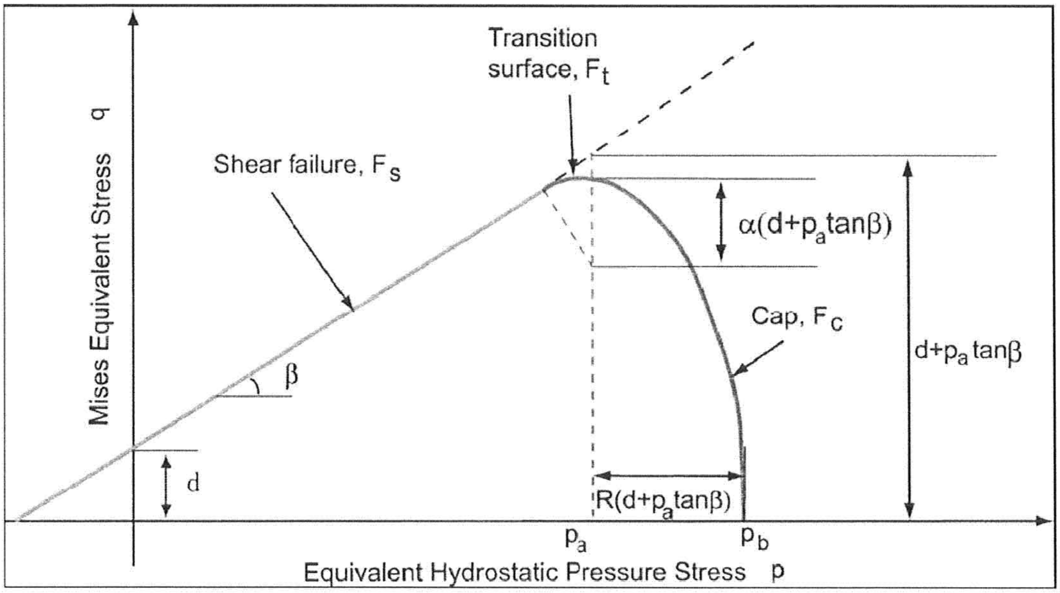

Figure 5-4. Drucker-Prager Cap model: yield surface in the p-q plane [Han, 2008].

As shown in Figure 5-4, six parameters are required to define the yield surface of the modified DPC model:

d : material cohesion

β : material angle of friction

α : transition surface parameter

P_b : Initial Cap yield at $\varepsilon_v^{in} = 0$

R : Cap eccentricity parameter

P_a : Evolution parameter

To uniquely define each of the evolving yield surfaces as a function of relative density, the above six parameters are also required as functions of relative density. In order to determine these six parameters at different densities, a set of uniaxial compression and diametrical compression tests are required (see Figure 5-5). Most of these tests were done in Stackpole Ltd. (now part of Gates Canada Ltd.).

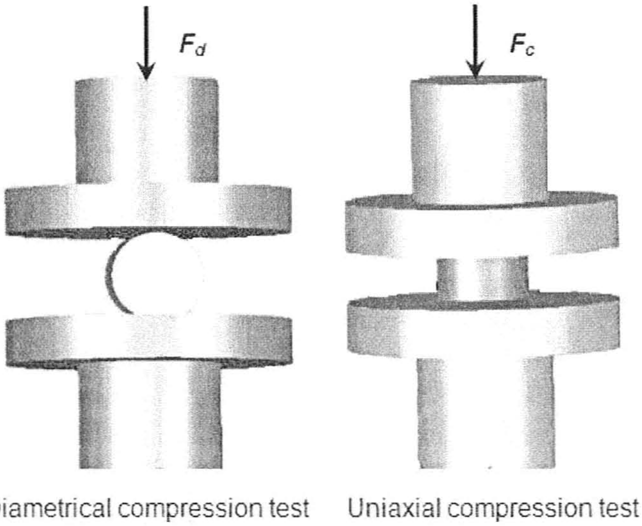

Figure 5-5. Illustration of diametrical compression test and unaxial compression test.

The load of F_d and F_c during the above tests were recorded until the failure and stress developed along the transverse direction. According to Wu et al. [Wu et al., 2003], the stress state during diametric test is given by:

$$\sigma_d = 2F_d / (\pi D t) \tag{5-5}$$

where D is the diameter of the compact sample and t is the thickness of it. The stress state in unaixal compression test is given by:

$$\sigma_c = 4F_c / (\pi D^2) \tag{5-6}$$

where D is also the diameter of the compaction samples. The cohesion, *d* and the slope representing the internal angle of friction, *β*, can be determined as follows:

$$d = \frac{\sigma_c \sigma_d (\sqrt{13} - 2)}{\sigma_c - 2\sigma_d}$$

(5-7)

$$\beta = arctan[\frac{3(\sigma_c - d)}{\sigma_c}]$$

(5-8)

To define the cap yield surface, α is set to be 0.01. According to Wu et al., P_a and R can be determined by analysing the stress state of the loading points on the cap surface during a closed die compaction process (see Figure 5-6). The cap eccentricity parameter, R, is given as:

$$R = \sqrt{\frac{2\left(1 + \alpha - \frac{\alpha}{cos\beta}\right)^2}{3q_A}(p_A - q_A)}$$

(5-9)

Consequently, the evolution parameter, P_a, can be obtained as:

$$p_a = -\frac{[3q_A + 4d\ tan\beta\left(1 + \alpha - \frac{\alpha}{cos\beta}\right)^2]}{4[\left(1 + \alpha - \frac{\alpha}{cos\beta}\right)tan\beta]^2} + \frac{\sqrt{9q_A^2 + 24dq_A\left(1 + \alpha - \frac{\alpha}{cos\beta}\right)^2 tan\beta + 8(3p_A q_A + 2q_A^2)[\left(1 + \alpha - \frac{\alpha}{cos\beta}\right)tan\beta]^2}}{4[\left(1 + \alpha - \frac{\alpha}{cos\beta}\right)tan\beta]^2}$$

(5-10)

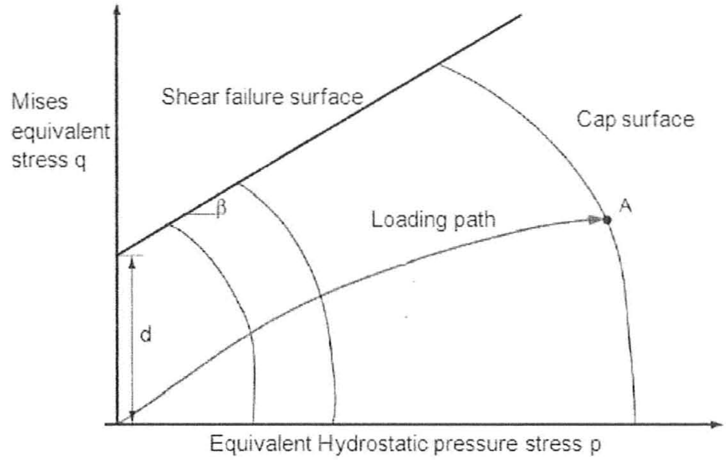

Figure 5-6. Loading path to determine DPC parameters.

The determined cap parameters *d, β, R, α with* the corresponding relative densities are shown in Table 5-2.

Table 5-2. Cap parameters *d, β, α, R* with the corresponding relative densities.

Relative density	d	β	R	α
0.5	15	40	0.8	0.01
0.6	20	50	0.81	0.01
0.7	30	60	0.85	0.01
0.8	40	70	0.89	0.01
0.9	50	72	0.89	0.01
1	60	72	0.89	0.01

The modified DPC model and the density dependent material parameters are adopted in a user subroutine file, which is originally developed by Dr. Zhang, a Research Associate in the Metal Forming Lab at McMaster. This user subroutine file is utilized within the ABAQUS FE analysis code for powder compaction simulations.

5.2.3 Boundary conditions

Two different boundary conditions were used for single action and double action compaction simulations. Both of them adopted displacement/rotation type boundary condition. At the initial state, for single action compaction simulation, bottom punch and die were restricted from any movements and deformations while the top punch was free of movement in the axial direction only. For double action compaction simulation, the die was also restricted from any movements and deformations, but both of the top and bottom punches were free of movements in axial direction. These two boundary conditions are illustrated in Figure 5-7. In both cases, the compact body was in contact with the inside surface of the die wall. A friction contact interaction was defined with a Coulomb friction coefficient value in the range from 0.025 to 0.2.

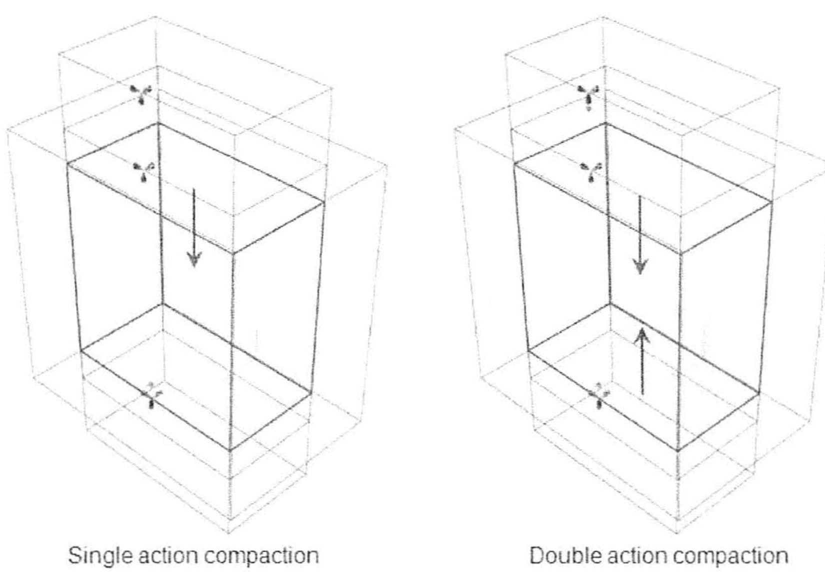

Figure 5-7. The boundary conditions for single and double action compaction processes.

5.2.4 Meshing

A uniform mapped mesh was created for the powder compact, as shown in Figure 5-8. A Hex (8-node) element type was chosen. This element type, C3D8R (reduced integration), was used in the 3D models. In general, using more elements provided a relatively more accurate result. However, a finer mesh required much more computational time. The distortion of the mesh had a strong influence on the accuracy of the results. Also, the distorted elements caused the simulation to stop. A total of 500 elements were created which resulted in good accuracy and without massive computational effort. A rigid discrete element (R3D4) was assigned to the two punches and die because ABAQUS requires meshing of the rigid body in 3D modelling.

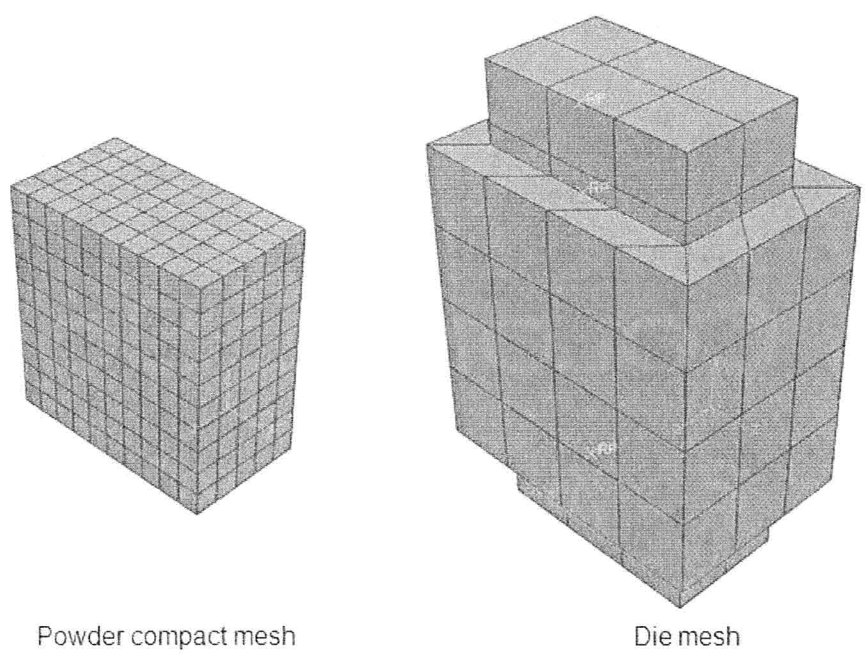

Figure 5-8. Meshed instances for CAE compaction modelling.

5.3 FE Simulation Results

5.3.1 Green density versus compaction pressure

Figure 5-9 shows a comparison of double action compaction experimental data and calculated FE simulation results for variation of green density with compaction pressure for SL5506 powder mixture (also see Figure 4-27). The experimental data points were obtained from double action compaction of SL5506 powder mixture. The solid curve is obtained from FE simulation results. In general, the model captures the experimental trend quite accurately. Further comparison between FE simulation results and experimental results will be provided in the next chapter.

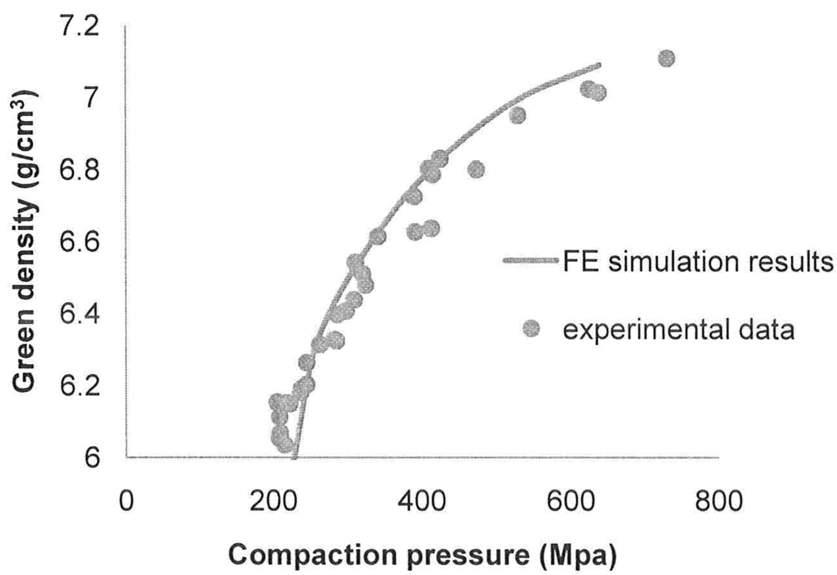

Figure 5-9. Comparison between experimental data and FE simulation (with friction coefficient of 0.03) results for the variation of green density of double action compaction.

5.3.2 Deformed meshes in single and double compaction

The meshes for the powder body before and after single action and double action compactions are shown in Figure 5-10. The initial height of the powder compact is 6.0 mm which is pressed to 3.2 mm after compaction. The unshaded wired frame region in the figure represents the powder compacts before compaction.

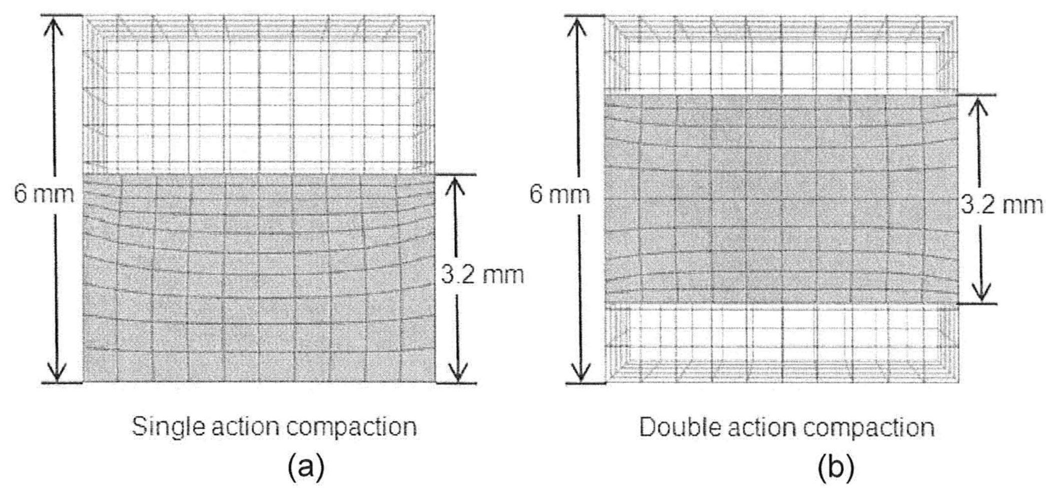

Figure 5-10. Deformations of powder compacts instance during (a) single action and (b) double action compaction simulation with friction coefficient of 0.2.

Figure 5-10 (a), shaded region, shows that the elements at the top section of the powder compact have the largest deformation, especially at the corners, and the elements at the bottom section have the smallest deformation in a FE single action compaction simulation. For double action compaction, on the other hand, the elements at the top and bottom sections of the powder compact have larger deformation than those in the middle section (see Figure 5-10 (b)). This is consistent with the experimental data presented earlier in Chapter 4.

5.3.3 Stress and strain results

The axial strain distribution map with continuous color gradient for single action compaction simulation is shown in Figure 5-11. The blue color, representing the highest axial strain value in the powder compact, is at the top section and especially at the top corners. The red color, representing the lowest axial value in the powder compact, is at the bottom section. This clearly indicates that the top portion of the powder compact has more powder particles compressed together than at the bottom.

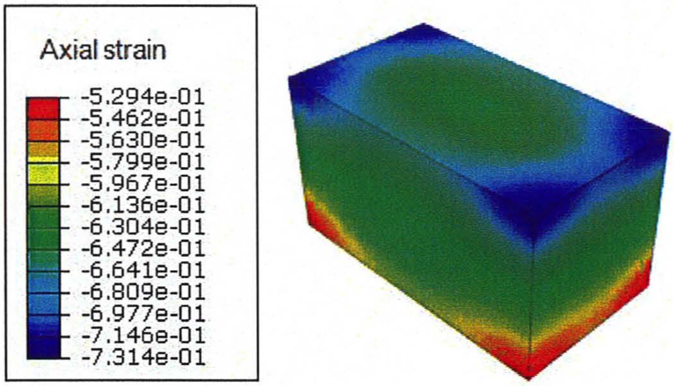

Figure 5-11. Axial strain distribution for a FE single action compaction simulation with friction coefficient of 0.03.

Figure 5-12 shows that the axial stress has a similar distribution as the axial strain in the powder compact, the top section generated higher axial stress than the bottom section during the single action compaction simulation. In other words, the higher local axial stress generates a higher local axial strain in a powder compact.

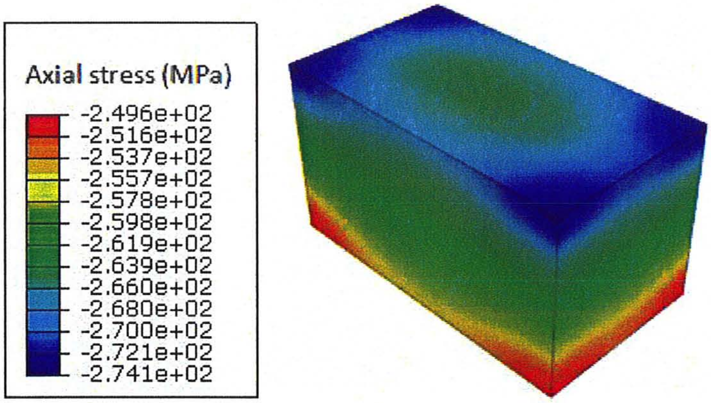

Figure 5-12. Axial stress (compaction pressure) distribution in the powder compact for a FE single action compaction simulation with friction coefficient of 0.03.

The axial strain distribution map for double action compaction simulation is shown in Figure 5-13. For double action compaction, the highest axial strain is at the top and bottom sections and especially at the corners of the powder compact, while the lowest axial strain is at the middle section of the powder compaction. This indicates that more material was compressed together at the top and bottom regions in the powder compact, whereas the middle portion remained less compact and with a lower density.

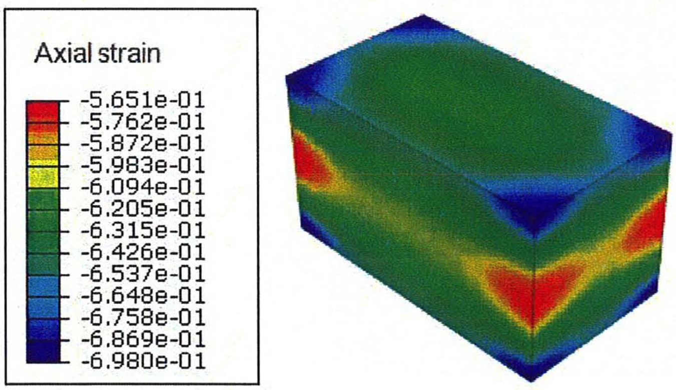

Figure 5-13. Axial strain distribution for a FE double action compaction simulation with friction coefficient of 0.03.

Figure 5-14 shows, as earlier, that the axial stress has a similar distribution as the axial strain in the powder compact, the top and bottom sections generated higher axial stress than the middle section during a FE double action compaction simulation.

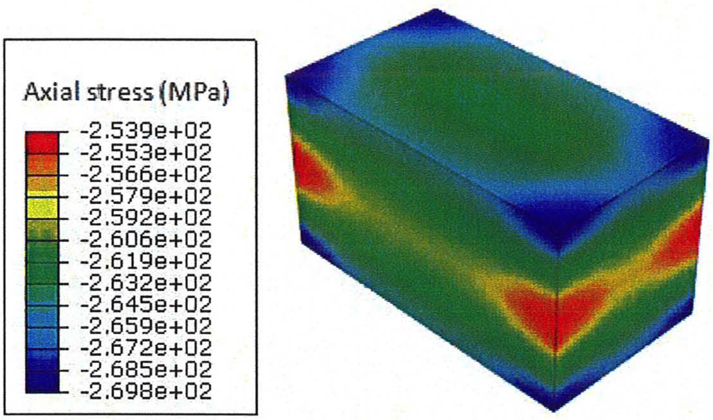

Figure 5-14. Axial stress (compaction pressure) distribution in the powder compact for a FE double action compaction simulation with friction coefficient of 0.03.

It is to be noted that strains are higher at the corners in all of the simulations. This was not captured by DIC based experiments. This is discussed further in the next chapter.

5.3.4 Density distribution

The approach for the calculation of green density by using axial strain was introduced in the previous chapter. Here, this approach is also used to calculate the green density distribution in the powder compact from FE compaction simulations. There are 8 density gradient lines which represent 8 different green densities, drawn on the powder compact in Figure 5-15 for single action compaction and in Figure 5-16 for double action compaction.

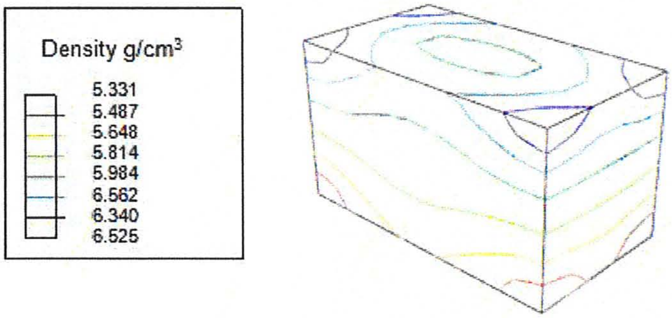

Figure 5-15. FE simulation results for green density contour plots for a single action compaction (with friction coefficient of 0.03).

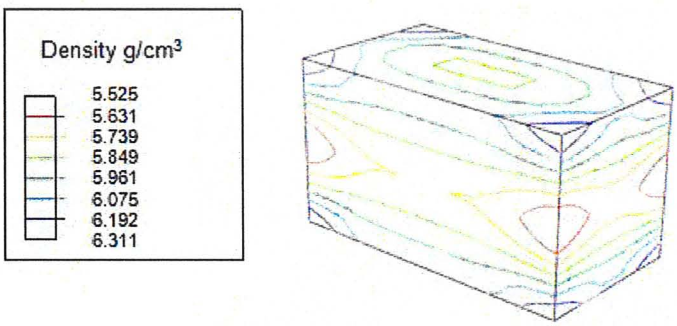

Figure 5-16. FE simulation results for green density contour plots for a double action compaction (with friction coefficient of 0.03).

The single action compaction has the same compression ratio (i.e., the ratio of the volume of the loose powder to the volume of the compact made from it), which is 1.88, as in the case of double action compaction. The powder compact has a larger green density gradient from the single action compaction simulation than from the double action compaction simulation. In die pressed powder compacts, the density gradients result from the pressure gradients. The pressure gradient (axial stress) has a large range for a since action compaction than for a double action compaction due to die wall friction. This is further discussed in the next chapter.

Chapter 6

Discussion

6.1 Generation of Shear Bridges and Cracks

Shear bridges and cracks result from non-uniform density distribution during suction filling and powder transfer. As described in Chapter 4, in suction filling, powder is delivered to the die from the shoe which stays on top of the die cavity while the bottom punch is moved downward to fill the powder in the die. This process results in a loose packing of powder in the die. In the experiments, after filling, the powder is transferred within the die to the compaction position. The powder particles rearrange in the die during the powder transfer process to form bridges and cracks.

During the transfer process, such as observed in Figure 4-5, particles move downward. However, due to the die-wall friction the powder particles move at a slower speed close to the die wall and pack tightly together to form shear bridges. Figure 4-5 (a) and (b) shows the intermediate stages during the transfer test, with particle rearrangement under shear bridge close to the bottom of the die cavity. The displacement above the shear bridge is smaller than that below the bridge as the speed of the powder above the shear bridges is slower than the transfer speed. Figure 4-5 (c) shows that a separation begins to appear along the die walls and grows rapidly with an increase in displacement distance of the powder below the shear bridge. As a result, the portion of the powder body at the bottom die cavity is separated from the rest of the transfer volume of the powder body to form a crack.

During the transfer process, the apparent volume occupied by the powder in the die is constant so that the powder is still loose and the die wall friction as the powder slides over the steel die wall results in shear deformation in the powder body. Consequently, due to the mobility of the particles during transfer and the die wall friction, local changes in the packing density are likely to occur. It also can be said that, for the same die and process conditions but with different die-wall friction, a more significant density change is developed with higher friction. The shear direction is opposite of the gravity direction. The particle rearrangement mode of the powder during transfer (see Figure 6-1) can be characterized by three regions: (1) tightly packed region close to the upper punch, (2) loosely packed region close to the bottom punch usually containing cracks, and (3) region close to the die walls in which powder moves at a relatively slower speed in the transfer direction.

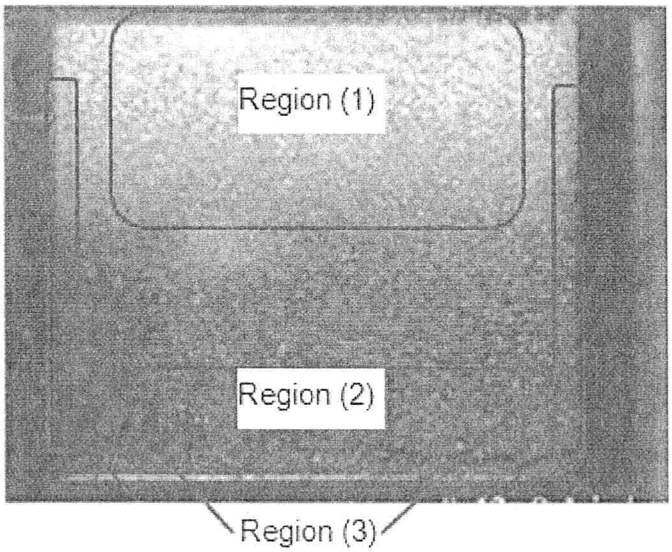

Figure 6-1. Particle re-arrangement during powder transfer process with 2.54 mm/s (0.1in/s) speed (using SL5506 powder mixture).

The above trend in the local density change during powder transfer is consistent with the experimental observations of Wu et al. [Wu et al. 2003], where it was shown that generation of shear zone during powder transfer, result in a change in local density distribution. Also, the density distribution prior to compaction is affected by the inter-particle friction. Thus, there is a larger increase in density gradient for powders with higher interparticle friction as the particles rearrange during filling and transfer processes.

Experiments using different transfer speeds are also carried out to obtain an understanding the effect of speed on the powder distribution during powder transfer. As the transfer speed is increased arc-shaped shear bridges are developed. According to Wu et al., powder material along the shear bridges induces inter-granular slip and rotation, which leads to dilating width of the arc bridges with a lower density. In Chapter 4, Figure 4-6 demonstrates that the transfer speed affects the mechanism of shear bridge propagation and powder separation during the transfer process. Table 6-1 shows the times of appearance of shear bridge and crack during 5 powder transfer tests at each of the following transfer speed 5.08 mm/s (0.2 in/s), 10.16 mm/s (0.4 in/s), 12.7 mm/s (0.5 in/s), 20.32 mm/s (0.8 in/s), 25.4 mm/s (1.0 in/s) and 50.8.4 mm/s (2.0 in/s). In general, the shear bridges were observed at most of the transfer tests at all different speeds. However, the cracks were observed frequently at transfer speeds below 25.4 mm/s (1.0 in/s), but when the transfer speed reached to 50.8.4 mm/s (2.0 in/s) the chances of appearance of cracks were reduced. It is likely that at higher transfer speeds, the frictional force is smaller between the powder particles as well as between the particles and the die wall. A reduced frictional force results in smaller displacement (or relative movement) between particles which reduces the propensity towards initiation of cracks.

Table 6-1. Occurrences of shear bridge and crack at the different transfer speeds (using SL5506 powder mixture).

Transfer speed	5.08 mm/s (0.2 in/s)	10.2 mm/s (0.4 in/s)	12.7 mm/s (0.5 in/s)	20.3 mm/s (0.8 in/s)	25.4 mm/s (1.0 in/s)	50.8 mm/s (2.0 in/s)
Total number of test	5	5	5	5	5	5
Shear bridge appeared	5	5	4	5	4	4
Crack appeared	4	4	5	5	3	2

6.2 Single Action and Double Action Compaction Characteristics

In Figure 6-2, the strain maps from single and double action compaction experiments are compared. Both strain distribution maps represent the last re-meshing step for strain calculation. The strain map can be divided into 3 sections for the single action compaction: (1) the highest axial strain section at the top of the compact, (2) the medium axial strain section in the middle of the compact, and (3) the lowest axial strain section at the bottom of the compact. The strain distribution is different for the double action compaction which has: (1) higher axial strain in top and bottom sections of the compact, (2) lower axial strain in the middle section of the compact. This strain distribution is caused by the friction between the powder compact and the die wall during compaction. Friction contributes to a decreased pressure with the axial depth of the compact which results in a corresponding strain distribution in the compact. The friction acts opposite to the direction of punch movement.

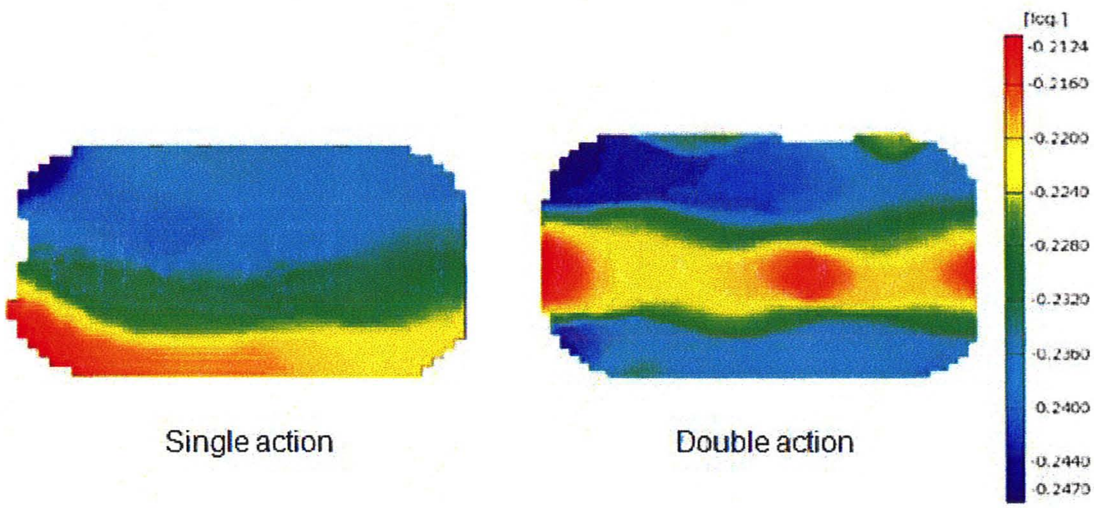

Figure 6-2. Comparison of strain maps for single and double action compactions (using SL5506 powder mixture).

The experimental data for these two compacts are also summarized in Table 6-2. The single action compaction sample has a lower overall strain and green density compared to the double action compaction sample. This verifies the earlier assumption that higher absolute strain value means more powder particles are packed together resulting in a higher density.

Table 6-2. A comparison of compaction characteristics of single and double compaction samples.

Compact	Material	Density (g/cm^3)	Max compression pressure (MPa)	Axial strain
Single	SL5506	5.99	197	0.581
Double	SL5506	6.27	251	0.613

Figure 6-3 shows the compaction pressure versus axial strain curves for the above single and double action compactions. At the starting stage of the compactions, the pressure strain curves are almost coincident. As the pressure is increased to a certain value, the single action compaction results in a lower strain (and density) value. In other words, the single action compaction needs to have higher compaction pressure to compress the powder further than the double action compaction. Therefore, the double action compaction is a more efficient method for powder compaction.

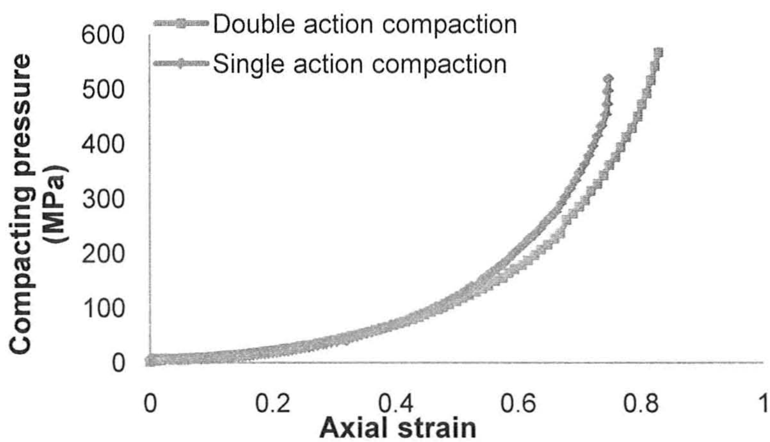

Figure 6-3. Compression pressure versus axial strain for single and double compaction (using SL5506 powder mixture).

6.3 Achieving Higher Green Density in Compaction

As described earlier in sub-sections 4.4.4 and 4.4.5, the use of the powder with lubricant can reduce the friction between the powder compact and the die wall, and also protect the die surface from damage during ejection. Therefore, in order to make the compaction more efficient, the addition of lubricant in the powder mixture is necessary. According to the previous section, the double action compaction generates a powder compact with more uniformed density distribution than the single action compaction. So, in order to make the compaction more efficient the double action compaction should be used.

Figure 6-4 shows a comparison of density versus pressure data for single action compaction without lubricant and the double action compaction with lubricant. The green density is slightly higher for double compaction than the single compaction for the same compaction pressure. This result indicates that by using a certain amount of lubricant and a double action compaction mechanism a higher green density can be achived in the P/M parts.

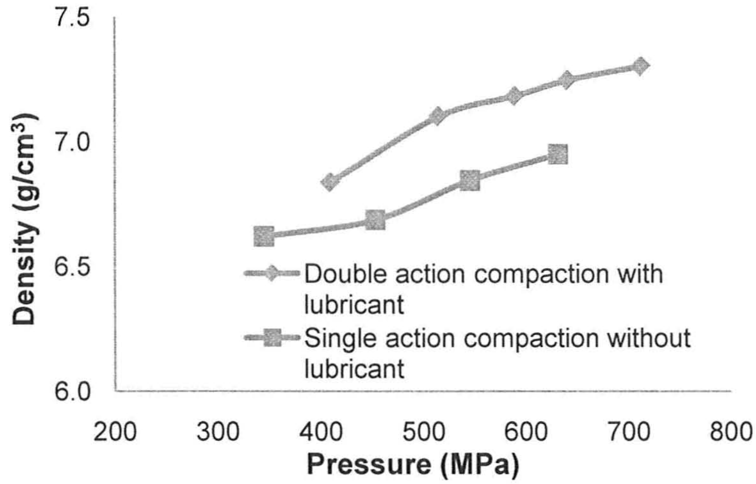

Figure 6-4. Density versus compaction pressure for single and double action compactions (AT1001 powder for single action compaction, AT1001 with 7% Kenolube for double action compaction).

6.4 Advantages and Limitations of ARAMIS Strain Analysis System for Powder Compaction

This study takes the advantage of the ARAMIS system based on digital image correlation (DIC) analysis to successfully obtain strain map on one of the faces of the green compact. The calculated strain results are obtained using a re-meshing procedure, in which DIC was used to measure the local strain increments. The average and local strain development characteristics for metal powder compactions in single and double action compaction modes are generally consistent with the trend reported in the literature for average and local density measurement, as well as the direct density measurements obtained in this work. The trends are also consistent with FE simulation results.

This study also shows the limitation of this DIC analysis by using ARAMIS system, which is restricted to 2D particle movement while in real situation the third dimension movement of the metal powder occurs. ARAMIS also fails to analyze corner regions due to poor image quality which are often quite important in terms of density variation and part strength. However, the 2-D strain map, strain history and compaction pressure versus strain curve offer a useful means of validating the results of FE simulation of the metal powder compaction.

6.5 Green Density Measurements

One characteristic feature of powder-manufactured (P/M) components is the density, governing the mechanical properties of the component. Generally a high density is preferred. The density is not homogenous through the body but is dependent on friction between the powder and the die wall during the compaction phase, shape of the body, dynamic effects, and applied pressure. The density distribution measurement is, however, not trivial.

This study, for the first time, presents a method of converting strain distribution map calculated by utilizing ARAMIS strain measurement system into density distribution. However, the predicted result show some variation with the measured density. The largest error appeared in the calculation for the local density in the top section of the powder compact (see Figure 4-30), which is about 3% smaller than the measured value. This error is due to the assumption of the uniform density distribution prior to powder compaction and after powder filling and transfer. According to the previous discussion of the powder transfer process, the powder particles are tightly packed in the top section of the powder body, while the powder particles are loosely packed in the bottom section powder body. As a result, the top section of the powder body has a higher apparent density than the average apparent density of the powder body. Once this aspect of initial density variation is accounted for in the ARAMIS calculations, the result should be more accurate.

This study also presents a method of utilizing Vickers hardness measurements to obtain density distribution data for the P/M parts in sub-section 4.4.2. The relationship of Vickers hardness value and the green density of SL5506 powder mixture compact was established, and it was used to rapidly determine the green density distribution in the P/M samples. This technique has been also applied with a similar accuracy in the studies of Chtourou et al. [Chtoutou et al. 2002]. So our experiments further confirm that this method can be a good application for assessing density distribution, and hence part quality.

In addition, this study presents a new method of utilizing surface roughness value for the P/M parts to obtain density distribution data in sub-section 4.4.3. Relationships between R_a value with the green density, and R_z versus green density were established. However, since the R_a value represent the average surface finish of the powder compact while the R_z value represents the highest gradient of surface finish of the powder compact, the Ra value appears to be a better indicator for the green density.

6.6 Effect of Friction Coefficient

Process simulations by using a finite element analysis are useful in gaining an understanding of the powder flow and density distribution during P/M forming process. In this study, the numerical modeling of the powder compaction process adopted the modified density dependent Drucker-Prager Cap material model with elastic material proprieties for densification of a powder material. However, proper friction coefficient is critical to obtaining reliable density distribution data. The axial strain and stress distribution from simulation results of double action compaction for different friction coefficient of 0.25, 0.05, 0.1 and 0.2 are shown in Figures 6-5 and 6-6.

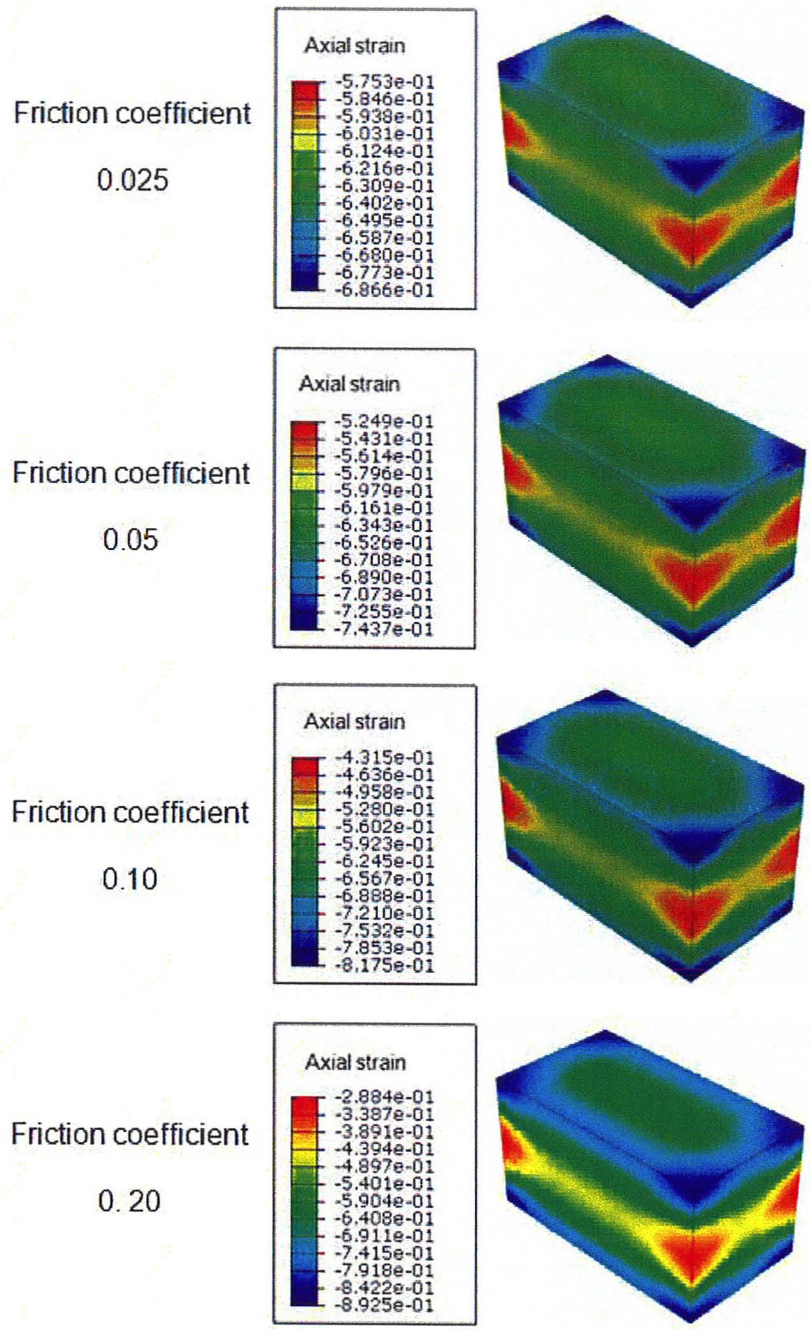

Figure 6-5. Axial strain distribution from FE simulation with friction coefficients in the range of 0.025 – 0.20.

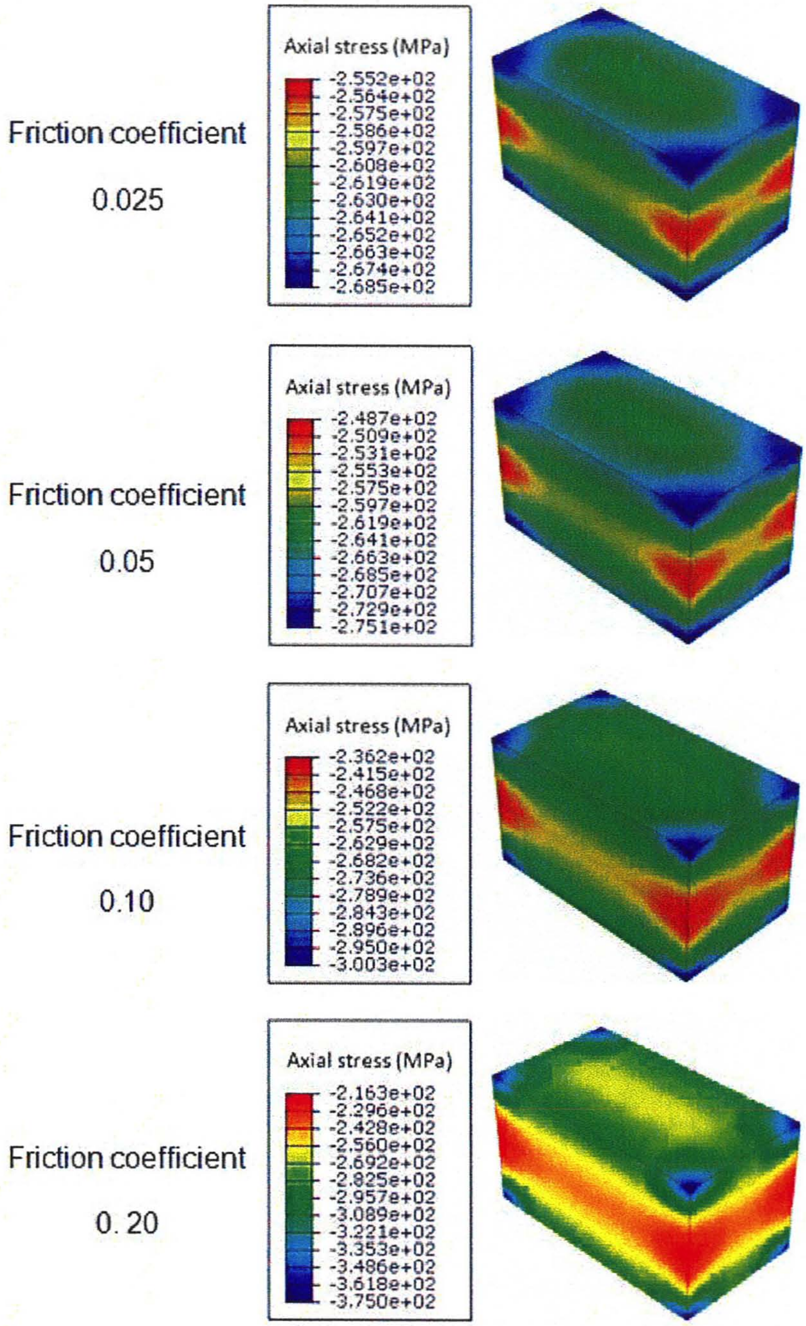

Figure 6-6. Axial stress distribution from FE simulation with friction coefficients in the range of 0.025 – 0.20.

As shown, the increase of the friction coefficient caused an increase in the local strain and stress gradients for double action compaction simulation results. The FE simulation results are summarized in Table 6-3.

Table 6-3. Axial strain and stress results for FE double action compaction simulations with different friction coefficient.

Friction coefficient	0.025	0.05	0.10	0.20
Minimum axial strain	0.5753	0.5249	0.4315	0.2884
Maximum axial strain	0.6866	0.7437	0.8175	0.8925
Strain gradient	0.1113	0.2188	0.3860	0.6041
Minimum axial stress (MPa)	255	249	236	216
Maximum axial stress (MPa)	268	275	300	375
Stress gradient (MPa)	13	26	64	159

6.7 Comparison of Experimental and Simulation Results

The displacement map generated by ARAMIS system for a double action compaction (test# 25 using SL5506 powder mixture) is compared with the FE simulation result for a compression ratio of 1.88 in Figure 6-7. In both of the displacement maps the blue color indicates downward movement of the powder while the red color refers to the upward material movement. The two displacement maps reveal very similar displacement patterns.

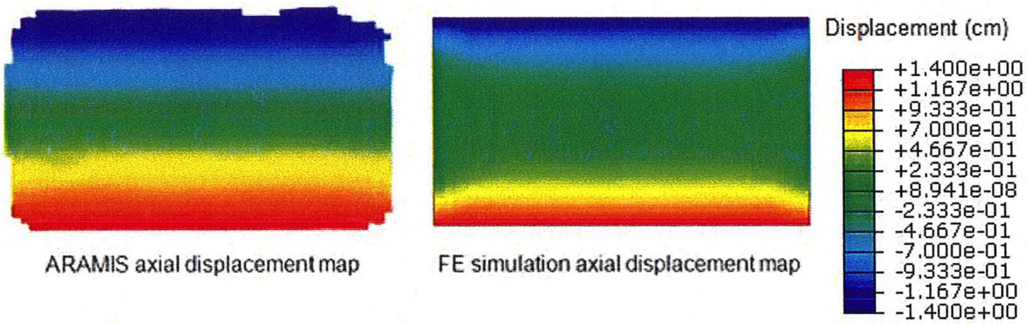

Figure 6-7. Axial displacement maps generated by ARAMIS strain measuring system for Test# 25 and by FE simulation of corresponding compaction process.

Moreover, the axial strain distribution calculated by the ARAMIS system for the same double action compaction experiment is compared with the same FE simulation result in Figure 6-8. In the strain distribution maps the blue color represents larger compressive axial strain than the yellow and red colors. The FE simulation result shows that the highest axial strains are concentrated on the corners of the top and bottom sections of the powder compact. However, the experimental data could not be calculated in these areas due to the large deformation and poor image quality. Leaving these corner regions, however, the agreement in strain distribution as measured by ARAMIS and FE simulations is satisfactory.

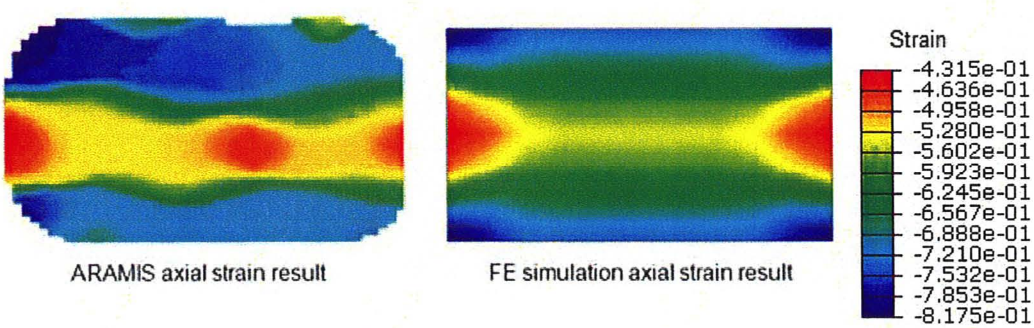

Figure 6-8. Axial strain maps generated by ARAMIS strain measuring system for Test# 25 and by FE simulation of corresponding compaction process.

Local green densities were evaluated for a double action compaction compact, which was cut into 3 sections by EDM. The green density of each section was measured to obtain the local density distribution. In order to compare with this experimental result, a simulation with a friction coefficient of 0.20 with the similar compaction ratio was carried out. The FE simulation results were separated into 3 sections and the density of each section was calculated from the average axial strain for each of the sections. A comparison of the local density for each section from the experimental result and FE simulation is shown in Figure 6-9.

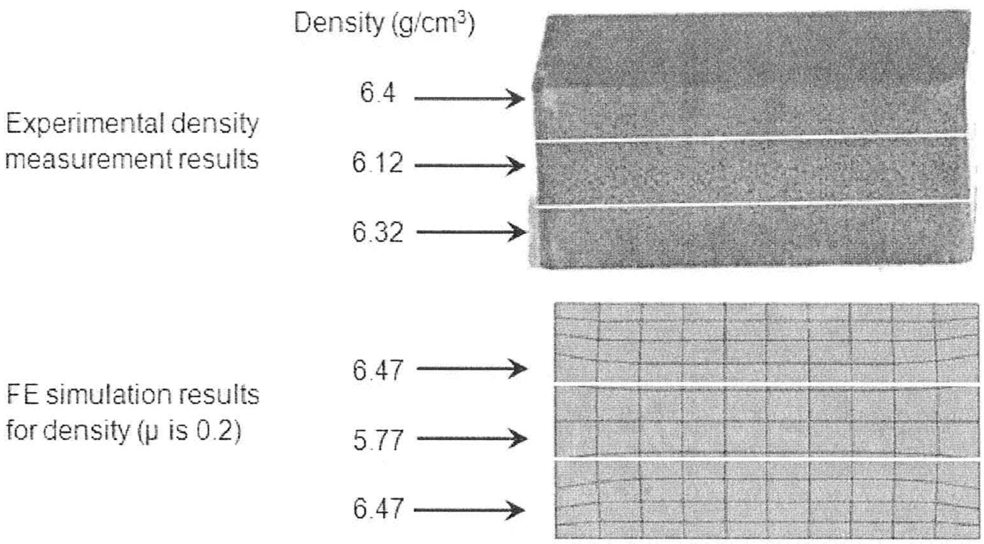

Figure 6-9. A comparison of sectional density for experimental result (test #25) with a corresponding FE simulation result with (μ is 0.2).

The density of each section of the compact is somewhat different between the experimental measurements and the FE simulation. To investigate this further, simulation data for other friction coefficients was obtained and compared with experimental data as shown in Table 6-4 below.

Table 6-4. Experimental and simulation results of densities for each section of powder compact.

	Experimental result density (g/cm^3)	Simulation result density (g/cm^3)			
		μ of 0.2	μ of 0.1	μ of 0.05	μ of 0.025
Top section	6.4	6.5	6.45	6.37	6.32
Middle section	6.12	5.77	5.97	6.12	6.2
Bottom section	6.32	6.5	6.45	6.37	6.32

It is to be notice that the FE simulation result with friction coefficient of 0.05 has the closest density for each section to the experimental result. However, it is to be further noted that more experimental effort should be given to friction measurements to improve the use of FE simulation of powder compaction experiments.

Chapter 7

Conclusions and Recommendations

7.1 Conclusions

The general objectives of the thesis to study the characteristics of metal powder compaction including fill, transfer and compaction as an integrated process have been achieved. The combination of experimental and simulation studies provides new insights, which enhance our understanding of various stages of green parts generation.

1. A large number of small scale experiments have been completed of pre-compaction, compaction and post-compaction steps such as powder filling from shoe to the die by suction, powder transfer, compaction and ejection process by using a lab-scale integrated die fill and compaction system with a transparent wall section of the die allowing for observation and recording of the powder movement with camera for subsequent analysis.

2. ARAMIS spatial 2D strain data has been obtained by analyzing images of powder through the transparent sapphire window during filling, transfer and compaction, which yield interesting and detailed information about the nature of powder flow and rearrangement during the above processes. The calculated strain results are obtained using a re-meshing procedure, in which DIC was used to measure the local strain increments. The average and local strain development characteristics for metal powder compactions in single and double action compaction modes are generally

consistent with the trend reported in the literature for average and local density measurement as well as from complementary experiments carried out in this research.

3. ARAMIS based axial strain distribution data and its conversion to density distribution has been validated with experimental density distribution measurements.

4. Two other methods for measuring the green density and its distribution have been successfully developed in terms of the relationship between the Vickers hardness value and green density and average surface roughness value and green density of the metal powder compacts. The latter correlation has not been reported in the literature.

5. A density dependent Drucker-Prager Cap plastic model has been utilized to simulate die compaction experiments by using ABAQUS CAE explicit. Experiments with specified metal powder mixture SL5506 were conducted in order to calibrate the constitutive models. It was shown that this constitutive model could be used to obtain a reasonable agreement with experiments. The results also indicate that friction had a dominating influence on the outcome of the simulations.

7.2 Recommendations

1. A technique for measurement of initial fill density, prior to compaction, will be extremely useful for the subsequent understanding of density after compaction.

2. In this work, a new method of the digital image correlation (DIC) analysis has been applied to obtain strain map on one of the faces of the green compact. Since most of the geometries of the compact parts used in the automobile industry are circular, a cylindrical die with a circular transparent window should be designed to study the compaction process.

3. The approach of using surface roughness measurement technique to predict green density can be improved. A non-contacting surface roughness testers can be used to measure the surface roughness which may reduce the error generated by the vibration of the contacting tester's tip running into the pores on the surface of the powder compact.

4. Experimental friction measurements between the die wall and powder during compaction should be carried out to provide useful data for FE simulations. Currently, no clear guide line with respect to friction is available for such simulations.

References

Alves, Luis M.M., Martins, Paulo A.F., and Rodrigues, Jorge M.C., *A new yield funciton for porous materials*, Journal of materials processing technology, 2006, Vol. 179, page 36-43.

ARAMIS 4.7 user menu, GOM, 2001.

ATSM Designation: B 946-06, ATSM International, 2006.

ATSM Standard E92-8, *Standard test method for Vickers hardness of metallic materials*, ATSM International, 1987.

Acculab gravity kit, http://www.lab-balances.com, Precision Weight Balances, 2009.

Berg, Sigurd, *Growth of PM through material and preocesses development for high performance components*, Montreal : s.n., 2005, PM²TEC2005. page 1-10.

Biswas, K., *Comparison of various plasticity models for metal powder compaction process*, Journal of Materials Processing Technology, 2005, Vol.166, page 107–115.

Burch, S.F., Cocks, A.C.F., Prado, J.M. and Tweed, J.H., *Die Fill and Powder Transfer*, Book chapter 9, Modeling of Powder Die Compaction, Springer, 2008.

Chtourou, H. Guillot,M. and Gakwaya, A., *Modeling of the metal powder compaction process using the cap mode Part I. Experimental material characterization and validation*, 2002, International Journal of Solids and Structures, Vol. 39, page 1059–1075.

Chtourou, H. Guillot,M. and Gakwaya, A., *Modeling of the metal powder compaction process using the cap mode Part II. Numerical implementation and practical applications*, 2002, International Journal of Solids and Structures, Vol. 39, page 1077–1096.

Cocks, A. C.F., *Constitutive modelling of powder compaction and sintering*, Progress in Materials Science, 2001, Vol. 46, page 201-229.

Cocks, A.C.F., Motazedian, F. and Sinka, L.C., *The influence of airflow on gravity and suction filling,* Advances in Powder Metallurgy & Particulate Materials—2007, Part 3 Compaction & Forming Processes, International Conference On Powder Metallurgy & Particulate Materials, May 13–16, Denver, Colorado, 2009.

Demetry, C., Souto, F.S., Ryden, B.C., and Roy, J.M., *Tactile sensing of density uniformity in powder beds after die filling*, Powder Technology, 1998, Vol. 45, page 119-124.

Drucker, D.C. and Prager, W., *Soil Mechanics and Plastic Analysis or Limit Design*, Quarterly and Applied Mathematics, 1952, Vol.10, page 157-175.

Fleck, N.A., *On the cold compaction of powders*, Journal of the Mechanics and Physics of Solids, 1995, Vol. 43, page 1409–1431.

Fleck, N.A., Kuhn, L.T., McMeeking, R.M., *Yielding of metal powder bonded by isolated contacts*, Journal of the Mechanics and Physics of Solids, 1992, Vol. 40, page 1139–1162.

Garg, P., Park, S.J. and German, R. M., *Effect of die compaction pressure on densification behavior of molybdenum powders* 2007, Internaltional Journal of Refractory Metals & Hard Materials, page 16-24.

German, R, Powder Metallurgy Science, Second edition, Metal Powder Industries Federation, 1994, page 21-31, 166-170, 212-220 and 370-374.

German, R and Olevsky, E, Mapping the compaction and sintering response of tungsten-based materials into the nanoscale size range, International Journal of Refractory Metals & Hard Materials, 2005, Vol. 23, page 294-300.

German, R, A-Z of powder metallurgy, 2006, Elsevier Science, page 231-233.

Gethin, D.T., Ransing, R.S, Lewis, R.W., Dutko, M. and Crook, A.J.L, *Numerical comparison of a deformable discrete element model and an equivalent continuum analysis for the compaction of ductile porous material*, Computers and Structures, 2001, Vol. 79, page 1287-1294.

GOM, www.gom.com, 2009.

Gripshover, P.J., *A comparison of conventional and hydrostatic pressing of metal powders*, Material Technology, 1970, Vol. 1, page 520-522.

Green, R.J. *A plasticity theory for porous solids*, International Journal of Mechanical Science, 1972, Vol.14, page 215-224.

Han, L.H. Elliott, J.A. Bentham, A.C. Mills, A. Amidon, G.E.and Hancock, B.C., *A modified Drucker-Prager Cap model for die compaction simulation of pharmaceutical powders*, 2008, International Journal of Solids and Structure, Vol. 45, page 3088-3106.

Hoganas, www.hoganas.com, 2009.

Hua, L. Qin, X. Mao, H. and Zhao, Y., *Plastic Deformation and Yield Criterion for Compressible Sintered Powder Material*, Journal of Material Processing Technology, 2006, page 174-178.

Jackson, S., Sinka, I.C., Cocks, A.C.F., *The effect of suction during die fill on a rotary tablet press*, European Journal of Pharmaceutics and Biopharmaceuties, 2007, vol. 65, page 253-256.

Kim, Mansig, *Improved Density Distribution in Powder Metallurgy Parts with Filtering Methods*, Advanced Materials Research, 2007, Vol. 26-28, page 445-448.

Kim, H.S. and Lee, D.N., *Plastic yield behaviour of porous metals*, Powder Metallurgy, 1992, Vol. 35, page 275-279.

Kuczynski, G.C. and Zaplatynskyi, I., *Density distribution in metal powder compacts*, Journal of metals, 1956, page 215.

Kuhn, H.A. and Downey, C.L., Deformation characteristics and plasticity theory of sintered powder materials, International Journal of Powder Metallurgy, 1971, Vol. 7, page 15-25.

Kwon, Y.S., Lee, H.T. and Kim, K.T., *Analysis for Cold Die Compaction of Stainless-Steel Powder*, Journal of Engineering and Technology, 1997, page 366-373.

Liu, Y., German, R.M. and Engle, R.S., *Finite element modelling for loose powder compaction*, 2000 International Conference on Powder Metallurgy, 2000, New York.

Mearson, G.A., Rasskazov, N.I. and Chulkov, V.P., *Experimental investigation of the compaction process of powder materials*, Poroshkovaya Metallurgiya, 1970, Vol. 85, page 21.

Metal Powder Industries Federation, www.mpif.org, 2009.

MPR, *Magnetic compaction process nears market*, 2000.

Schofield, A., *Critical State Soil Mechnics*, 1968, McGraw-Hill, London.

Sielamowicz, I., Blonski, S. and Kowalewski, T.A., *Digital particle image velocimetry (DPIV) technique in measurements of granular material flows*, Part 2 of 3-converging hopers, Chemical Engineering Science, 2006, Vol. 61, page 5307-5317.

Shima, S. and Oyane, M., *Plasticity theory for porous material*, International Journal of Mechanical Science, 1976, Vol. 18, page 285-291.

Sinka, I.C., Cunningham, J.C., Zavaliangos, A., T*he effect of wall friction in the compaction of pharmaceutical tables with curved faces: a validation study of the Drucker-Prager Cap model*, Powder Metallurgy, 2003, vol.133, page 33-43.

Smith, L.N. and Midha, H.S., *Computer simulation of morphology and packing behaviour of irregular particles*, for predicting apparent powder densities, Computational Materials Science, 1997, Vol. 7, page 377-383.

Steinberg, M., Kamm, R., and Wulff, J., *Plastic deformation in metal powder compacts*, Powder Metallurgy, 1947, Vol. 17, page 439-456.

MPIF, *student information*, http//:www.mpif.org, 2009, Metal Powder Industries Federation.

Mitutoyo production specification, http://www.mitutoyo.ca, 2009, Mitutoyo Cooperation.

Tanwongwan, W., Manonukul, A. and Carmai, J., *Effects of powder size and initial arrangement on cold compaction*, JSME International Journal, 2005, Vol. 48, page 376-380.

Wu, C.Y. and Cocks, A.C.F., *Flow behaviour of powders during die filling*, Powder Metallurgy, 2004, Vol.47, page 127-136.

Wu, C.Y., Cocks, A.F.C., Gillia, O.T. and Thompson, D.A., *Experimental and numerical investigations of powder transfer*, Powder Technology, 2003, Vol.138, page 216-228.

Wu, C.Y., Dihoru, L. and Cocks, A.C.F., *The flow of powder into simple and stepped dies*, Powder Technology, 2003, vol.134, page 24-29.

Wu,C.Y., Ruddy, O.M., Bentham, A.C., Hancock, B.C., Best, S.M. and Elliott, J.A., Modelling the mechanical behaviour of pharmaceutical powders during compaction, Powder Technology, 2005, Vol. 152, page 107-117.

Wu, C.Y., *DEM simulations of the die filling during pharmaceutical tabulating*, Particuology 6, 2008, page 412-418.

Zhang, L., *Shear deformation of granular media in pure shear, direct shear and simple shear*, PhD Thesis, 2003, Aston University.

Appendix I Powder Compaction Data

Test #	Compaction type	Filling	Material	Max Load (lbs)	Compaction pressure (MPa)	Density (g/cm^3)
1	Single	Gravity	ATOMET 1001 with 7% Kenolube	9445	329	6.58
2	Single	Gravity	ATOMET 1001 with 7% Kenolube	15896	554	6.99
3	Single	Gravity	ATOMET 1001 with 7% Kenolube	16175	564	7.04
6	Double	Gravity	ATOMET1001 with 7% Kenolube	14885	515	7.01
7	Double	Gravity	ATOMET 1001 with 7% Kenolube	17037	590	7.18
8	Double	Gravity	ATOMET 1001 with 7% Kenolube	18517	641	7.25
9	Double	Gravity	ATOMET 1001 with 7% Kenolube	20599	713	7.30
10	Double	Gravity	ATOMET 1001 with 7% Kenolube	11835	410	6.84
11	Single	Suction	SL5506	5700	197	5.99
12	Double	Suction	SL5506	5245	172	6.04
13	Double	Gravity	SL5506	15521	541	7.03
14	Double	Gravity	ATOMET 1001 with 7% Kenolube	14885	515	7.01
15	Double	Gravity	ATOMET 1001	14094	488	6.84
16	Double	Gravity	ATOMET 1001	9567	331	6.36
17	Double	Gravity	ATOMET 1001	11428	396	6.54
18	Double	Gravity	ATOMET 1001	14094	488	6.84
19	Double	Gravity	ATOMET 1001	15659	542	6.94
20	Double	Suction	SL5506	11040	371	6.7
21	Double	Suction	SL5506	7750	261	6.32
22	Double	Suction	SL5506	11077	368	6.68
23	Double	Suction	SL5506	11373	383	6.27
24	Double	Suction	SL5506	11469	385	6.75
25	Double	Suction	SL5506	7485	251	6.27
26	Double	Suction	SL5506	16900	589	6.74

Appendix II Powder Compact Properties

Test#	Upper Load	Lower load	Average load	Density	Pressure
	lbs	lbs	lbs	g/cm^3	MPa
1	6380	5390	5885	6.15	222
2	6510	6490	6500	6.26	246
3	7870	8510	8190	6.44	309
4	10200	10530	10365	6.63	392
5	10990	10890	10940	6.64	413
6	12320	12780	12550	6.80	474
7	10840	10850	10845	6.80	410
8	10610	11360	10985	6.79	415
9	8270	8210	8240	6.54	311
10	8940	9130	9035	6.62	341
11	9930	10730	10330	6.73	390
12	11590	10930	11260	6.83	425
13	13790	14260	14025	6.95	530
14	5280	5590	5435	6.15	205
15	5480	5620	5550	6.07	210
16	5350	5700	5525	6.11	209
17	5620	5940	5780	6.15	218
18	5090	5400	5245	5.99	198
19	5600	5420	5510	6.05	208
20	7640	7310	7475	6.33	282
21	5840	5560	5700	6.04	215
22	6190	6420	6305	6.19	238
23	6550	6010	6280	6.18	237
24	7950	7850	7900	6.41	298
25	8720	8250	8485	6.51	321
26	8320	8850	8585	6.48	324
27	7990	5930	6960	6.31	263
28	7460	7730	7595	6.40	287
29	6530	6450	6490	6.20	245
30	7560	7570	7565	6.32	286
31	16960	16840	16900	7.01	639
32	16700	16420	16560	7.02	626
33	19450	19190	19370	7.11	732

Appendix III Vickers Hardness Measurements on Powder Compacts

TEST#	load lbs	HV1	HV2	HV3	HV4	HV5	HV6	HV Average	Density g/cm^3
1	5890	31	34	30	39	38	40	35.3	6.15
2	6500	31	39	39	40	34	40	37.2	6.26
3	8190	52	48	51	48	48	44	48.5	6.44
4	10370	57	63	65	55	65	56	60.2	6.63
5	10940	58	63	65	63	58	59	61.0	6.64
6	12550	69	70	63	74	80	72	71.3	6.80
7	10850	63	72	63	59	61	60	63.0	6.80
8	10990	68	67	63	71	67	66	67.0	6.79
9	8240	47	55	49	44	49	46	48.3	6.54
10	9040	56	57	56	45	50	52	52.7	6.62
11	10330	62	60	60	62	67	67	63.0	6.73
12	11260	70	76	70	56	68	60	66.7	6.83
13	14030	83	79	71	77	68	74	75.3	6.95
14	7480	51	44	44	41	36	25	40.2	6.33
15	5700	29	30	31	28	28	24	28.3	6.04
16	6310	35	37	35	32	34	31	34.0	6.19
17	7900	46	42	41	39	39	36	40.5	6.41
18	8490	49	48	48	45	45	43	46.3	6.51
19	8590	47	45	40	47	46	43	44.7	6.48
20	6490	34	42	42	37	39	38	38.7	6.20
21	16900	84	87	79	78	80	79	81.2	7.01
22	16560	78	82	80	78	84	85	81.2	7.02

Appendix IV Surface Roughness Measurements on Powder Compacts

Test#	Max load (lbs)	Location	Ra (μm)	Rz (μm)
1	5890	top	2	22.9
		middle	1.9	31.8
		bottom	1.8	31.2
	average		1.90	28.63
2	6500	top	1.4	12.6
		middle	1.5	22.2
		bottom	1.5	40.7
	average		1.47	25.17
3	8190	top	1.1	17.2
		middle	1.3	18.4
		bottom	1.2	14.4
	average		1.20	16.67
4	10370	top	0.6	23.2
		middle	0.8	10.7
		bottom	1.1	12.8
	average		0.83	15.57
5	10940	top	0.5	6.3
		middle	0.7	6.9
		bottom	1	7.1
	average		0.73	6.77
6	12550	top	0.6	6.4
		middle	0.7	8.4
		bottom	0.7	9.9
	average		0.67	8.23
7	10850	top	0.7	6.6
		middle	0.7	8.8
		bottom	0.9	11.6
	average		0.77	9.00
8	10990	top	0.6	6.8
		middle	0.7	8.3
		bottom	0.9	9.1
	average		0.73	8.07
9	8240	top	1.1	11.4
		middle	1	17.1

		bottom	1	14.6
	average		1.03	14.37
10	9040	top	0.7	10.9
		middle	1	19.2
		bottom	0.9	12.8
	average		0.87	14.30
11	10330	top	0.6	7.1
		middle	0.9	13.4
		bottom	0.7	13.8
	average		0.73	11.43
12	11260	top	0.6	5.9
		middle	0.7	18.4
		bottom	0.8	8.3
	average		0.7	10.87
13	14025	top	0.4	5.2
		middle	0.8	9.5
		bottom	0.6	5.6
	average		0.60	6.77
14	5780	top	1.7	20.1
		middle	2.1	31.2
		bottom	1.9	25.8
	average		1.90	25.70
15	7480	top	1.4	27.2
		middle	1.5	28.9
		bottom	1.9	29.7
	average		1.60	28.60
16	6310	top	1.4	18.5
		middle	2.1	53.1
		bottom	1.8	32.4
	average		1.77	34.67
17	6280	top	1.3	20.8
		middle	2.1	43.5
		bottom	1.5	24.9
	average		1.63	29.73
18	7900	top	1.4	21.9
		middle	1.7	25.6
		bottom	1.7	42.1
	average		1.60	29.87
19	8490	top	1.2	30
		middle	1.3	22
		bottom	1.3	21.5

	average		1.27	24.50
20	8590	top	1.2	29.1
		middle	1.5	30.6
		bottom	1.2	21.6
	average		1.30	27.10